UNIVERSITY OF OKLAHOMA

GRADUATE COLLEGE

DEVELOPMENT OF A PROTOTYPE IN-SITU FATIGUE SENSOR FOR STRUCTURAL HEALTH MONITORING OF HIGHWAY BRIDGES

A DISSERTATION

SUBMITTED TO THE GRADUATE FACULTY

in partial fulfillment of the requirements for the

Degree of

DOCTOR OF PHILOSOPHY

By

B. H. M. PRIYANTHA WIJESINGHE
Norman, Oklahoma
2010

DEVELOPMENT OF A PROTOTYPE IN-SITU FATIGUE SENSOR FOR STRUCTURAL HEALTH MONITORING OF HIGHWAY BRIDGES

A DISSERTATION APPROVED FOR THE
SCHOOL OF CIVIL ENGINEERING AND ENVIRONMENTAL SCIENCE

BY

_____
Dr. Kyran D. Mish, Co-chair

_____
Dr. J. David Baldwin, Co-chair

_____
Dr. Chris Ramseyer

_____
Dr. K. K. Muraleetharan

_____
Dr. Thomas Kang

_____
Dr. Joseph P. Havlicek

Dedication

This dissertation is dedicated to my family – my wonderful parents,
my loving husband and my darling son.
Without their support and love this work would not have been possible.

ACKNOWLEDGEMENTS

It is with great pleasure I acknowledge the following people who made this work possible.

First of all, I wish to express my deep gratitude to Dr. K.D. Mish for being my major advisor and for all the valuable comments, guidance, and inspiring discussions encouraging my work, and above all, for his faith in my effort and in my success as a PhD candidate. Dr. Mish, I could not have wished for a better advisor.

I am forever grateful to my co-advisor, Dr. J.D. Baldwin, for the immense guidance extended to me with his field of expertise: his incisive comments and valuable criticisms greatly helped to shape this work and make it more fruitful. Dr. Baldwin, without your guidance and endless support this work would never have been possible.

I would like to express my sincere thanks to Dr. Chris Ramseyer, not only for serving as a member of my PhD committee, but also for his valuable ideas, guidance and financial support provided me during my early years of PhD candidature.

I am forever indebted to Dr. K.K. Muraleetharan for introducing me to CEES at OU in 2004, for his valuable comments, and for his time serving as a member of my PhD committee.

I owe my gratitude to both Dr. Thomas Kang and Dr. Joseph P. Havlicek for their valuable comments and time serving as members of my PhD committee. They both have helped me in many ways throughout my PhD candidature, which I will always be thankful for.

Special thanks to Dr. Thordur Runolfsson for his comments on the research work and his guidance in circuit design.

I am grateful for the continuous financial support provided for this research by the Oklahoma Transportation Center under grant OTCREOS7.1-36.

Many thanks to Scott Zacharie for working with me on this project and his contribution to laboratory testing during his masters candidature. I am also thankful to Adam Kelly and Ryan Abraham for their helping hands in the research work and Kanwardeep Bhachu for sharing a peaceful working environment with me.

I would also like to thank Mr. Billy Mays and Mr. Greg Williams of AME Machine Shop for their continuous help by providing me with the necessary technical support. Special thanks go to Tim Long and Amanda Hyde for taking extra time and effort to fabricate the sensors with the highest quality possible.

I would also acknowledge the staff of OU Libraries, especially the people in the Engineering Library for their excellent facilities and service provided me with all the required literature in a timely manner to successfully complete my doctoral research. I would also like to thank Mr. Jonathan Killgore of OU IT for all the IT support and Ms. Paula Gerhard of DYSSC center for facilitating a peaceful work environment for me. Many thanks go to OU Writing Center for their help in proof reading.

I wish to convey my appreciation to the CEES faculty and staff, especially to Dr. Robert Knox, Dr. Gerald Miller, Ms. Susan Williams, Ms. Brenda Clouse and Ms. Audre Carter for their continuous help in many aspects throughout my PhD candidature.

I would like to extend my sincere thanks to Mr. Michael Schmitz of Fears Structural Engineering Laboratory for teaching and training me on the necessary laboratory skills to do my research during my early years of graduate research.

I wish to thank Dr. Jinsong Pei for the financial support provided me during my early years of PhD candidature, and I also wish to thank Dr. Musharraf Zaman for providing me financial support as a TA in spring 2007.

I'm also grateful for the people in the engineering division of the Star Building Systems, OKC, for their great support and friendship during my internship period. Special thanks to Mr. Dustin Cole for his guidance and advice.

It is with great pleasure I remember the financial support provided me as a TA by the College of Architecture at OU during my early years of PhD candidature. Special thanks go to Professor William Bauman and Dr. I-Kwang Chang. They both provided me with valuable advice and considered me as part of their extended families during my early years of graduate studies at OU.

My sincere thanks go to my colleague Krisda Piyawat for his valuable support during my early years of research work and my thanks to Jason, Brent, Jessica, Colby, Eric, Christopher, Hungjr, Phuong, Yohanes, Keith, Anh, Kyle, Mallory, Werner, Archith, Shideh and Kim for their friendship and support during my graduate research at OU.

I'm fortunate to have wonderful friends like Kosala, Babak, Nimali, Hemantha, Varuni, Anuruddha, Anjalee, and the Wijethunga family, who were there always when I needed help. Dear friends, you are the greatest that anyone could have ever wished for.

I'm also grateful to Venerable Piyarathana Thero for all the spiritual blessings he made towards my success.

I wish to extend my heartiest love and thanks to my late mother: even though she is not with me today, she had always been the greatest courage in my life. My sincere thanks go to my loving father, my sisters and their families, my aunts and all my relatives who helped me in many ways and shared my happiness and sorrow throughout my life.

Last but not least, I wish to thank to my loving husband Daminda, who was there with me, always, as my shadow, and my loving son Jihan who deserves special thanks for keeping me happy always. You both gave me all the emotional support to successfully finish my work.

I offer my regards and blessings to all of those who supported me in any way during the completion of my dissertation. Without their constant support and encouragement, this endeavor would never have been fruitful.

TABLE OF CONTENTS

LIST OF TABLES

LIST OF ILLUSTRATIONS

ABSTRACT

Fatigue damage to bridges has been identified as a threat to bridge safety. Fatigue cracks usually occur at stresses lower than the anticipated design stress levels. Unlike yielding or corrosion, fatigue cracks are seldom visible enough to be detected by visual inspection and therefore can be easily overlooked. Since a larger portion of the life of a structure is spent on crack initiation (as opposed to crack propagation), it is vital to develop methods to detect fatigue crack initiation.

Unfortunately, most of the methods that are developed to detect fatigue cracks do not accommodate crack initiation and are not sensitive enough to detect fatigue nucleation. A prototype in-situ fatigue senor has been developed to detect nucleation of fatigue damage in steel highway bridges.

The in-situ fatigue sensor is designed to be bonded to the base structure and is based on the strain-life fatigue analysis method. Sensors are constructed of electrically conductive material with notched sensor arms producing varying stress concentration factors. The sensor operates on the principle of predictable progressive failure of the parallel arms as fatigue damage is accumulated in the base structure. Experimental results of the behavior of the fatigue sensor under constant amplitude loading and variable amplitude loading of a base structure-mimicking carrier specimen are compared with the simulation results obtained by the finite element analysis method and show reasonable agreement.

CHAPTER 1. INTRODUCTION

1.1. Background and Need of the Study

According to the Federal Highway Administration (FHWA), steel bridges represent 40% of the bridges and 60% of the structurally deficient bridges in the nation's bridge inventory. Structurally deficient means that these bridges are given a poor or worse rating for the deck, superstructure or substructure and have a significantly low load-carrying capacity which falls below the minimum standards (Chase 1998). Aging is one of the key causes of structural deficiency. Eighty percent (80%) of the bridges built between 1905 and 1910 are categorized as structurally deficient. According to the FHWA, 1% (5,000) bridges become deficient each year (Chase 1998).

Fatigue damage and corrosion are considered among the major defects that emerge due to aging of structures (Zhang 2006a). In addition to aging, heavy truck loads which frequently pass over these bridges (Fisher 1998) and major catastrophic events such as earthquakes are considered as likely sources that initiate and develop fatigue cracks.

Fatigue damage to bridges has been identified as a threat to bridge safety due to several reasons. Fatigue cracks in steel structures are well-known to occur at stresses lower than typical design stresses. Unlike corrosion, yielding, spalling or material loss, short fatigue cracks are hardly visible and can be difficult to detect by visual inspection. For this reason they can be easily overlooked. Since state-of-the-art bridge health monitoring is largely depend on visual inspection (ODOT 2006), a question remains on

the safety and reliability of these aging bridges. Detecting fatigue cracks, therefore, is crucial in Structural Health Monitoring (SHM) of steel bridges.

Currently, various non destructive evaluation (NDE) methods are being researched, developed, and evaluated for detecting fatigue damage, including ultrasonic testing (Gongkang 2004), infrared and thermal imaging (Moore 1998), acoustic emission (Son 2004), eddy current methods (Rakow 2007), dye penetrant inspection (Gongkang 2004; Son 2004), magnetic particle testing (Fisher 1998; Gongkang 2004), and radiographic testing. In general, these techniques can be considered as non strain-based methods. Strain-based methods include fiber optic sensors (Lee 2001), piezoelectric sensors (Zhang 2006a) and various crack propagation gages (Vishay 2008).

Most of these techniques, however, have certain limitations such as accessibility, automation, power supply, long term durability, environmental noise and bulkiness (Zhang 2006a). In practice, the majority of these techniques cannot be cost-effectively deployed in required bridge sites to obtain reliable information that can be easily interpreted by a bridge inspector. Moreover, the majority of these methods are developed based on the fracture mechanics approach and thus do not address the crack nucleation stage of fatigue damage evolution. Since a larger portion of fatigue life in metals is spent on crack nucleation than on propagation, it is vital to develop methods to detect the nucleation of fatigue cracks in steel bridges. As a result, a prime need for a simple, yet reliable, easy to deploy fatigue crack detecting method is in demand. This research addresses numerical and experimental aspects of development work of a prototype in-situ fatigue sensor which is capable of detecting fatigue crack nucleation in steel structures while being simple in concept, low in cost, easy to apply, and easy to interpret.

1.2. Hypotheses

The Strain Based Fatigue Analysis Method

Out of the three main fatigue analysis methods widely used (Stress-based, Strain-based, and Fracture Mechanics-based), the **Strain-based Fatigue Analysis Method** was adopted in this study. The stress-life or stress-based analysis method is commonly used in high cycle fatigue (HCF) analysis in which little plastic deformation (stresses are mostly elastic) is considered (Lee 2005) and is based on the fatigue limit of the material. Fracture mechanics-based method or crack growth analysis method uses linear elastic fracture mechanics with the related crack growth material properties to determine how fast a crack will grow, and the remaining life of the structure. The concept of stress intensity is involved in this method.

Despite the fact that most engineering structures are designed for elastic nominal stresses, local stress concentrations cause plastic strains to develop in the regions around them. **The strain based method** assumes that the smooth specimen tested under strain control can simulate fatigue damage at the notch root of an engineering component. Equivalent fatigue damage is assumed to occur in the material at the notch root and in the smooth specimen when both are subjected to identical stress-strain histories (Bannantine 1990).

The advantage of using the strain-life method is its ability to incorporate the elastic and plastic responses of the structural material. It also provides a way to account for the cyclic plasticity in the root of a notch.

The following information is required for a strain-life fatigue analysis

- Material properties obtained from strain controlled laboratory fatigue data

- Stress-strain history of the critical location *(e.g. notch)*
- Techniques to identify damage events - *cycle counting – **Rain-flow** method was focused in this study*
- Methods to include mean stress effects - ***Morrow** and **Smith-Watson-Topper (SWT)** mean stress correction methods were utilized in this study*
- Damage summation techniques - ***Miner's rule** was used in this study*

The Prototype Fatigue Detecting Sensor

The prototype sensor, which is made of an electrically conductive material, consists of several sensing arms; each arm is designed with different notch geometries to create different stress concentration factors (SCF). A prototype fatigue sensing element is shown in Figure 1.1. When the sensor is properly attached to a structure, it will experience the same nominal strain, but different maximum strains at the notch roots due to differing notch geometries. As a result, the arms will fail progressively at different number of loading cycles, thus indicating the accumulation of fatigue damage in the attached structure. Strain-based fatigue analysis method can be used to calibrate the progressive failure of the sensing arms with the accumulation of stress in the attached structure. Failure of each sensing arm can be detected by measuring its associated electrical resistance.

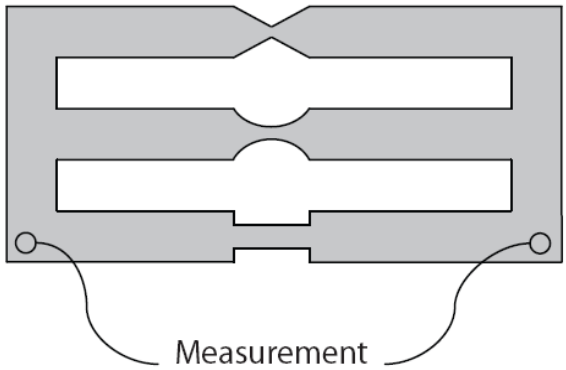

Figure 1.1 The concept of prototype fatigue-detecting sensor

1.3. Research Objectives

The main objective of this research was to develop a unique low-cost reliable fatigue detecting sensor which is capable of monitoring the accumulation of fatigue damage in highway bridges.

The following specific problem areas have been addressed through this research.

Numerical

- Apply finite element analysis (FEA) method for the design and analysis of the fatigue sensor.

  - Investigate the fatigue analysis capabilities of commercially available finite element analysis software, validate their capabilities and deploy an appropriate FE and fatigue analysis tool for the research.

  - Create comprehensive FE models with sensor material, substrate and attached structural elements which can be used to (1) optimize the performance of laboratory testing, (2) develop the sensor design - geometry and (3) select appropriate materials.

Overall, the finite element analysis was used to mitigate the experimental limitations, especially the time spent on accumulating large numbers of cycles.

Experimental

- Conduct laboratory experiments to develop and evaluate the design and performance of prototype in-situ fatigue sensors and compare the results with the simulated results
- Design and develop a circuit and deploy a commercially available data acquisition system (DAQ) which is sensitive enough to capture the change in resistance of the sensing arms due breaking of notches
- Study, identify and deploy appropriate encapsulating and fabricating methods for the sensor *(future focus)*
- Research and develop a reliable self power strategy for the senor *(future focus)*

1.4. Method and Scope of Work

There are two major segments in this research: numerical and experimental. Numerical modeling and simulation were carried out simultaneously with the experimental work to achieve optimum results from the experiments and vice versa.

Cyclic fatigue experiments were carried out in the laboratory (1) to prove the concept, (2) to develop a power supply and signal conditioning strategy, (3) to calibrate and improve the design and the sensitivity of the prototype sensor, (4) to investigate and deploy proper attachment options (5) and to monitor the performance for constant amplitude and variable amplitude loading at different applied stress levels. Figure 1.2 shows the flow of the overall research tasks.

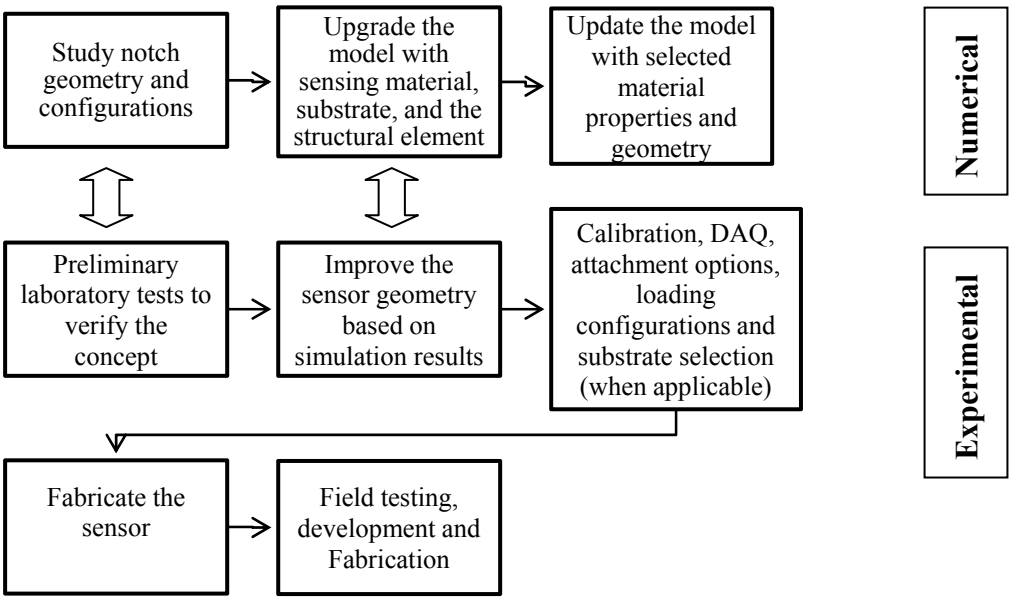

Figure 1.2 Research layout

1.5. Dissertation Layout

This dissertation consists of 7 chapters. Chapter 2 is the literature review in which the mechanism of fatigue damage, fatigue analysis theories, fatigue damage detection methods and fatigue in steel bridges are discussed. The 3rd chapter is the introductory chapter to the FEA method; an overview of the FE based fatigue analysis and an investigation to the validity of the ANSYS WB fatigue capabilities are discussed. A general introduction to the experimental procedure utilized in this research with details of the proof-of-concept experiment and its results are discussed in the 4th chapter. Chapter 5 serves as the core of the dissertation, in which the experimental and simulation work and results pertaining to the deep "U" notch prototype Al sensors are presented. Different other approaches taken while developing the aforesaid deep "U notch Al prototype are considered important thus briefly discussed in Chapter 6. Finally, Chapter 7 concludes the dissertation with a summary and concluding remarks with suggestions for future directions in this research.

CHAPTER 2. LITERATURE REVIEW

The literature review is organized under several sections. The first section discusses the mechanism of fatigue damage as it is understood by researchers today. The second section briefs the most established fatigue analysis methods that are being used today and discusses Strain-Based Method in detail as a theoretical approach to this research. The next three sections are devoted to the practical aspect of fatigue: fatigue damage in bridges, fatigue damage monitoring techniques, and the state-of-practice fatigue damage retrofitting methods, respectively.

2.1. Fatigue and Fatigue Damage Theories

2.1.1. Fatigue Mechanism

Fatigue is a localized damage process of a component produced by cyclic loading and is a cumulative process which includes crack nucleation, short crack growth, long crack growth and final fracture. The nature of a fatigue crack is that localized plastic deformations usually occur at the crack tip (the highest stress site), while elastic deformations occur at other regions. Component will fail as a result of increasing length of the crack (due to increasing number of load cycles) (Lee 2005).

Fatigue cracks can initiate on localized shear planes at or near high stress concentrations, inclusions, porosity or discontinuities. There are several equivalent models available to explain the initiation of fatigue cracks ((Broek 1986) and reference therein). Wood's model (1958) (see Figure 2.1) shows that during loading, slip occurs on a favorably oriented plane, and during unloading slip takes the reverse direction on a

parallel slip plane. The slip on the first plane is restrained by strain hardening and oxidation due to the newly created free surface resulting in an extrusion or an intrusion in the metal surface. An intrusion created in this way can grow into a crack by continuous loading cycles.

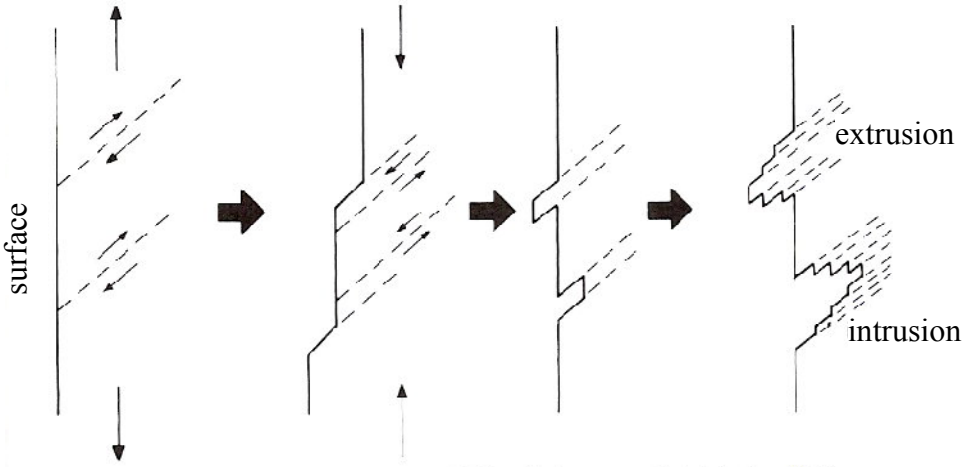

Figure 2.1 Wood's model for fatigue crack initiation (Wood 1958)

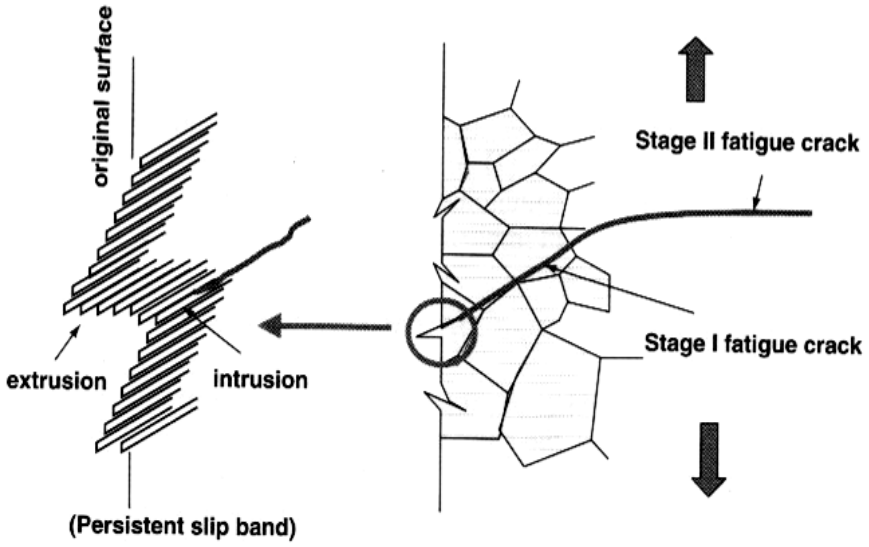

Figure 2.2 The fatigue process: a thin plate under cyclic tensile loading (Lee 2005)

Once this first step (crack nucleation) starts, and the cyclic loading continues, the crack tends to grow along the plane of maximum shear stress and through the grain boundary. The crack growth is divided into two stages: Stage I cracks and Stage II cracks. Stage I is the initial, short finite length crack growth and its crack tip plasticity is mostly affected by the grain size, type of slippage, orientation and the stress level (properties of the material micro-structure). Stage II crack growth refers to long crack propagation normal to the principal tensile stress plane (See Figure 2.2). The crack tip plastic zone in Stage II crack is much larger than the material microstructure thus they are less affected by the properties of the material microstructure (Lee 2005). In general, for engineering components, *crack initiation period* refers to the total nucleation and propagation of the short cracks, whereas *crack propagation period* refers to the growth of the long cracks. Even though it is not possible to differentiate the transition period from crack initiation to crack propagation, the crack size at the end of the initiation stage is generally considered between the range of 0.00394 – 0.0394 in. (0.1 – 1 mm) in metals (Lee 2005). Crack initiation size can be estimated by linear elastic fracture mechanics approach. Typically, for a component made of steel, the crack initiation accounts for most of its fatigue life, especially at HCF regime, i.e. $>10^5$ cycles. As oppose to HCF, fatigue life is mostly spent on crack propagation in low cycle fatigue regime (LCF), i.e. $< 10^5$ cycles.

A pattern of ripples develops on the fracture surface as a result of cyclic opening and closing of the crack, termed as *striations*. These striations, which can be seen with an electron microscope, represent one loading cycle for each ripple. These occur due to crack tip blunting and re-sharpening as a result of cyclic loading. As shown in Figure 2.3,

at the beginning, the crack opens when the material above the crack slips along the plane of maximum shear stress while extending its length (see stages 1-2 of Figure 2.3). As a result, the next slip occurs on another plane (stage 3 of Figure 2.3) and afterwards, work hardening and increasing stress activate other slip planes making a blunt crack (stage 4 of Figure 2.3). When plastic deformation occurs in a small region surrounded by elastic regions, during unloading the elastic region contracts towards the plastically deformed region. This results in compressive stresses, which closes and re-sharpens the crack tip (stages 5-7 of Figure 2.3) (Broek 1986). Al alloys are proven to be excellent in creating striations on fatigue fracture surfaces compared to other metals. Figure 2.4 shows an example of striations on Al alloy.

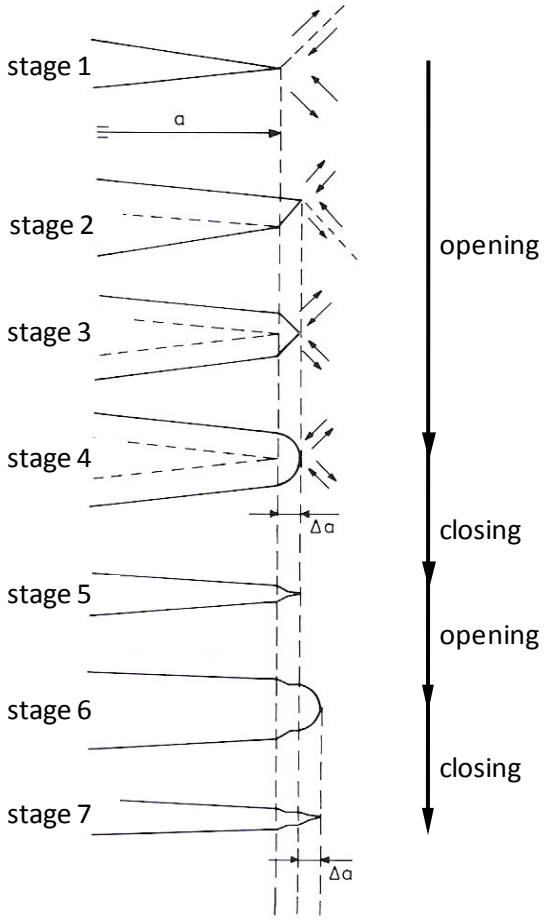

Figure 2.3 Possible model for fatigue crack growth, redrawn from Broek (1986)

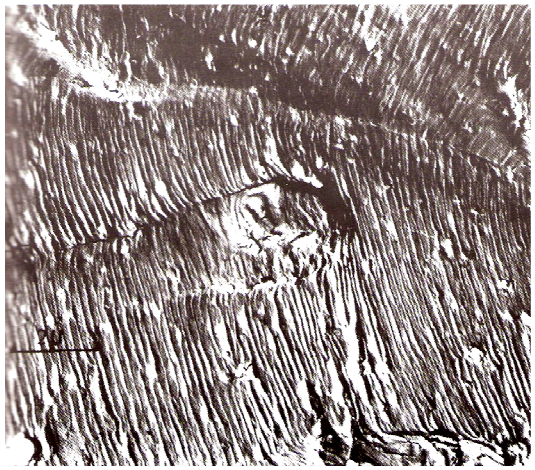

Figure 2.4 Striations on fatigue crack surface of Al-Cu-Mg alloy (Broek 1986)

2.1.2. Fatigue Damage Summation

Fatigue loading of a component or a structure mainly consists of two types: constant amplitude loading and variable amplitude loading. For constant amplitude loading, damage calculation is straightforward since the stress range under consideration is a constant. In real world applications, however, the applied stress range is not always a constant. Instead it consists of varied stress ranges, i.e. transmission, and bridge loading etc. For such applications, a damage summation method needs to be applied to calculate the accumulation of fatigue damage. Different cumulative fatigue damage theories have been developed over the past eighty years focusing on different aspects of fatigue. Altogether, these theories can be categorized as (a) linear damage models, (b) non-linear damage models and double linear damage models, and (c) other methods which include approaches based on crack growth concepts, continuum damage models and energy based theories.

2.1.2.1. Linear Damage Model: Palmgren-Miner Rule

From both linear and nonlinear damage theories available, linear damage theory is more widely used and accepted than nonlinear methods, especially in civil engineering practice. This is because it is simple, easy to apply and produces satisfactory results (Fisher 1998). The Linear Damage Rule (LDR), commonly called the Palmgren-Miner Rule, was first proposed by Palmgren in 1924 and was later developed by Miner in 1945 (Bannantine 1990). It states that the damage fraction (the fraction of life used up by an event or a serious of events) which results from any stress range is a linear function of the number of cycles corresponding to that stress range. The total damage from all stress ranges is the sum of all such events (Bannantine 1990). This can be stated as,

$$\sum \frac{n_i}{N_i} \geq 1 \qquad (2.1)$$

where n_i is the number of cycles that occur at stress range i, and N_i is the number of cycles at the failure at stress range i. Despite its simplicity, it has major shortcomings (Fatemi 1998): it does not account for the load sequence, independent of load level, and lacks load-interaction accountability (Fatemi 1998). However, at higher residual stresses and when plasticity is constrained, such factors are considered to have minimal effect, i.e. structural engineering applications (Fisher 1998). In fact, American Association of State Highway and Transportation Officials (AASHTO 2007) specifications recommend the Palmgren-Miner Rule for estimating cumulative damage. Therefore, for this research, the Palmgren-Miner rule has been used to calculate accumulation of damage due to variable amplitude loading.

2.1.2.2. Non-linear Damage Models

Marko-Starkey Theory

In order to overcome the above mentioned issues related to the LDR Richart and Newmark introduced the concept of damage curve in 1948 and Marco and Starkey, backed by load sequence experiments, proposed the first non-linear load dependant damage theory in 1954 ((Fatemi 1998) and reference therein). This damage theory is a power law relationship in which,

$$D = \sum r_i{}^{x_i} \tag{2.2}$$

where D is the damage, r_i is the cycle ratio corresponding to the ith load level ($r_i = {}^{n_i}/_{N_i}$) and x_i is a variable quantity related to the ith loading level. For the special case of $x_i = 1$, a diagonal line in Figure 2.5 represents the Miner's rule.

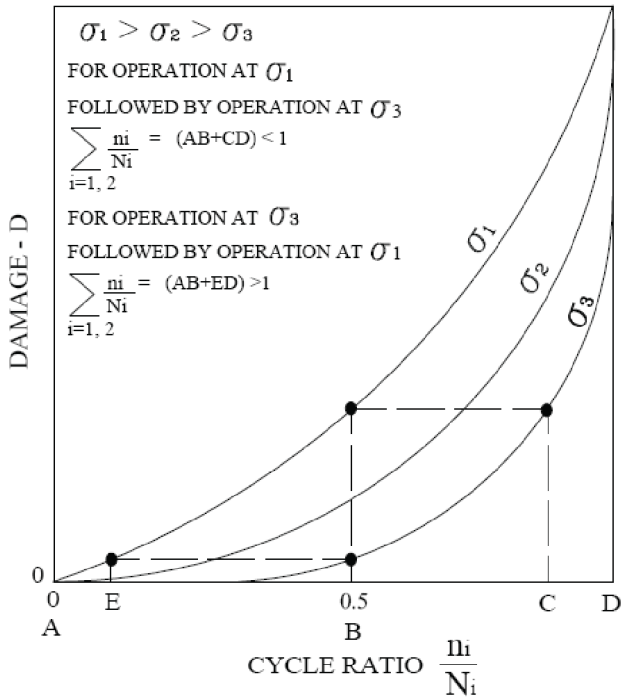

Figure 2.5 Schematic representation of damage versus cycle ratio for the Marco-Starkey Theory, redrawn from Fatemi (1998)

As shown in Figure 2.5, $\sum r_i > 1$ for low to high (L-H) load sequence and $\sum r_i < 1$ for high to low (H-L) load sequence. Experimental evidence under fully reversed loading often shows similar behavior (Fatemi 1998).

Damage Curve Approach by Manson and Halford

Later in 1981, Manson and Halford proposed a damage curve based on the crack growth approach which states that,

$$a = a_o + (a_f - a_o)\left(\frac{n}{N_f}\right)^{\propto f} \tag{2.3}$$

where n is the number of loading cycles applied to form a length of a and a_o is the initial crack length. N_f is the number of cycles applied to obtain the crack length a_f at final fracture. The exponent,

$$\propto f = \frac{2}{3} N_f{}^{0.4} \tag{2.4}$$

and is empirically determined. Cumulative damage, therefore, is defined as,

$$D = {}^{a}/_{a_f} = {}^{1}/_{a_f}\left[a_o + (a_f - a_o)\left(\frac{n}{N_f}\right)^{\propto f}\right] \tag{2.5}$$

and fatigue failure occurs when damage, D, is equal to unity (Lee 2005).

Double Linear Damage Rule by Manson and Halford

Manson and Halford proposed the Double Linear Damage Rule (DLDR), which is a bilinear representation of the above damage curve to model the accumulation of damage in 1981 (Lee 2005). In doing so, it was assumed that the damage is a two phase process which includes crack initiation and propagation. This model therefore consists of two phases (phase I damage and phase II damage) in a linear manner as shown in Figure 2.6.

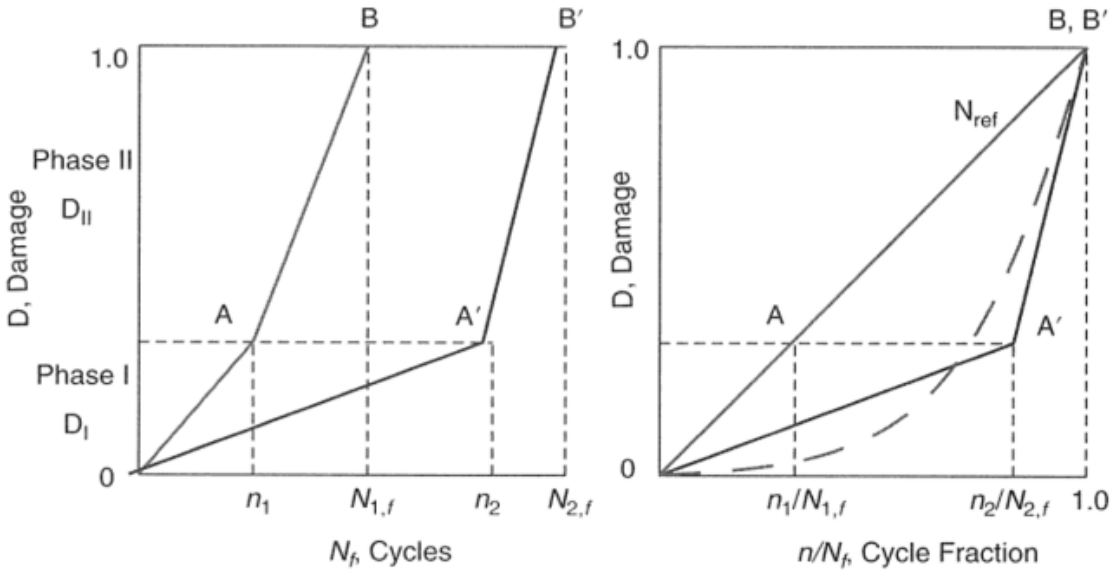

Figure 2.6 Double linear damage accumulation (Lee 2005)

Manson and Halford also found that the damage accumulation depends only on the total sum of the cycle ratios at each level, thus regardless of the loading sequence. In other words, the knee point location is not characterized by the crack initiation and propagation, and its coordinates are empirically determined as follows (Lee 2005).

$$\left[\frac{n_1}{N_{1,f}}\right]_{knee} = 0.35 \times \left(\frac{N_{1,f}}{N_{2,f}}\right)^{0.25} \tag{2.6}$$

$$\left[\frac{n_{2,f}}{N_{1,f}}\right]_{knee} = 0.65 \times \left(\frac{N_{1,f}}{N_{2,f}}\right)^{0.25} \tag{2.7}$$

It is also noted that these knee coordinates are not material dependant, thus would be the same for all materials. They only depend on maximum and minimum values.

2.1.2.3. Other Damage Models

Other approaches and theories, apart from linear and non linear damage models exist to model fatigue damage accumulation in metals. Examples of such approaches are energy based damage theories, and recently, the continuum damage mechanics approaches.

Energy based theories have mainly been developed since the late 1970s and have been recognized by their ability to combine damage caused by different types of loading, i.e. thermal cycling and creep (Fatemi 1998). They can also include multi-axial loads and mean stresses into consideration. Plastic strain energy (hysteresis energy), total strain energy (elastic and plastic), Bui-Quoc model and Niu theory are some of the examples of such models. Most of these energy-based models are energy versions of the LDR.

The Continuum Damage Mechanics (CDM) approach deals with the mechanical behavior of a damaging medium at the continuum scale. This first emerged as a model to treat creep damage problems and was later extended to model ductile plastic damage, brittle fracture and fatigue damage, and was further applied to composites and concrete materials (Fatemi 1998). One such theory is called the Nonlinear Continuum Damage Model (NCDM) proposed by Chaboche. Similar models were later developed following the same approach but different in the number and types of parameters used, as well as the applicability.

Even though many damage models have been developed to model accumulation of damage, none of them have proven universally acceptable while still accounting for all aspects of damage. Out of the aspects such as load dependence, load sequence, load interaction, nonlinear damage evolution and mean stress, one damage model generally addresses one or several of these factors only (Fatemi 1998). In addition, the applicability of each model greatly varies from one another making one model only effective for selected areas of applications. The LDR in this regard, due to its simplicity, seems the most widely used model for fatigue damage accumulation. In addition, the DLDR by

Manson and Halford is also recommended for use in engineering design to overcome the deficiencies associated with the LDR (Lee 2005).

2.1.3. Cycle Counting

During the service life of structures and their components, they undergo cyclic loading. This cyclic loading may be either constant amplitude or variable amplitude. If it is constant amplitude loading, then determining the amplitude and the number of cycles is straightforward with or without the presence of a mean offset load. For variable amplitude loading, determining cycles and their corresponding amplitudes are not straightforward. Various methods have been developed to determine the number of cycles in variable amplitude load histories. Determination of a cycle in this research is based on the identification closed hysteresis loops in strain histories, but in general, these methods can be applied to any other parameter, i.e., load, stress, torque, moment, and so on. By using a cyclic counting method, a complex variable amplitude load history can be converted to a number of discrete constant amplitude loading events.

One-Parameter Cycle Counting Methods

Examples of one parameter cycle counting techniques are level crossing, peak-valley and range counting. Details of these methods can be found in fatigue design and analysis textbooks such as Bannantine (1990) and Lee et. al (2005). These methods have been used over the years as a common method to extract number of cycles from a complex loading history. However, they have been identified as unsatisfactory since they fail to relate loading cycles to local stress-strain hysteresis behavior - an important factor that influences fatigue failure (Lee 2005).

Two-Parameter Cycle Counting Methods - Rain-flow method

Two parameter methods like rain-flow cycle counting method, have been widely accepted and used as reliable methods for better life predictions than one-parameter methods. Rain-flow method was originally developed by Matsuishi and Endo (1968) based on the analogy of rain drops falling on a pagoda roof (see Figure 2.7). This method defines cycles as closed stress-strain hysteresis loops. Several variations of the rain-flow counting method exist; original rain-flow method, range-pair counting, hysteresis loop counting, the "racetrack method", ordered overall range counting, range-pair-range counting and the Hays method ((Bannantine 1990) and reference therein). For this research, we adopt the rain-flow cycle counting technique with three-point counting method as per recommended by the ASTM and SAE standards (Lee 2005).

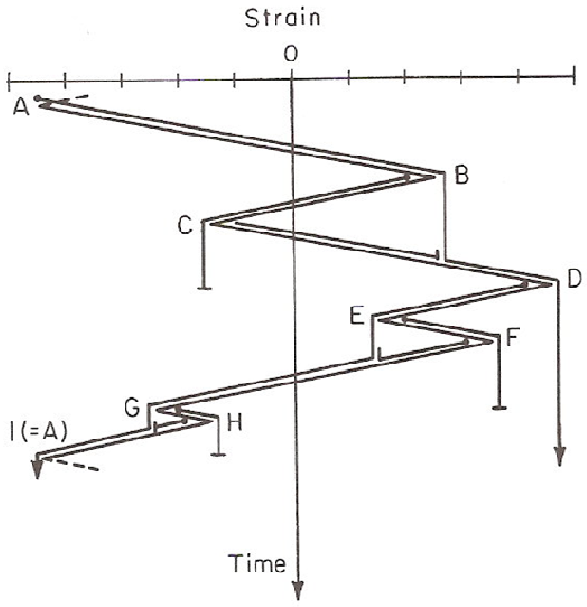

Figure 2.7 Rain-flow counting, "falling rain" approach (Bannantine 1990)

First, the load-time history is re-arranged to begin with the maximum peak or the minimum valley, whichever absolute magnitude is higher. Then, the three-point rain-flow counting rule is applied to every three consecutive load points ($S1$, $S2$ and $S3$) which

define the two consecutive ranges as $\Delta S1 = |S1 - S2|$ and $\Delta S2 = |S2 - S3|$. If $\Delta S1 \leq \Delta S2$, then one cycle from $S1$ to $S2$ is extracted and if $\Delta S1 > \Delta S2$, no cycle is formed (see Figure 2.8). This procedure is continued until a closed hysteresis loop is defined. The two points forming the cycle are discarded and the remaining points are connected to each other, and this is repeated until the remaining load points are consumed (see Figure 2.9).

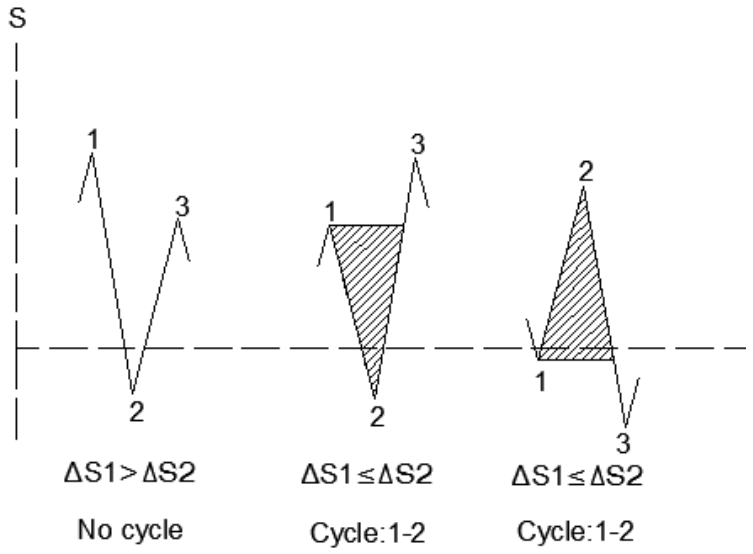

Figure 2.8 Rule of three-point rain-flow counting, redrawn from Lee (2005)

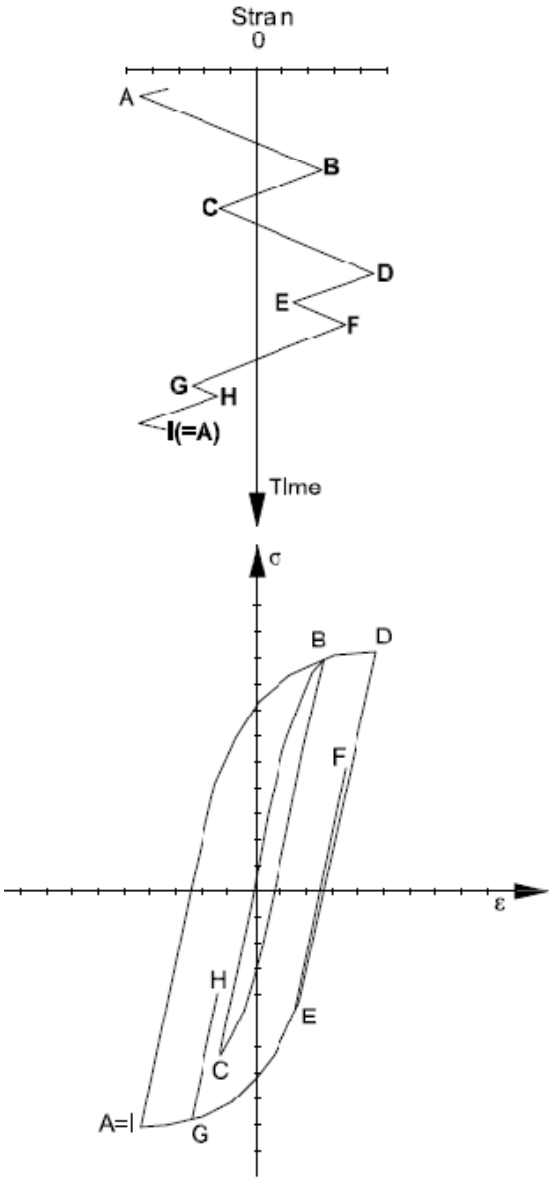

Figure 2.9 Material stress-strain response to given strain history, redrawn from Bannantine (1990)

2.2. Fatigue Analysis Methods

There are three main fatigue analysis methods in use, namely, (1) stress-life, (2) strain-life, and (3) fracture mechanics approach. Out of these three methods strain-life fatigue analysis method is used in this research. This section discusses the features of strain life analysis method in detail and briefs the use of the other two methods for comparison.

2.2.1. Strain-life fatigue analysis method

The anticipated behavior of the in-situ fatigue sensor in this research is based on the strain life fatigue analysis method. Strain-based fatigue analysis method assumes that a laboratory smooth specimen tested under strain control can simulate fatigue damage at the notch root of an engineering component. Equivalent fatigue damage is assumed to occur in the material at the notch root and in the smooth specimen when both are subjected to identical stress-strain histories (Bannantine 1990) (see Figure 2.10). Despite the fact that most engineering structures are designed for elastic nominal stresses, local stress concentrations can cause plastic strains to develop in their vicinity, thus causing more severe fatigue damage. The advantage of using the strain-life method is found in its ability to incorporate the elastic and plastic responses of the structural material. This method also provides a means to account for the cyclic plasticity at the root of a notch. Moreover, local strain-life approach is a good choice for cases where the load history is random (typical to highway bridges) and mean stress and load frequency are found to be important (Lee 2005).

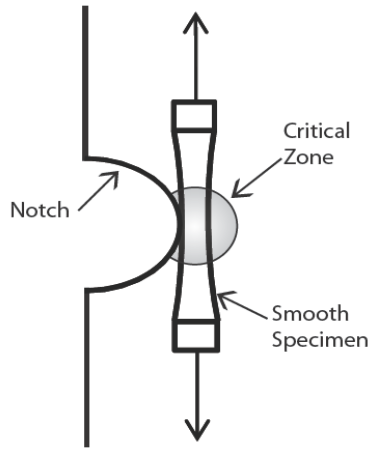

Figure 2.10 Equally stressed volume of material, redrawn from Bannantine (1990)

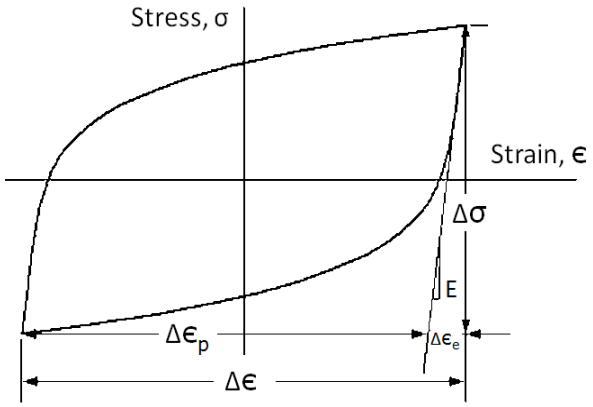

Figure 2.11 Typical cyclic stress-strain curve

When a material undergoes cyclic loading, it shows a hysteresis response as shown in Figure 2.11. The total width of the loop is the total strain range $\Delta\varepsilon$, and the total height of the loop is the total stress range $\Delta\sigma$. When stated in terms of amplitudes,

$$\varepsilon_a = \frac{\Delta\varepsilon}{2} \tag{2.7}$$

$$\sigma_a = \frac{\Delta\sigma}{2} \tag{2.8}$$

where ε_a is the strain amplitude, σ_a is the stress amplitude and the total strain ε is the sum of the elastic strain ε_e and the plastic strain ε_p. This can be written in terms of amplitudes as,

$$\frac{\Delta\varepsilon}{2} = \frac{\Delta\varepsilon_e}{2} + \frac{\Delta\varepsilon_p}{2} \tag{2.9}$$

and by applying Hook's law $E = {}^{\sigma}/_{\varepsilon}$ to the elastic term, it can be written as follows. E is the Modulus of elasticity

$$\frac{\Delta\varepsilon}{2} = \frac{\Delta\sigma}{2E} + \frac{\Delta\varepsilon_p}{2} \tag{2.10}$$

When a fully reversed stabilized cyclic true stress σ versus true plastic strain ε_p is plotted on a log-log plot, the approximated straight line can be used to develop a power law function as follows;

$$\sigma = K' + \left(\varepsilon_p\right)^{n'} \tag{2.11}$$

where σ is the cyclically stable stress amplitude, ε_p is the cyclically stable plastic strain amplitude, K' is the cyclic strength coefficient and n' is the cyclic strain hardening exponent.

Rearranging Equation 2.11 and using Hook's law for the elastic strain, the total strain ε can be written as,

$$\varepsilon = \frac{\sigma}{E} + \left(\frac{\sigma}{K'}\right)^{1/n'} \tag{2.12}$$

and by multiplying Equation 2.12 by 2, the hysteresis curve can be obtained.

$$\Delta\varepsilon = \frac{\Delta\sigma}{E} + 2\left(\frac{\Delta\sigma}{2K'}\right)^{1/n'} \tag{2.13}$$

Basquin ((Bannantine 1990) and reference therein) showed that stress-life data plotted linearly on a log-log scale provides the following relationship,

$$\frac{\Delta\sigma}{2} = \sigma_f'\left(2N_f\right)^b \tag{2.14}$$

where $\Delta\sigma/2$ is the true stress amplitude, $2N_f$ is the reversals to failure, σ_f' is the fatigue strength coefficient and b is the fatigue strength exponent (σ_f' and b are fatigue properties of the material).

Similarly, Coffin and Manson ((Bannantine 1990) and reference therein) found that plastic strain-life data can be linearized and presented by a power law function,

$$\frac{\Delta\varepsilon_p}{2} = \varepsilon_f'\left(2N_f\right)^c \tag{2.15}$$

where $\Delta\varepsilon_p/2$ is the plastic strain amplitude, ε_f' is the fatigue ductility coefficient and c is the fatigue ductility exponent (ε_f' and c are fatigue properties of the material).

The elastic strain amplitude $\Delta\varepsilon_e/_2$ of equation (2.9) can be re-written using the Hook's law as,

$$\frac{\Delta\varepsilon_e}{2} = \frac{\Delta\sigma}{2E} \tag{2.16}$$

and in terms of failure (using Basquin's equation (2.14)) as follows,

$$\frac{\Delta\varepsilon_e}{2} = \frac{\sigma_f^{'}}{E}\left(2N_f\right)^b \tag{2.17}$$

Substituting both elastic (Equation 2.17) and plastic (Equation 2.15) terms to Equation 2.9, the strain-life equation is obtained which is the basis of the strain-life analysis method adopted in this research:

$$\frac{\Delta\varepsilon}{2} = \frac{\sigma_f'}{E}\left(2N_f\right)^b + \varepsilon_f'\left(2N_f\right)^c \tag{2.18}$$

2.2.1.1. Mean Stress Effects

It has been experimentally shown that the presence of a non-zero mean normal stress influences the fatigue life of materials in crack initiation and propagation. According to experimental data, compressive mean stresses are beneficial to fatigue life whereas the tensile normal mean stresses are disadvantageous under conditions of long life regime where elastic strain is prominent (Bannantine 1990). Several mean stress correction methods exist to account for mean stress effects in fatigue life calculations. To estimate the mean stress effects on the fatigue life of the prototype fatigue sensor, Morrow's mean stress correction method and SWT's mean stress correction model have been applied in this research.

In Morrow's method the elastic term in the strain-life Equation 2.18 is modified by the mean stress σ_0 to obtain the following:

$$\frac{\Delta\varepsilon}{2} = \frac{\sigma_f^{'} - \sigma_0}{E}\left(2N_f\right)^b + \varepsilon_f^{'}\left(2N_f\right)^c \tag{2.19}$$

In the SWT model, both sides of the strain-life equation are multiplied by the maximum stress σ_{max} where $\sigma_{max} = {}^{\Delta\sigma}/_{2} = \sigma_f^{'}\left(2N_f\right)^b$ as per Equation 2.14 for fully reversed loading.

$$\sigma_{max}\frac{\Delta\varepsilon}{2} = \frac{\left(\sigma_f^{'}\right)^2}{E}\left(2N_f\right)^{2b} + \sigma_f^{'}\varepsilon_f^{'}\left(2N_f\right)^{b+c} \tag{2.20}$$

2.2.1.2. Stress Concentration and Neuber's Rule

To perform a strain-life analysis requires knowledge of stresses and strains at the notch root. This can be obtained either by taking strain measurements at the notch root, using finite element analysis or by using other methods to relate nominal stress/strain values to local stress/strain values, i.e. Neuber's Rule. For this study, both FEA method and Neuber's Rule have been adopted. Neuber's Rule states that,

$$K_t = \sqrt{K_\sigma K_\varepsilon} \tag{2.21}$$

where K_t is the theoretical SCF and K_σ and K_ε are stress and strain concentration factors respectively. This method has been proved for one notch geometry but generally assumed to be applicable to most notch geometries (Bannantine 1990).

For the nominally elastic behavior which is the case for this research, Neuber's Rule is modified with the Hook's law to obtain

$$\Delta\sigma\Delta\varepsilon = (K_t\Delta e)^2 E \tag{2.22}$$

where Δe and $\Delta\varepsilon$ are the nominal and local (notch) strain ranges, respectively, and $\Delta\sigma$ is the stress range. K_t is defined as the ratio of maximum (local) stress σ_{max} to nominal stress σ_{nom}. For the strain-life analysis, the modified Neuber's Rule (Equation 2.22) is

combined with the cyclic stress-strain curve (Equation 2.12) and with the hysteresis curve (Equation 2.13) independently to obtain local stresses at the notch root of the fatigue sensor.

2.2.2. Stress-Based Fatigue Analysis

The stress-based method, which is based on the fatigue limit of the material, is considered as the quickest and the cheapest method. This method works well for designs involving long life or HCF which account for little plastic deformation (stresses are mostly elastic) and constant amplitude histories as well, i.e. power transmission shafts, valve springs and gears. In addition, a wealth of data is available for variations of finish, loading conditions, environments and so on.

However, this method is completely empirical and lacks physical insights into the mechanism of fatigue. Further, it ignores the true stress-strain response of the material and the true stress-strain relationship at the notch root as well. This limits its application to long life predictions because plastic strains play a major role at short lives. It is also unable to distinguish between initiation and propagation of fatigue.

2.2.3. Fracture Mechanics Based Fatigue Analysis

Unlike the stress-based method, this method gives better insight into the actual mechanism of fatigue. Fracture mechanics based methods use linear elastic fracture mechanics with the related crack growth material properties to determine how fast a crack will grow, and the remaining life of the structure. The concept of stress intensity is involved in this method. This is the only method that deals with the propagation of fatigue cracks and characterizes the final failure due to fracture of the remaining cracked section. Fracture mechanics based methods can be utilized as a design tool in large

structures where propagation dominates fatigue life and which have small fraction of life which involves initiation, i.e. aerospace and nuclear industries. It can be utilized successfully in situations where components have pre-existing flaws.

No crack initiation is accounted in this method and the difficulty in determining the initial crack size, which has major influence in the predicted life, are some of the concerns. In addition, the need for stress intensity factors may become a problem for complicated geometries.

2.3. Fatigue Damage to Steel Bridges

According to Fisher (1998), fatigue damage to steel bridges occurs mainly due to the following reasons:

1. Flaws in fabricated steel structures such as filet welded details.

Partial penetration, porosity or inclusions, lack of fusion and undercut may lead to fatigue cracks.

2. Material flaws during fabrication

Material flaws may occur as a consequence of the manufacturing process and fabrication process of steel. In rolled shapes, flaws can occur from surface and edge imperfections, irregularities in mill scale, laminations and from mechanical notches due to handling, straightening, cutting and shearing.

3. Mechanical details

Mechanical details, such as drilled holes or punched holes, are prone to severe fatigue life compared to the bare rolled shape. Furthermore, punched holes are considered to give lower fatigue life than drilled, sub-punched or reamed holes because of the edge imperfections that occur during the punching process.

Overall, the fatigue life of a steel structure is determined by three factors, (a) the number of cycles of loading to which the member is subjected; (b) the type of detail under examination; and (c) the stress range at the location of the detail.

According to Fisher (1984), fatigue damages to steel bridges can be categorized mainly into (1) load induced fatigue damage and (2) distortion induced fatigue damage.

2.3.1. Load Induced Cracking

Stresses acting on the above mentioned defects may lead to fatigue cracking of the associated members. It is assumed that these stresses can be calculated and that the loads are the same as those indicated in the strength design of the members (Fisher 1998). Such damage associated with loads is called load-induced damage. See Figure 2.12, Figure 2.13, Figure 2.14 and Figure 2.15 for examples of load induced fatigue damage.

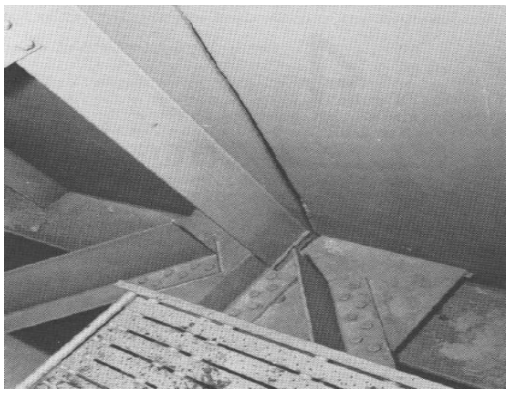

Figure 2.12 Cracked girder of the Lafayette Street Bridge (Fisher 1984)

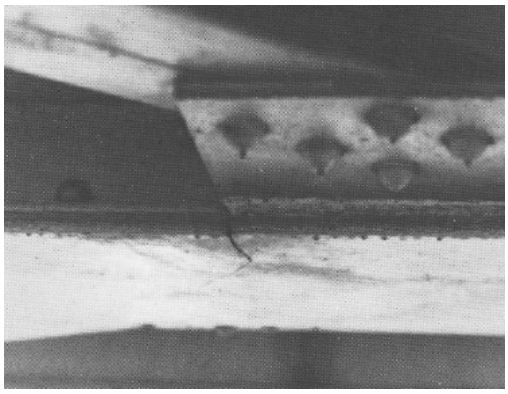

Figure 2.13 Crack at end of lateral connection plate, Vermilion River Bridge, Illinois (Fisher 1984)

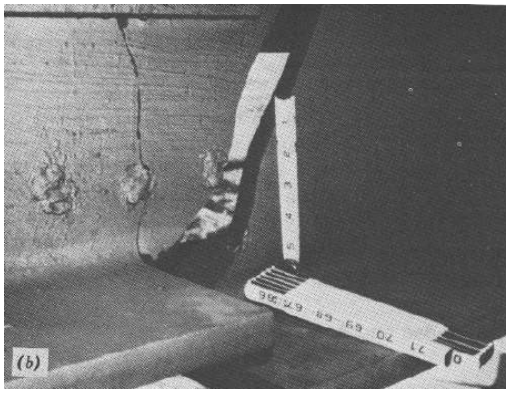

Figure 2.14 Cracks at the welded bolt holes, Country Highway 28 Bridge, Illinois (Fisher 1984)

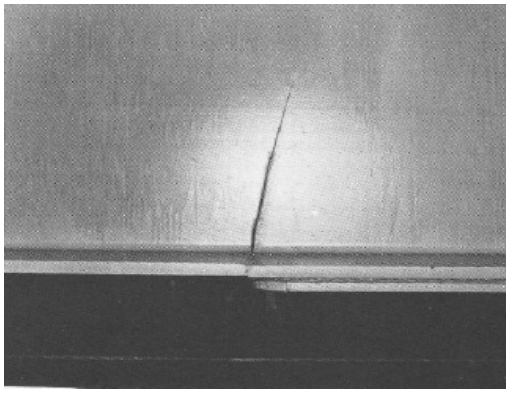

Figure 2.15 Cracked girder in Yellow Mill Pond Bridge, Connecticut (Fisher 1984)

2.3.2. Distortion-Induced Cracking

In some cases, fatigue damage may occur as a result of imposition of deformations, not necessarily due to loads. This type of fatigue damage, which is called distortion-induced cracking, arise as a result of relatively small out-of-plane deformations in local regions (Fisher 1998). This type of damage is mostly found in small web gaps and in different types of bridges such as suspension bridges, plate girder bridges, truss bridges, box girder bridges etc. It is important to know that this type of fatigue crack usually develops in planes parallel to the load-induced stresses and that after adequate flexibility is gained, these cracks may slow down or even stop. Therefore, distortion-induced damage is

considered as less severe than load-induced damage. See Figure 2.16, Figure 2.17, Figure 2.18, and Figure 2.19 for examples of distortion induced fatigue damage.

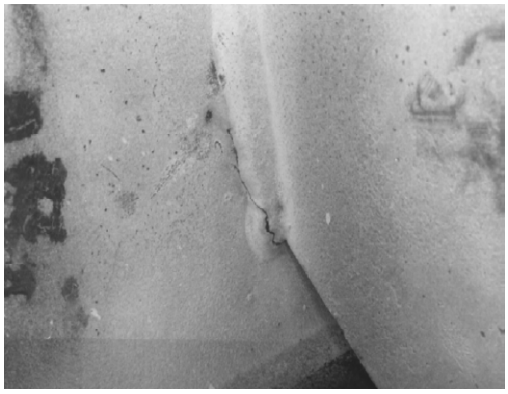

Figure 2.16 Web gap cracking at end of transverse connection plate (Fisher 1984)

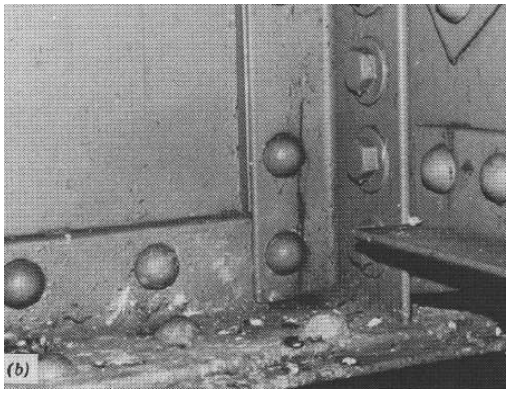

Figure 2.17 Cracking at diaphragm of riveted bridges: cross-frame connection angle (Fisher 1984)

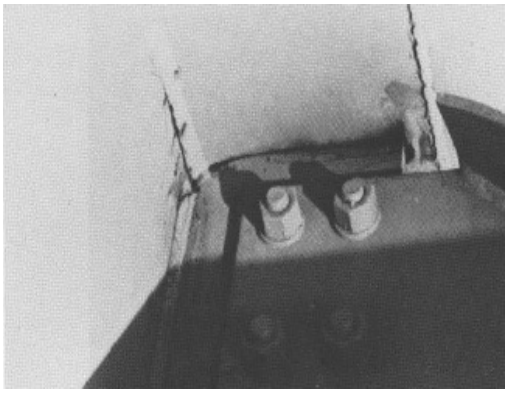

Figure 2.18 Cracking in web gap at floor-beam connection, Prairie Du Chien Bridge, Iowa (Fisher 1984)

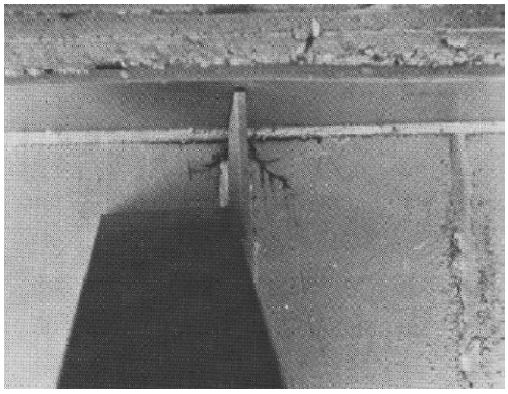

Figure 2.19 Fatigue cracks along flange-web weld toe at end of diaphragm connection plate (Fisher 1984)

2.4. Current NDE Methods for Fatigue Monitoring

2.4.1. Introduction

Different types of Non Destructive Evaluation (NDE) methods are being developed to detect fatigue damage in steel components and structures. These NDE methods are based on different approaches and utilize diverse technologies for fatigue detection. They can be global (methods that focus on the entire bridge) or local (methods that focus on a local area of interest, i.e. crack size, shape and direction).

2.4.2. Non-Strain Based NDE Methods

Visual inspection, the only routine method for fatigue inspection in steel bridges in the US (Gongkang 2004), is not very successful due to the nature of the fatigue damage. The other popular global diagnostic method is dynamic model testing, most commonly by using accelerometers. Limitations of dynamic methods (Doebling 1998) are the cost, limited coverage (unless the structure is densely instrumented which increases the cost) and the noise. Numerical analysis methods, such as FEA can also be used as a global method (Bhargava 2008). The limitations, such as (1) the cost and (2) the reliability of the FE models to cover the inconsistencies between nominal and as-built strength and stiffness, are major concerns (Gongkang 2004). The image technology, which uses high resolution images from Couple Current Devices (CCD) or CCD cameras, is gaining popularity. They can detect displacements of a structure at points of interest and largely cut the cost while covering a larger area of the structure at the same time.

Local methods can be found either as non-strain-based methods and strain-based methods. Examples of non-strain based methods include ultrasonic testing, infrared and thermal Imaging, acoustic emission, eddy current methods, dye penetrant inspection, magnetic particle testing, and radiographic testing. Examples of some strain-based methods are fiber optic sensors, piezoelectric sensors and various crack propagation gages.

UltrasonicTesting

Ultrasonic testing is commonly used in aerospace and automotive industries and consists of four different types of waves: longitudinal or compressive waves, compressive and shear waves, surface or Rayleigh-waves, and plate or Lamb-waves. Out of these four,

surface or Rayleigh-waves are considered successful in fatigue crack detection in welds (Gongkang 2004). According to Fisher (1998), ultrasonic testing method can be used for any thickness of plate over 0.118 in. (3 mm) and may even detect small embedded cracks or surface cracks when properly calibrated. However, the variations in the surface roughness and parts with complicated geometry (Gongkang 2004) may affect the accuracy. Gongkang (2004) claims that ultrasonic testing is most successful for detecting discontinuities that are oriented perpendicular to the direction of propagating sound wave and therefore can be used in combination with Radiographic Testing (RT) for optimum results. However, considerable experience is required to deploy this method because of the difficulty in visualizing the orientation and the size of the cracks (Fisher 1998). Recent developments of ultrasonic testing can be found in research projects sponsored by FHWA. An example of such a system is called the New Ultrasonic and Magnetic Analyzer for Cracks (NUMAC), which has shown to be able to detect and quantify fatigue cracks in steel bridges even though they may covered with paint (Chase 1998).

Infrared and Thermal Testing (IR)

Infrared and Thermal Testing (IR) is used as another NDE method to detect fatigue cracks in metals. An IR scanning system can measure and view temperature patterns based upon temperature differences as small as a few 100ths of a degree Centigrade and it can be performed during day or night (Moore 1998), depending on environmental conditions and the type of application. According to Chase (1998), Small Business Innovative Research (SBIR) has developed a high-resolution thermographic imaging system to detect surface-breaking fatigue cracks. This forced diffusion thermography method uses a high-wattage light to heat the desired surface. A pattern of hot and cold

regions is created on that surface as a result which can be indentified via thermographic imaging system and in the presence of a crack, the characteristic pattern is observed.

Acoustic Emission (AE)

The principle behind the Acoustic Emission (AE) is that high frequency stress waves are generated by the rapid release of strain energy generated within a material during crack growth, plastic deformation, phase deformation, etc. ((Son 2004) and reference therein). Piezoelectric sensors are usually installed around the area to be inspected and the stress waves generated as a result of crack propagation can be assessed by the sensor output. The advantage of this method is its high sensitivity to detect minute cracks and material discontinuities. However, the cost and the call for complex equipment are considered among the disadvantages of using AE in bridge health monitoring schemes. Background noise generated from joint friction and traffic are also of great concern (Gongkang 2004) together with the no-repeatability - AE only detects the flaws at the time of operation.

Eddy Current (EC) Method

Eddy Current (EC) method follows the electromagnetic principle and is used to detect minute surface cracks in complex geometries by detecting the leakage of the electromagnetic flux due to flaws. Limitations associated with EC method are material conductivity, surface accessibility, surface finish, and penetration depth. However, the recent sensor designs in the aircraft industry seem overreach such boundaries; i.e. Rakow et al. (2007) has designed an in-situ sensor made from two layers (active and passive) of inter-wound Cu coils printed on a flexible Kapton layer that is capable of detecting cracks in thru-holes of multi-layered metallic joints in aircrafts.

Dye Penetrant Inspection (DPI)/ Liquid Penetrant Inspection (LPI)

Dye Penetrant Inspection (DPI) or Liquid Penetrant Inspection (LPI) is one of the low cost methods to detect surface breaking fatigue cracks in in-service bridges. DPI, which is based on capillary action, can only be applied to non-porous materials and the main advantage is that it can detect flaws regardless of their size, configuration, internal structure, chemical composition or the orientation (Son 2004). However, no judgment can be made about the depth of such flaws and only the surface breaking flaws that are not contaminated with dust or rust can be detected (Gongkang 2004).

Magnetic Particle Testing (MT)

Magnetic Particle Testing (MT) is another inspection method used to identify or confirm fatigue cracks, especially in welds. This method is mostly used to detect surface cracks. However, sub-surface cracks also can be detected if the depth is not too large. The MT procedure involves surface preparation, magnetization, application of particles, removal of excess, post cleaning and demagnetization (Gongkang 2004). Fine magnetic particles when sprayed on the component will detect distortions in the steel that occur as a result of a distorted magnetic field due to cracking. In the presence of damage, these particles form clusters at crack tip locations (Fisher 1998). These magnetically held clusters of particles generally indicate its location, size, shape and extent (Son 2004). The major limitation of this method is that non-ferromagnetic materials such as aluminum (Al) alloy, magnesium (Mg) alloy, copper (Cu) alloy, lead (Pb), titanium (Ti) alloy and austenitic stainless steels cannot be tested using MT.

Radiographic Testing (RT)

Radiographic Testing (RT) is based on differential absorption of penetration radiation: X or gamma ((Son 2004) and reference therein). The variations in absorption caused by the material flaws can be detected by the unabsorbed radiation which passes through the material when recorded on photosensitive paper and viewed on a fluorescent screen. RT is mostly applied to weld flaws to inspect porosity, lack of fusion and slag, etc (Son 2004). It is therefore required that both surfaces of the specimen are accessible to apply this method. According to Gongkang (2004), the selection of RT depends on the type, thickness and geometry of the steel and the required sensitivity of the test. However, Son (Son 2004) claims RT is slow, expensive and requires heavy equipment for operation.

2.4.3. Strain Based NDE Methods

Strain-based NDE methods use strain as the detecting parameter to estimate fatigue damage. Some examples include piezoelectric sensors, fiber optic/fiber brag sensors and most commonly, strain gages.

Piezoelectric Sensors

The use of piezoelectric materials has shown promising results in detecting fatigue cracks. Zhang (2006a) developed a surface-mount piezoelectric paint sensor, which is a polymer-based piezoelectric paint that can be directly deposited onto the surface of host structures. Another benefit of piezoelectric paint sensors is that they can be used as self-powered sensors because the electric charge generated by piezoelectric materials in response to mechanical loads can be measured without the need for external power excitation. However, the limitation of this sensor is that it can only detect dynamic strain.

Fiber-Optic and Fiber Bragg Sensors

The use of fiber-optic sensors in SHM is gaining popularity for many reasons. Their light weight, flexibility in size, and resistance to electromagnetic fields have made them popular over other conventional sensors (Casas 2003). They can be bonded to steel structures or embedded in composites for real time monitoring in in-service structures. The Blue Road Research team has developed fiber-optic sensors for civil infrastructure and aerospace applications, as well as composites and pressure vessels. Calvert (2004) used fiber Bragg grating strain sensors to detect bridge response due to dynamic input. The objective is to provide direct strain input to the algorithm in order to generate more accurate mode shapes and modal parameter calculations. The advantages of Fiber Bragg strain sensors are higher temperature range up to 400°C (Schulz 1998), multiplexing capabilities, environmental ruggedness, ability to support demodulation, and reliability in dynamic strain measurements. However, these Fiber Bragg strain sensors require expensive instrumentation and data processing to detect wavelength shift (Lee 2001). Considering the fatigue detection, another development to the fiber optics, namely intensity-based optical fiber (IBOF) sensors, were developed by Lee (2001) for real-time monitoring of stiffness changes due to fatigue damage in composite structures. However, the issues related to fabrication and strength of the optical fibers due to accumulation of damage is an open research area.

Strain Gages and Crack Propagation Sensors

Strain gages are still widely used as reasonable indicators of structural health and help to determine damage due to fatigue (Chan 2001; Li 2001; Mohammadi 2004). Limitations include finding the correct location or "hot-spot", installation and maintenance

difficulties and power supply. Wireless strain gages deploy the same principle of typical strain gages but use wireless transmission of the signal. In addition, battery power, on board memory storage and on board bridge completion resistors are some of the features of wireless strain gages. Crack Propagation Gages, a development of typical strain gages, provide a convenient method for indicating the rate of crack propagation when applied to a structure. These gages consist of a number of resister strands that are connected in parallel (Vishay 2008). Progressive fracture of the strands due to crack propagation creates open circuiting while increasing the total resistance, which can be measured by using a strip chart recorder. *CrackFirst* is another recently developed patented fatigue sensor to detect fatigue damage in welded structures (Zhang 2006b). Based on fracture mechanics principle, this sensor is made of a thin steel coupon with a pre-crack at the center and is meant to be attached to a structure adjacent to the critical weld detail. When the structure undergoes cyclic loading, the crack propagates. This is especially developed for welded joints, where the presence of flaws acts as fine cracks at the weld toe and largely eliminates the crack initiation phase. FHWA has developed a device named the Passive Fatigue Load Measurement Device with a similar principle for the purpose of estimating the fatigue loads in bridges. This device has two pre-cracked Al fatigue coupons that strain along with the bridge. Due to the difference in grades of these coupons, cracks will grow at different rates. By periodically measuring the crack length using another meter for a length of time, the fatigue life of the bridge under variable amplitude loading can be determined (Chase 2005; Chase 1998).

2.5. Inspecting and Retrofitting Fatigue Damage: State-of-the-art Practice

2.5.1. Inspection of Fatigue Cracks

Proper detection and action against fatigue cracks are important to ensure the safety of the steel bridges. If fatigue cracks are found, then the engineers are responsible for taking necessary actions to prevent crack propagation and damage to the entire structure. Fisher (1998) shows the following protocol for fatigue crack investigation:

- Perform a fatigue life analysis to determine the remaining fatigue life based on load-induced fatigue. Such an analysis would identify details that have minimum or no remaining fatigue life. In such cases, a physical inspection of the structure will be carried out. It is advised to measure local strains to better estimate load induced stresses since global strains obtained from conventional structural analysis methods are generally considered conservative.
- Utilize shop drawings of the members to identify the details that are susceptible to distortion-induced fatigue.
- If a need of a physical inspection of the structure is identified, it should be carried out by trained personnel.
- If cracks are found, appropriate repair methods must be carried out with subsequent inspection procedures.

As a result of the previous examinations, one of the following decisions will be made:

- The structure is deemed to be unsafe for the intended use, and it must be shut down.
- The structure is deemed to be safe, providing that load levels are reduced.

- Because of redundancy, the structure is deemed to be safe at existing load levels, even though cracks have been identified. It is possible that although remedial action is not required, continued monitoring of the structure is indicated.

In cases where the structure is not shut down for use, it is advised to investigate the causes of cracking before taking any action. It is important at this point to look for the factors which activate and develop fatigue cracks: large number of stress ranges, severe stress concentrations, impact, out-of-plane distortion, corrosion, and defects in fabrication and welding. Generally, engineers/inspectors identify the possible causes from their previous knowledge and experience as well as from the available information of other fatigue damaged bridges.

2.5.2. Repair of Fatigue Cracks

Repair of fatigue cracks, according to Fisher (1998), may result in an adequate solution to fatigue cracking only when the steel quality is appropriate for both present and future service conditions. Most importantly, welding repair has rarely been found successful, thus it should be carried out only when no other solution is available. Fisher further lists the measures that have been employed successfully to steel structures as follows (in the order from best to worst):

- Place cover plates on both sides of the cracked plate and attach them with pre-tensioned high-strength bolts. This solution provides a load path for forces while restricting movement of the crack surfaces during fatigue loading.
- Drill a hole at the crack tip and fill it with a pre-tensioned high-strength bolt.

Drilling a hole at the end of the crack tip blunts the tip, thus greatly increasing the force required to drive a crack. The pre-tensioned bolt that introduces a local compressive stress masks the tensile stress, further preventing the crack growth.

- Cut out and re-fabricate parts of elements in order to reproduce the same conditions that existed at the crack site before cracking occurred.
- Air-arc gouge the crack and fill the gouged area with weld metal. Then grind away weld reinforcement and polish smooth. Afterwards, inspect for any weld defects by using ultrasonic and X-ray inspection technology.
- Peening the toe of a weld termination that is perpendicular to the stress range is considered an effective way to avoid the growth of small cracks (less than 0.118 in., or 3 mm, deep). This procedure introduces compressive residual stresses and changes the size of the weld toe crack as well.
- Another method is to use the gas tungsten arc re-melting that effectively removes micro-discontinuities at the weld toe thus decreasing the stress concentration. This measure is more accepted for shop use and new construction due to the difficulty in executing in-service bridges.

In addition to the above measures, any measures that lower the stress ranges in the area around the crack are considered helpful. In an extreme case, the total replacement of the cracked element will be carried out. Special attention must be paid to the steel grade of the new element, its size and the connection details. It is important to check for the stiffness changes of the replaced element to make sure no new problems are created elsewhere as a consequence.

CHAPTER 3. THE USE OF FINITE ELEMENT SIMULATION FOR FATIGUE LIFE PREDICTION

Numerical analysis plays an essential role in the design and development of the in-situ fatigue sensor. Fatigue testing of the sensor requires a repeated number of loading cycles to be applied to its attached specimen, typically up to 10^8 cycles. Testing multiple specimens is, therefore, time-consuming depending on the excitation frequency and the limitations of the testing apparatus. In order to optimize the sensor design, fatigue response needs to be observed for varying test parameters, such as geometric, material and loading, which would expand the test matrix while further increasing testing time. Under these circumstances, FEA methods have been successfully utilized in this research. FEA methods were used at different stages of the design; to identify the most appropriate notch geometry and configuration, to predict the material response, to identify the sensitivity parameters and to mitigate the experimental limitations pertaining to the time spent on accumulating large numbers of cycles.

This chapter discusses the use of FEA for fatigue life prediction in general and specific to this research. First it investigates FE simulation software available in the market for fatigue life prediction with some examples, and then examines the validity of the fatigue tool in ANSYS FEA software in detail as a possible fatigue life prediction tool to be used in this study. In doing so, the Society of Automotive Engineers (SAE) experimental data of a keyhole specimen have been used as a validation. Issues related to ANSYS Workbench (WB) fatigue tool are identified and discussed for this particular

problem. The last section discusses how FEA has been utilized in this research for fatigue life prediction of prototype in-situ fatigue sensors.

3.1. An Overview of the Current FE-Based Fatigue Analysis Methods with Special Reference to ANSYS

3.1.1. Current Fatigue Simulation Methods

Generally, FE based fatigue analysis is a post processing operation preceded by linear or non-linear FE analysis. The analysis results are then imported to a fatigue solver together with fatigue material models such as stress-life (S-N) curves or strain-life (E-N) curves. The next step is to define loading cycles either by importing loading histories directly from a DAQ or by generating them within the fatigue solver.

As a result of a market search for fatigue solvers, the following products were revealed. These are only a few examples available on the market used by various industries for fatigue life analysis and design optimization of mechanical components and structures. A brief overview of each method is presented.

- ***FEMFAT***- *Finite Element Method/FATigue* from MAGNA POWERTRAIN (http://www.femfat.com/)
- ***fe-safe*** from safe technology limited (http://www.safetechnology.com/)
- ***MSC Fatigue*** from MSC Software Corporation (http://www.mscsoftware.com/)
- ***NEi Fatigue*** (***winLiFE***) –Nastran Finite Element Analysis and Simulation Software from NEi Software, Inc. (http://www.nenastran.com/)

FEMFAT performs fatigue analysis in combination with widely used FE software such as *ANSYS, ABAQUS, NASTRAN* and *I-DEAS*, etc. This software is developed primarily for the automotive industry and is based on the stress-life approach. It supports multi-axial fatigue, fatigue in weld seams, spot weld and self piercing rivets, etc. Fatigue

analysis under thermo-mechanical loading is also supported. Fatigue results can be viewed through the *VISUALIZER* module or by FE post-processors in terms of damage and safety factors. The main disadvantage is that it does not include local strain-life analysis method, which is of main interest to this research.

The *fe-safe* fatigue solver consists of most of the above mentioned features and a wider range of import options. In addition to the stress-life approach in multi-axial fatigue, it also includes strain-life approach with SWT and Morrow mean stress corrections for uniaxial fatigue.

MSC Fatigue is similar to *FEMFAT* and *fe-safe* and supports widely used FE software such as *ANSYS, ABAQUS, Adams, Marc* and *MSC Nastran*. Advantages include crack growth and strain-life fatigue analysis capabilities. Strain-life fatigue analysis capabilities have been verified together with stress-life and crack growth analyses methods in the *MSC Fatigue* User's Guide using SAE experimental data for the key-hole specimen. Details of the SAE experimental data and the keyhole specimen will be discussed in the following section.

NEi Fatigue (*winLiFE*) is another FE based fatigue solver which has the least number of features compared to *FEMFAT, fe-safe* and *MSC Fatigue.* This also includes strain-life fatigue analysis with the SWT mean stress correction method.

3.1.2. Fatigue Simulation Using ANSYS

The above discussed commercial fatigue solvers are relatively expensive and the possibility and flexibility to utilize them in this research is limited. As an alternative, the educational version of ANSYS FE software, which is available under university license, was chosen. Fatigue capabilities in ANSYS were investigated prior to applying it for

fatigue life estimations. Fatigue capabilities in both ANSYS Classic 11 and ANSYS WB 11 have been explored.

ANSYS Classic 11

ANSYS Classic 11 has very limited fatigue analysis capabilities. It uses *ASME Boiler and Pressure Vessel Code* Section III (and Section VIII, Division 2) for guidelines on range counting, simplified elastic-plastic adaptations, and cumulative fatigue summation by Miner's rule (ANSYS 2009) . This criteria is mostly suitable for the pressure vessel industry (Hancq 2000). Its output options are limited, thus they do not allow flexibility for modifications.

ANSYS WB 11

The ANSYS WB approach to fatigue analysis includes three generic steps, or three component architectures, called *Material Library*, *Fatigue Engine* and *Damage Engine* (Hancq 2000).

1. *Material Library* provides the functionality to store, manipulate and query the fatigue properties of a given material. Material data is entered as a scalar or a vector.
2. *Fatigue Engine* measures fatigue damage based on a single input stress and temperature state. This information could be in the form of available life, damage, or safety factor for a given loading scenario and relies on:

   - a fatigue curve that contains material properties from the *Material Library*

   - a set of procedures that does actual fatigue calculations based on different engines such as S-N Engine, which conducts a stress-life analysis or E-N Engine for strain-life analysis.

3. *Damage Engine* calculates the fatigue damage for a given loading history where multi-axial stress and temperature may vary over time. This relies on three main pieces:

   - cycle counting

   - finding partial damage estimates, and

   - summing partial damage to find the total accumulated damage

The procedure for strain-life fatigue analysis follows the following steps in ANSYS WB.

- Select the analysis type
- Select the loading type – zero based/fully reversed/ratio/history data

ANSYS WB supports 3 loading types ((1) constant amplitude, proportional, (2) constant amplitude, non-proportional, and (3) non-constant amplitude, proportional)

- Mean stress theory – none/SWT/Morrow
- Multi-axial Stress correction factors – based on component stresses (x, y, z, xy, yz, xz)/equivalent (Von Mises)/signed Von-Mises/max. shear/max. principal/abs. max. principal
- Fatigue strength factor (K_f) – strength reduction factor to adjust strain/stress life curves to represent "real world" settings
- Scale factor – sets scale of the load magnitude

According to WB literature on the fatigue tool (Browell 2006), the total strain inputs (elastic and plastic) to the strain-life equation are obtained first by assuming nominal elastic response and then by using the Neuber's rule to relate local stress/strain to nominal stress/strain at the stress concentration location and, finally, by simultaneously

solving Neuber's equation along with cyclic strain equation. It considers the elastic SCF (K_t) = 1 at the beginning and assumes it can capture any stress concentration effects through refinements of the mesh.

3.2. Investigate the Validity of ANSYS WB Fatigue Module Using SAE Experimental Data

3.2.1. Introduction to the SAE Experiments

The goal of this subtask is to compare ANSYS WB fatigue module results with experimental data obtained and published by the *Cumulative Fatigue Damage Division* of SAE - *Fatigue Design and Evaluation Committee* (Tucker 1975). The experimental data extracted from this SAE report consists of the documentation of the test program: analysis of the service load histories, the specimen design, a list of basic material and component properties and analysis of the variable amplitude experimental results.

The Load Histories

Three load histories were used by SAE to represent a wide variety of actual operating conditions in the automotive industry: suspension history, which has primarily compressive mean stress; bracket history with nearly constant mean stress; and transmission history, which has drastic change of mean stress (Tucker 1975). For this investigation only the constant amplitude load histories were used.

The Test Specimen

The SAE test specimens (see Figure 3.1) were made from both U.S. Steel's Man-Ten and Bethlehem's RQC-100 steel and were cut from a 0.375 in. hot rolled plate. The hole was drilled and seamed with no edge penetration and was saw cut from one side to create the notch.

Loads were applied to the specimen through a close tolerance mono ball fixture which was capable of providing both tension and compressive stresses (Tucker 1975). This loading configuration would cause both axial and bending stresses at the notch (see Figure 3.2).

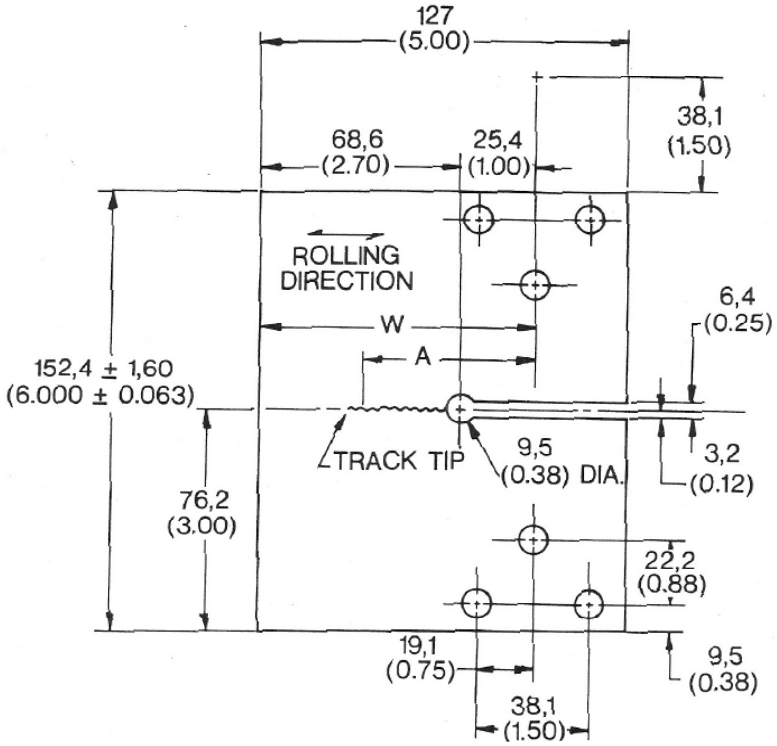

Figure 3.1 Test specimen design, mm (in.) (Tucker 1975)

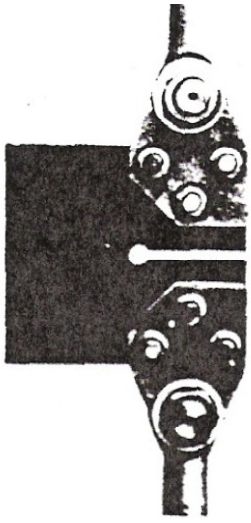

Figure 3.2 Loading fixture (Tucker 1975)

Material Properties

The following materials properties from SAE report (Tucker 1975) were used in the ANSYS WB FE analysis.

Table 3.1 Material Properties of Man-Ten and RQC-100 Steels (Tucker 1975)

Monotonic Properties	**Man-Ten**	**RQC-100**
Modulus of Elasticity (E), psi	29,500,000	29,500,000
Tensile Yield Strength (S_y), psi	47,000 (C-4)[a]	112,000 [T](C-6)[a]
Tensile Ultimate Strength (S_u), psi	82,000 (C-4)[a]	119,000 [T](C-6)[a]
Cyclic Properties		
Fatigue Strength Coefficient (σ_f'), psi	133,000	168,000
Fatigue Strength Exponent (b)	-0.095	-0.075
Fatigue Ductility Coefficient (ε_f')	0.26	1.06
Fatigue Ductility Exponent (c)	-0.47	-0.75
Cyclic Strength coefficient (K'), psi	160,000	167,000
Cyclic Strain Hardening Exponent (n')	0.193	0.1

[a]C-4 Results from L. E. Tucker, Deere & Company, SAE committee correspondence
[a]C-6 Results from D. Parks and R. M. Wetzel, Ford Motor Company, SAE committee correspondence
T Transverse to rolling direction

3.2.2. Modeling and Simulation of the SAE Keyhole Specimen in ANSYS WB

The simulation was carried out in two steps. First, SAE experimental results were compared with ANSYS WB results directly based on the life data. It is important here to identify how *life* is defined in either case.

ANSYS WB fatigue module defines *life* as follows.

For a constant amplitude loading, *life* is a result contour plot that represents the number of cycles until the part will fail due to fatigue. If the alternating stress is lower than the lowest alternating stress defined in the S-N curve, the *life* at that point will be used (ANSYS 2009).

SAE defines *life* as the fracture *life* or the total reversals ($2N_f$) to failure (Note: The crack initiation is arbitrarily defined in SAE as an average crack of 0.1 in.). Therefore, for this analysis SAE results were divided by two to compare with ANSYS

results which were given in cycles (N_f). Crack *initiation life* in SAE results were compared instead of their *fracture life*. This is because it was obscure what "failure" in the ANSYS fatigue module denotes in terms of the fatigue life: its crack initiation life or the total fracture life.

The FE Model

The FE model was created using ANSYS WB following the geometry of the SAE test specimen. Due to its symmetricity about the horizontal center line, only the top half of the specimen was modeled using the *Design Modeler* interface in ANSYS WB.

Meshing

The model was meshed using the WB automatic meshing tool with *mechanical* option and PLANE183, 8 node plane stress quadratic triangle and quadratic quadrilateral elements. By including mesh sizing with sphere of influence at the vicinity of the notch and refinement at its edge, a fairly reasonable mesh was created with approximately 6,500 elements and 20,000 nodes.

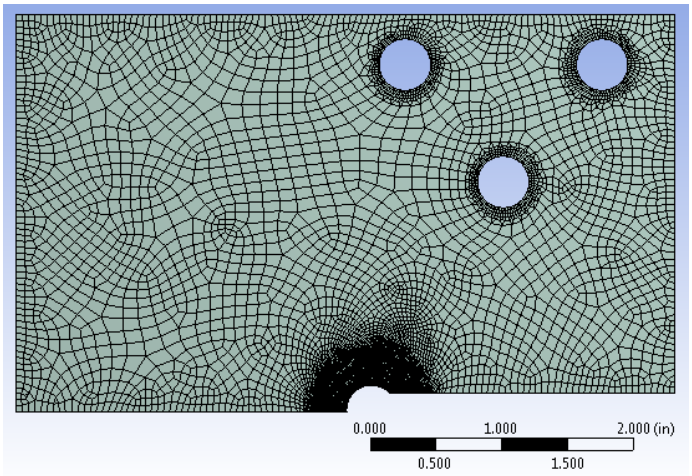

Figure 3.3 Meshed half model of the SAE specimen in ANSYS WB

Boundary Conditions, Loading and Analysis Type

Boundary conditions were set to (1) avoid rigid body motion by setting displacement $x = 0$, $y = 0$ at the bottom left vertex and (2) symmetry boundary conditions along the lower edge of the model by setting displacement $x = 0$ and $x = free$, as shown in Figure 3.4. Two loading cases were considered. In the first case, the load was applied as a point load to the edges of the bolt holes (see Figure 3.4, left) and in the second case, the load was applied as a line pressure (see Figure 3.4, right). Both cases were then analyzed as a 2D plane stress problem.

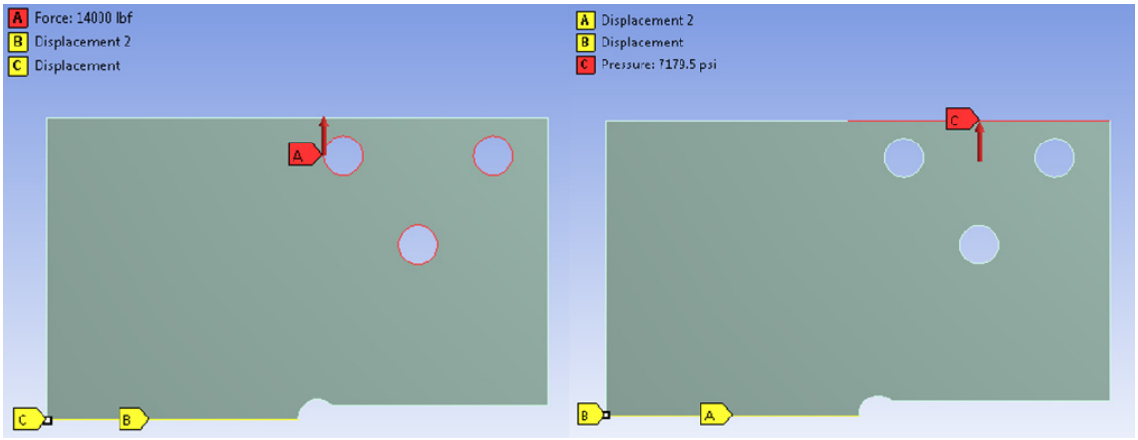

Figure 3.4 Analysis settings: BC's and two loading options

WB Fatigue Module Options Used in the Analysis

The WB environment carries out fatigue calculations as a post processing task. For this analysis, strain based method was selected as the analysis type. The majority of the fatigue loadings were fully reversed except for a few cases where different stress/loading ratios ($R = \sigma_{min}/\sigma_{max}$) were used according to the SAE constant amplitude experiments. No mean stress theory was needed for fully reversed ($R = -1$) cases. Morrow's mean stress theory was used for other R ratios ($0 \leq R \leq 1$). Fatigue life was

calculated based on the Von-Mises component of stress since the stress field is multi-axial and the infinite life was kept at the default of 10^9 cycles.

Under the *Engineering Data* interface, the above listed (Table 3.1) monotonic and cyclic material properties were entered under a new material labeled as *MAN-TEN_V1,* for Man-Ten steel, and *RQC-100* for RQC-100 steels.

Simulation Results

Finite element models were analyzed for different loading cases following the SAE constant amplitude experiments. Results are recorded in Table 3.2 and Table 3.3. Following figures show equivalent stress, normal stress and fatigue life for Man-Ten steel for two types of loading.

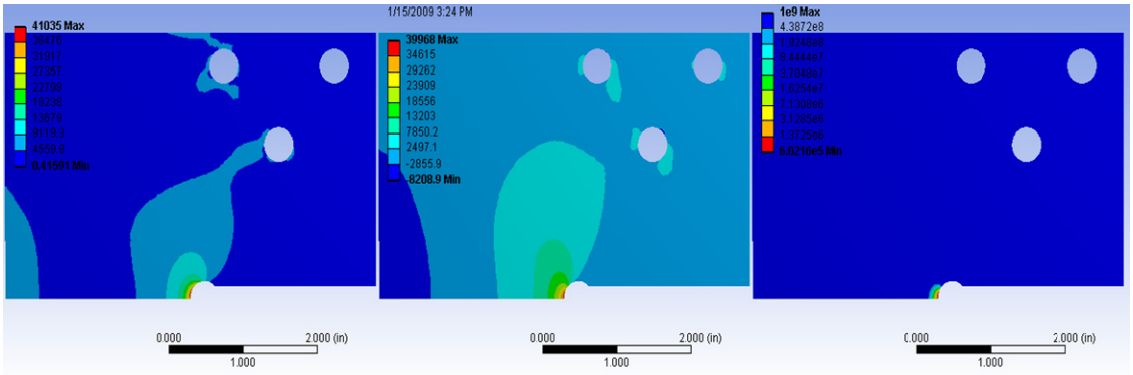

Figure 3.5 Equivalent Stress, normal stress and life results for 2000 lb. point load

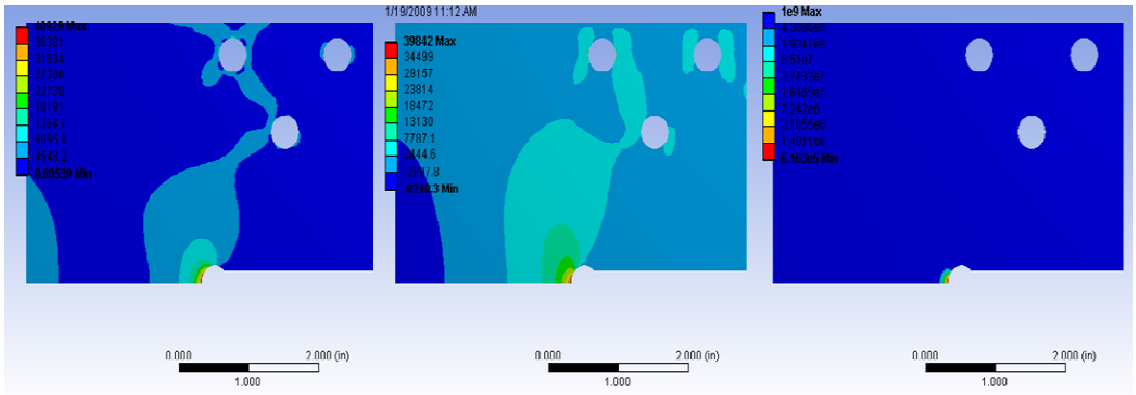

Figure 3.6 Equivalent stress, normal stress and life results for 2051.3 psi line pressure (2000 lb. equivalent point load)

Comparison

Table 3.2 Constant Amplitude Fatigue Test Results – Man-Ten Steel

Load (lb.)		+/- 14,000	+/- 7,000	+6030 +995	+5030 +995	+/- 5000	+/- 2000
Total Life Cycles	SAE Experimental (crack Initiation)	72	1,790	178,500	1,131,500	7,200	>1,059,500[c]
	ANSYS Point Load	46	698	72,133[a]	258,000[b]	2,982	495,930
	ANSYS Line Pressure	46	703	72,761[a]	260,650[b]	3,004	501,720

[a]max = + 6030, min = + 995 (R=0.165 w/ Morrow's mean stress correction) - not plotted in
[b]max = + 5030, min = + 995 (R=0.198 w/ Morrow's mean stress correction) - not plotted in
[c]Approximate value taken at 0.38 in crack (should be at 0.1 in crack – by definition)

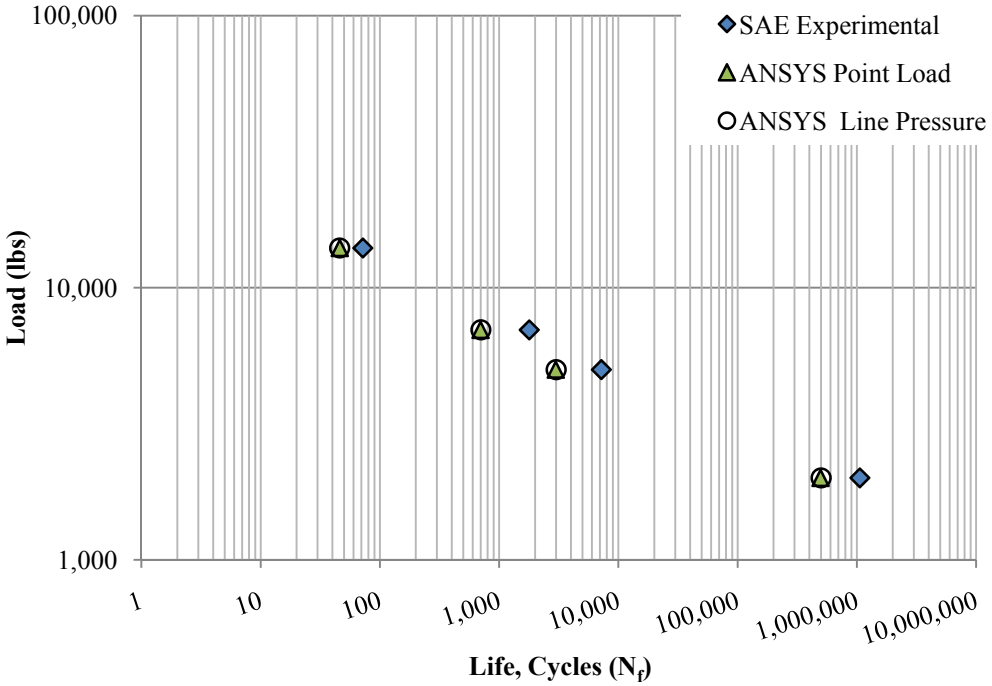

Figure 3.7 Comparison of SAE results with ANSYS WB results for different BC's – Man-Ten steel

Table 3.3 Constant Amplitude Fatigue Test Results – RQC-100 Steel

Load (lb.)		+/- 20,000	+/- 15,000	+/- 14,000	+/- 12,000	+/- 8,000	+7020 +995	+/- 4,000	+/- 3,500	+/- 3,000
Total Life Cycles	SAE Experimental (crack Initiation)	60	194	290	1300	3600	472,000	55,000(14FS)[a] 107,900(3CT)[a] 140,000(2CT)[a]	200,000	605,000
	ANSYS Point Load	36	78	94	146	521	45,387[b]	18,326	64,044	372,430
	ANSYS Line Pressure	36	78	95	147	524	45,859[b]	18,559	65,088	379,780

[a]Average value is plotted
[b]max = +7,020, min = +995 (R=0.142 w/ Morrow's mean stress correction) – not plotted in Figure 3.8

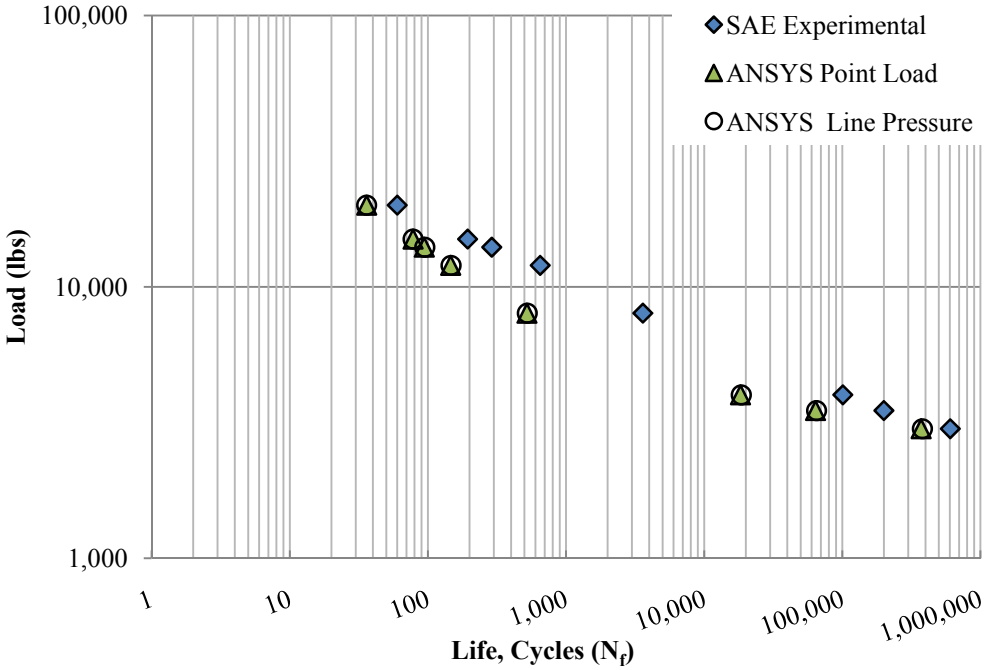

Figure 3.8 Comparison of SAE results with ANSYS results for different FE models and B.C's – RQC100 steel

3.2.3. Analysis and Discussion I

For Man-Ten and RQC-100 steels, as shown in Figure 3.7 and Figure 3.8 respectively, ANSYS WB results obtained from both BC's followed the SAE results with a similar pattern. However, for both types of steels, the ANSYS WB results underestimated the SAE results. The deviation becomes lager for applied loads between 4,000 lb. and 12,000 lb. for RAQ-100 steel and the deviation was comparatively low for Man-Ten steel. The

two loading options (point load and line pressure) did not make a considerable difference towards the life prediction in the two types of steels. However, the line pressure results gave little higher life predictions while getting closer to the SAE results. The most important observation was that $K_t$was unexpectedly high, i.e >5.5 in all loading cases which could not be accepted by any means.

3.2.4. Investigate Notch Root Stress-Strain Behavior

Since the results of ANSYS WB fatigue module did not provide acceptable and reasonable agreement with SAE experimental data, further checking and updating of FE models were carried out. The sole purpose of this investigation was to check the validity of the ANSYS WB fatigue module to be used in the life prediction of the prototype in-situ fatigue sensors. In this process, the notch root stress-strain response measured by SAE (See Figure 3.9) was compared with ANSYS WB static stress-strain results. No plasticity models or nonlinearity were included in any of the above FE models.

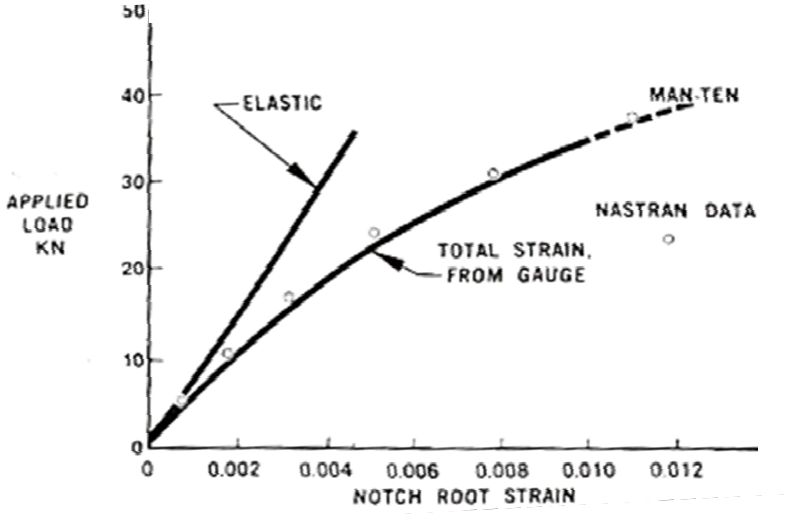

Figure 3.9 SAE Comparison of measured and calculated notch root strain for Man-Ten steel (Tucker 1975)

The following curve (see Figure 3.10) was reproduced from the above SAE curve (Figure 3.9) with imperial units for the comparison with ANSYS WB results.

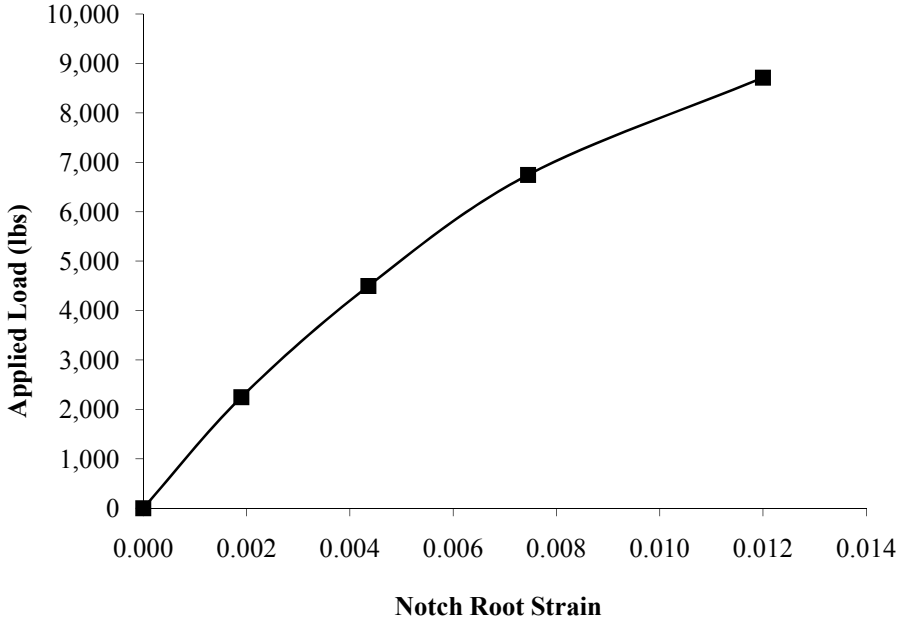

Figure 3.10 SAE (experimental) total strain values at the notch root for MAN-TEN steel (Tucker 1975), reproduced

Only Man-Ten steel properties and results were used for this comparison. Several material models were created in ANYS WB with varying plasticity models namely, Bilinear Isotropic Hardening (BISO), Multi-linear Isotropic Hardening (MISO), Bilinear Kinematic Hardening (BKIN), and Multi-linear Kinematic Hardening (MIKN). Material data were entered for each material model using the engineering data interface in ANSYS WB. The values to input for these nonlinear models were extracted from the following SAE experimental graph (Figure 3.11) (Landgraf 1975).

These different plasticity models were named as *MAN-TEN_V2* through *MAN-TEN_V6* for future references and *MAN-TEN_V1* is the linear model that was used in

previous analyses. According to Langraf (1975), the cyclic stress strain curve of a material provides the necessary relation for the cyclic plasticity analysis. Therefore, cyclic stress-strain values from Figure 3.11were used in the ANSYS WB material model, named *MAN-TEN_V6*. For other models (*MAN-TEN_V2* through *MAN-TEN_V5*), monotonic stress-strain values were used. See Table 3.4 for the values used in each material model. For all nonlinear material models (*MAN-TEN_V2* through *MAN-TEN_V6*) modulus of elasticity was taken as 30,000 ksi according to Rosenberger ((Barron 1975) and reference therein). The *MAN-TEN_V2* material model which is a MISO model requires data to be entered as plastic strain versus stress with the first point being the yield point and zero plastic strain. The *MAN-TEN_V3,* which is a BISO model, consists of a bilinear stress-strain curve with yield strength and tangent modulus. The two slopes of the curve represent the modulus of elasticity and the tangent modulus respectively. The *MAN-TEN_V4* is a BKIN model, which assumes that the total stress range is equal to twice the yield stress to include the Bauschinger effect. The *MAN-TEN_V5* consists of the MKIN model. MKIN is considered a good option to simulate metal plasticity under cyclic loading (ANSYS 2009) which is the case for this problem. *MAN-TEN_V6* is also a MKIN model with the only difference being the use of cyclic stress-strain curve instead of monotonic stress-strain curve as mentioned in the beginning.

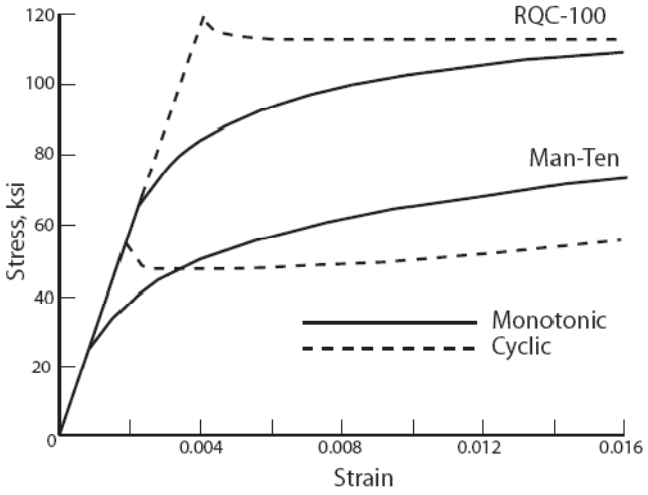

Figure 3.11 Monotonic and cyclic stress-strain curves for Man-Ten and RQC-100 steels, redrawn from Landgraf, (1975)

Table 3.4 ANSYS Material Models and Associated Values

Stress	Strain
0	0
20000	0.000676
40000	0.0013
55550	0.002
46670	0.0024
48880	0.006
51110	0.01
57770	0.016

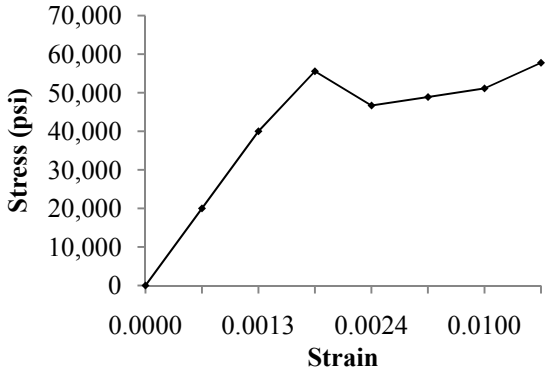

Stress	Strain
0	0
27770	0.000880
44440	0.002660
55440	0.004400
65550	0.010000
73330	0.016000

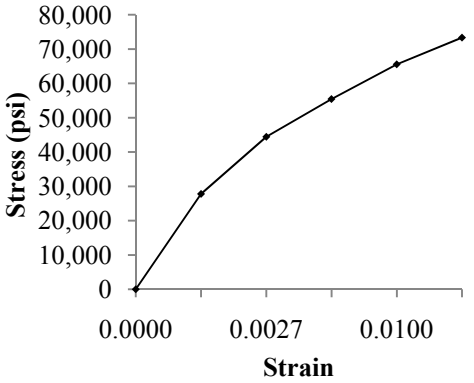

MAN-TEN_V2		*MAN-TEN_V3*		*MAN-TEN_V4*		*MAN-TEN_V5*		*MAN-TEN_V6*	
MISO		BISO		BKIN		MKIN		MKIN	
Stress	Plastic Strain	Stress	strain	Stress	strain	Stress	Plastic Strain	Stress	Plastic Strain
47000	0	0	0	0	0	47000	0	27770	0.000000
48880	0.004433	47000	0.001567	47000	0.001567	48880	0.004433	44440	0.001780
51110	0.008433	57770	0.016	94000	0.064552	51110	0.008433	55440	0.003520
57770	0.014433	E = 30,000,000 psi σ_y = 47,000 psi E_t,Tangent Modulus = 746,207		E = 30,000,000 psi σ_y = 47,000 psi E_t,Tangent Modulus = 746,207		57770	0.014433	65550	0.009120
								73330	0.015120

The ANSYS WB half model with line pressure was used in this analysis to compare and evaluate the notch root strain in the specimen for varying material models listed in Table 3.4. Sensitivity analyses were carried out using the ANSYS WB *DesignXplorer* interface for each material model in order to reproduce the SAE experimental notch root load- strain curve (Figure 3.9 and Figure 3.10).

Each sensitivity analysis was performed for 21 design points from 500 lb. to 14,000 lb. (only up to 9000 lb. are plotted for clarity and for a better comparison with the SAE curve). Sensitivity analyses for nonlinear solutions consume a lot of disk space and time. Each analysis took approximately more than 3-4 hours to complete. However, out of all nonlinear material models, *MAN-TEN_V4* and *MAN-TEN_V6* gave good sensitivity analysis results.

The following graph shows load-strain curves obtained through ANSYS WB *DesignXplorer* for different material models. Other *MAN-TEN* versions are not included for clarity. Note that, *MAN-TEN_V1* does not include nonlinearity.

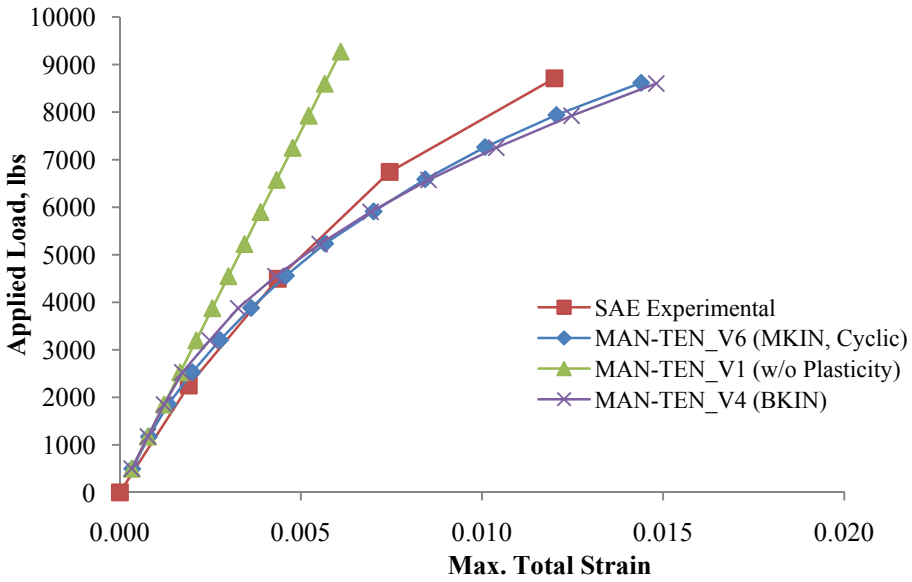

Figure 3.12 Load versus notch root total strain for different plasticity models

3.2.5. Analysis and Discussion II

From the above graph it can be seen that the *MAN-TEN_V6* consisting of the MKIN model with cyclic properties provides the closest results to the SAE experimental notch root strain response for Man-Ten steel. It was an expected result; in fact, ANSYS WB recommends kinematic models over isotropic models for cyclic loading. Having obtained acceptable strain response at the notch root, the next step was to check its performance on the fatigue life analysis. Fatigue analyses were carried out for this model for the same loading conditions (as per SAE for constant amplitude loading), and the results are shown in Table 3.5 and plotted in Figure 3.13 for comparison.

Table 3.5 Constant Amplitude Fatigue Test Results – Man-Ten steel: Comparison of Different Plasticity Models in WB with SAE Experimental Results

Load (lb.)		**+/- 14,000**	**+/- 7,000**	**+6030 +995**	**+5030 +995**	**+/- 5000**	**+/- 2000**
Total Life Reversals	SAE Experimental (crack Initiation)	72	1,750	178,000	1,131,500	7,200	>1,059,500[c]
	ANSYS Line Pressure	46	698	72,133[a]	258,000[b]	2,982	495,930
	ANSYS Line Pressure (w/ MKIN-cyclic)	**14,908**	**34,315**	**11,096,000[a]**	**25,083,000[b]**	**70,374**	**3,619,300**

[a]max = + 6030, min = + 995 (R=0.165 w/ Morrow's mean stress correction) - not plotted in Figure 3.13
[b]max = + 5030, min = + 995 (R=0.198 w/ Morrow's mean stress correction) – not plotted Figure 3.13
[c]Approximate value taken at 0.38 in. crack (should be at 0.1 in. crack – by definition)

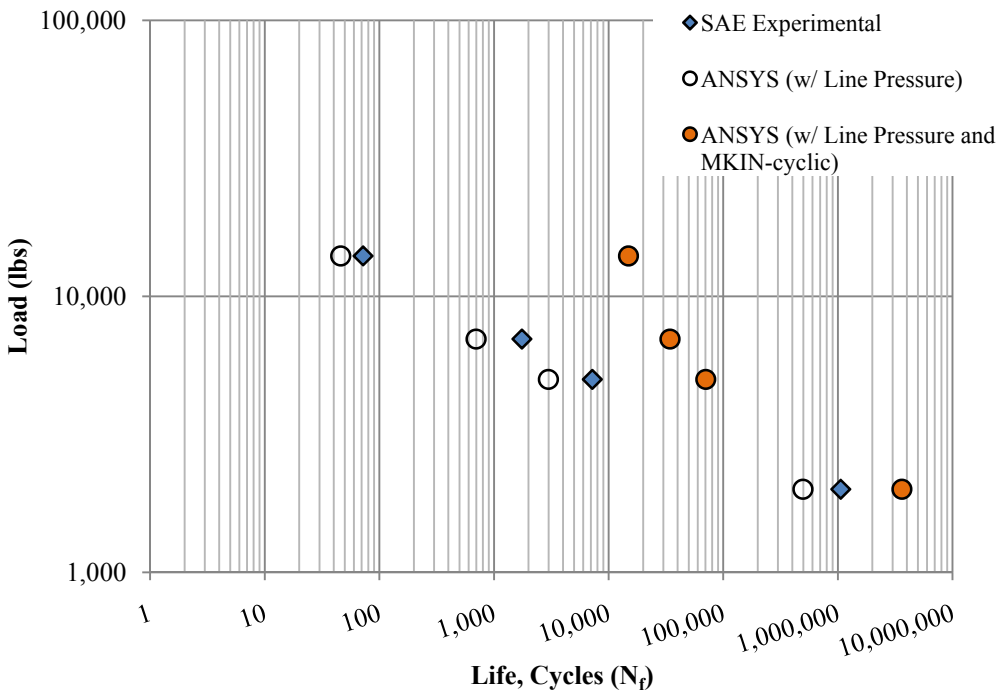

Figure 3.13 Comparison of fatigue results from ANSYS WB MKIN cyclic plasticity model and linear model with SAE experimental results for MAN-TEN steel

As shown in the above graph, by including the plasticity as MKIN model, no improvements to the fatigue results were found; instead the FE results showed a considerably higher overestimation and deviation from the expected experimental results. This issue was seen as critical higher loading cases. In fact, the ANSYS fatigue module does not have the flexibility to force the fatigue analysis to consider both elastic and plastic strains at the notch root in the strain-life analysis method.

At this phase it was decided to extract the local notch root strains from this ANSYS WB analysis and use them independently as input values to a MATLAB code, which follows the strain-life analysis method to obtain fatigue lives under the same loading conditions. Table 3.6 shows the strains obtained from ANSYS WB model with *MAN-TEN_V6* plasticity and the calculated results using strain-life equation in MATLAB. Figure 3.14 shows the same data plotted in log-log scale.

Table 3.6 Comparison of Estimated (ANSYS + MATLAB) Life with SAE Experimental Life for Man-Ten Steel Under Fully Reversed Loading

Load (lb.)	ANSYS. Equivalent Elastic Strain	ANSYS Equivalent Plastic Strain	ANSYS Total Strain	SAE Experimental Life, Cycles	MATLAB Life, Cycles (based on ANSYS total strain)
+/- 2000	0.0010785	0.00041735	0.0014959	1,059,500	741,430
+/- 5000	0.001875	0.0034739	0.0053489	7,200	4,884
+/- 7,000	0.0021251	0.0074005	0.0095256	1,750	991
+/- 14,000	0.0024854	0.07938	0.0818654	72	6

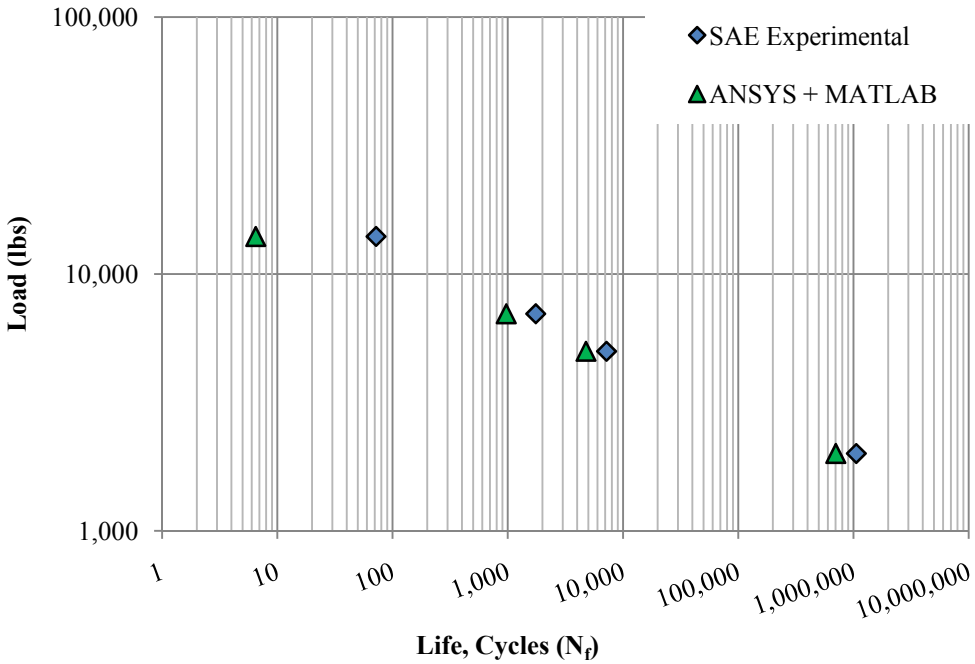

Figure 3.14 Comparison of ANSYS+MATLAB results with SAE for Man-Ten steel

Both Table 3.6 and Figure 3.14 show that the estimated life from MATLAB gives better results, compared to the results obtained from the ANSYS fatigue module for the same material model and loading conditions. Figure 3.15 shows estimated versus experimental lives: the diagonal line is the perfect correlation of the two and the two dotted lines are factor of three scatter bands. Except for the 14,000 lb. loading case (the

maximum), the other loading cases show a reasonable agreement with the experimental values.

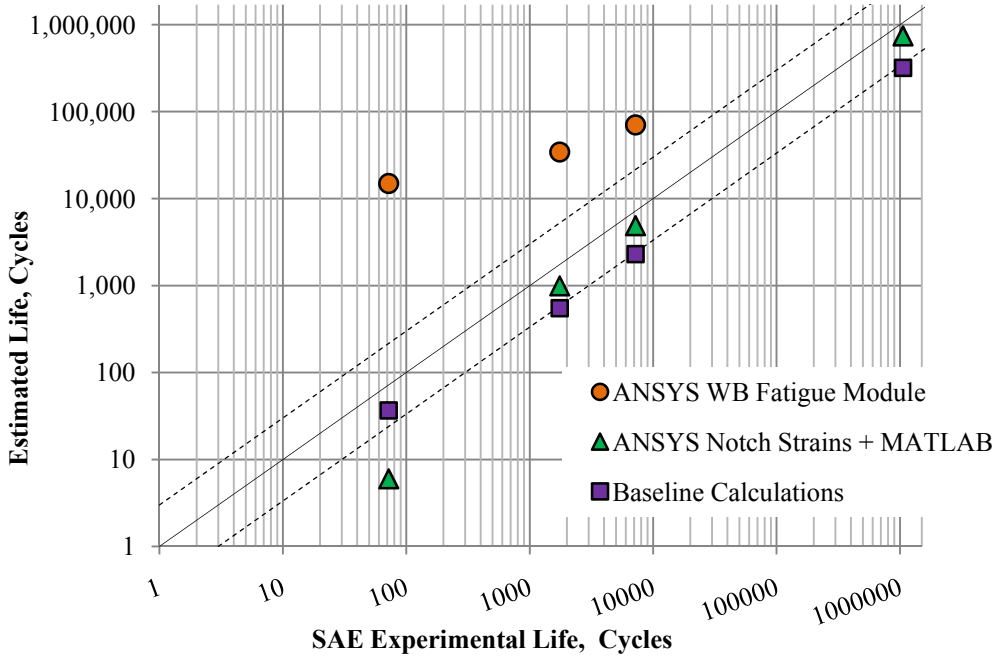

Figure 3.15 Comparison of results from ANSYS fatigue module, MATLAB calculations based on ANSYS WB notch root total strains, and baseline calculations with SAE experimental results for Man-Ten steel under fully reversed constant amplitude loading

Conclusions

From these analyses, it can be concluded that it is vital to accommodate both elastic and plastic strains for local fatigue life calculations. This fact has been further confirmed through in-depth analysis by Dowling et al. (1975) in the corresponding SAE report.

Due to the combined bending and tensile stresses, the stress distribution of the model was not uniform, thus discrepancies due to the fixed boundary condition at the bottom left vertex (see Figure 3.16, right) brought some irregularity/inaccuracy to the stress analysis, and the symmetric boundary conditions that extend towards the notch tip created similar problems especially to the plastic strain results (see Figure 3.16, left). This

was mostly evident at higher loading cases, i.e. 14,000 lb. The unexpected results at higher loads may be attributed to such issues related to the FE model. It would have been more effective if ANSYS Classics was used instead of ANSYS WB, so that the cyclic plasticity could be applied only to the elements located at close proximity to the notch root, which is more related to the actual behavior of the specimen under the specified loading.

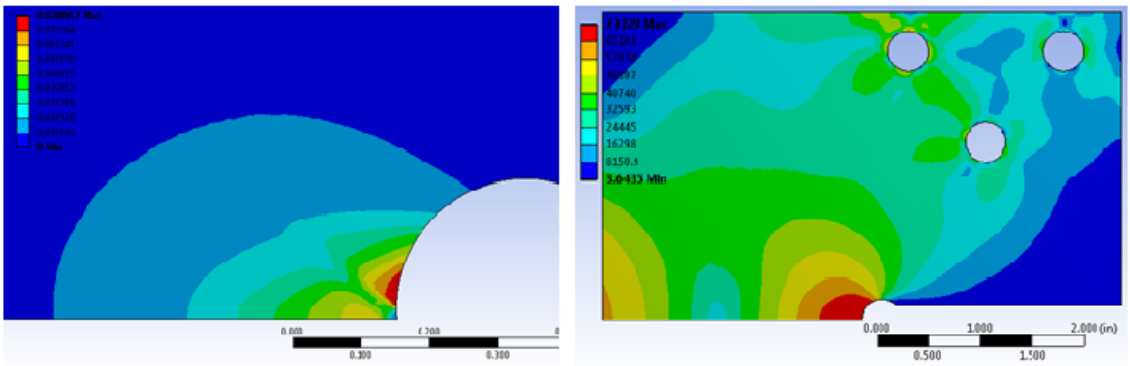

Figure 3.16 Man-Ten steel at 14,000 lb. load: equivalent plastic strain, left; equivalent stress, right

The SCF estimated from the ANSYS WB model varied from 4.3 to 2.1 from 2,000 lb. loading case to 14,000 lb. loading case, respectively while a SCF of ~3 dominated in all other loading cases. The SCF for this particular notch was determined by different methods by SAE. It was estimated 3.02 from finite element analysis (Dowling 1975), 3 from measurements of elastic notch root strain (Nelson 1975) and 2.62, 2.88 from strain gauge measurements at notch tip strains ((Newport 1990) and reference therein). Baseline calculations were also carried out to estimate the nominal stresses due to the combination of axial loading and bending across the reduced cross-section of the specimen and used as inputs to the MATLAB code to calculate life using Neuber's rule with a SCF of 3.02. These baseline results are plotted in Figure 3.15 for comparison. The nominal stresses were calculated based on the combined bending and tension effect on

the notch tip using, $S = \frac{Mz}{I} + \frac{P}{A}$ which was estimated as $0.011271\,P$ for P in [N] and S in [MPa] (Newport 1990) and as $7.25\,P$ (Landgraf 1975) for P in [kips] and S in [ksi]. The latter value $7.25\,P$ was used in the baseline estimations graphed above.

According to the overall results, the ANSYS WB fatigue module failed to deliver reliable fatigue life predictions due to its inability to incorporate total (elastic and plastic) local strains to fatigue life estimations for this particular problem. ANSYS WB static stress-strain results combined with MATLAB code delivered reliable fatigue results for the same problem.

3.3. The Fatigue Life Prediction Procedure Utilized in this Research

The fatigue life prediction procedure utilized in this research consisted of two steps. The first step involved FE modeling and analysis of the test specimen to imitate the same boundary conditions and loading of the experiment. This FE analysis was carried out as a static analysis using ANSYS WB to obtain the stress-strain response of the prototype fatigue sensor. The stresses at the notches and at their nominal locations were used to calculate the SCF for each notch.

The second step involved fatigue life calculations. Nominal stresses obtained for each sensor arm were used as inputs to a MATLAB program, which calculates fatigue life according to the strain-life fatigue analysis method with both SWT and Morrow mean stress correction theories. The equations embedded in the code are discussed under Section 2.2.1 - strain life fatigue analysis method. Two MATLAB programs were created for constant amplitude fatigue life calculations and variable amplitude fatigue life calculations. Variable amplitude fatigue life calculation program includes Rain-flow

cycle counting method as explained in Section 2.1.3. Validations of these MATLAB programs are given in APPENDIX A and APPENDIX B.

CHAPTER 4. AN OVERVIEW OF THE EXPERIEMENTAL PROCEDURE AND PROOF-OF-CONCEPT EXPERIMENTS

An introduction to the experimental procedure utilized in this research is presented in this chapter. First, an overview of the test setup, DAQ and the monitoring system are discussed. Next, the details of the proof-of-concept experiment, its results and analysis are presented. Final experiments which are discussed under Chapter 5 were designed on the basis of these proof-of-concept experiments.

4.1. Experimental Procedure: Overview

4.1.1. Test Setup

For all the experiments carried out in this research, the MTS 810 (Material Test System) hydraulic testing machine was used. The main test configuration used throughout the research was axial loading with fixed-fixed boundary conditions. Other test configurations were also explored and their limitations and issues are discussed in Chapter 6.

Axial tensile setup was identified as the most successful test configuration. The test specimens were clamped about 1.5 in. from top and bottom in the MTS to ensure a proper grip at all the time. Grip widths were changed from time to time to accommodate different specimen widths. No compression force was allowed when loading long sheet specimens in order to prevent any buckling of the specimen and the loading was never forced to zero since it was practically impossible to obtain zero load under MTS loading. Axial tensile test setup allowed obtaining higher stress levels and a uniform stress field

which helped to characterize the behavior of the prototype in-situ fatigue sensors more effectively and to verify the experimental results with baseline calculations. However, under both force controlled and displacement controlled conditions, the excitation frequency could not exceed 3 Hz due to the limitations of the MTS machine.

4.1.2. Data Acquisition System

The DAQ consisted of a National Instrument (NI) signal conditioner (SC-2345), a circuitry, a DAQ card (NI DAQ 6062E), and a laptop (Dell Inspiron 2600) with DAQ and monitoring software NI DAQ 7.1 and *LabVIEW* 8.5 installed (see Figure 4.1, Figure 4.2 and Figure 4.3).

Figure 4.1 Experimental setup in the laboratory with the DAQ

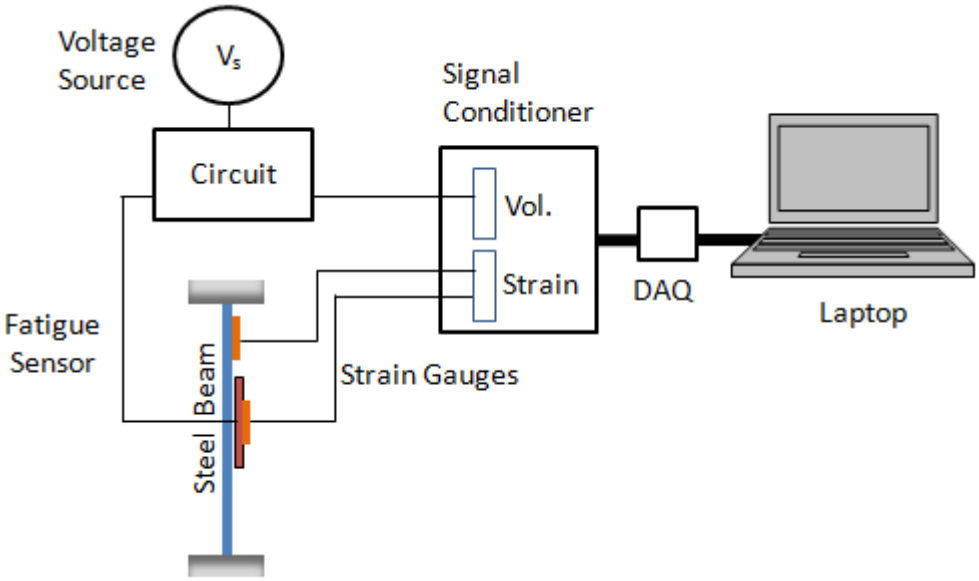

Figure 4.2 A schematic of the test setup and instrumentation for axial loading (Wijesinghe 2010)

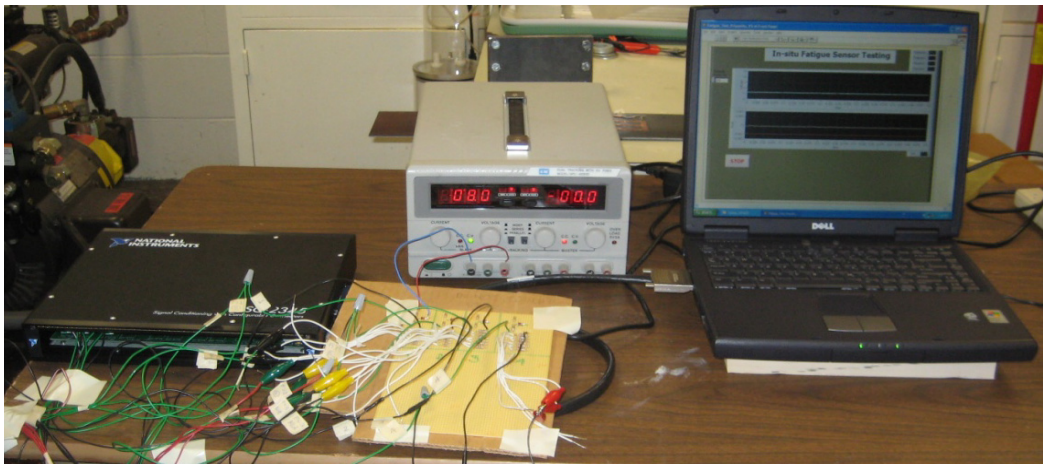

Figure 4.3 The DAQ and monitoring

SCC modules

These are portable, modular signal conditioning systems. Two types of SCC modules were used, SCC-SG01 and SCC-FT01. Each module supports two strain gauge input channels. SCC-SG01strain gauge modules with 120 Ω and quarter-bridge (Wheatstone bridge) configuration were used for strain gauge measurements. SCC-FT01 is a feed through module which connects directly to the analog input (AI) and analog output (AO)

channels of the DAQ device. These were used to acquire voltage measurements from the prototype fatigue sensors through the circuitry.

SC-2345 Carrier

The SC-2345 is a carrier/signal conditioner which transfers signals to and from the DAQ. When used with a SCC series module, it performs low-noise signal conditioning as well.

Circuitry

An external circuit was designed to measure the resistance of the notched sensor arms of the prototype fatigue sensor. Each notched sensor arm was connected to a high resistance resistor (1MΩ) in parallel so that the breaking of each arm would increase the total resistance significantly. An external voltage source was used across two resistors connected in series: one is a known resistance and the other is the varying resistance of the prototype fatigue sensor. A diode (zener diode) was used to avoid voltage drift from the voltage source and to clamp the voltage across the terminals. As an example, when the external voltage was set to 8 V, the output voltage would rise stepwise approx. from 1.29 V → 1.7 V → 2.52 V → 5 V upon breaking of each notch. The circuit facilitates 4 prototype fatigue sensors, each consisting of up to 6 sensor arms (see Figure 4.4).

R_1 = Fixed resistor (1MΩ)

R_2 = Total resistance of the prototype fatigue sensor (each sensor arm was connected to 1MΩ (R_a, R_b, R_c) resistors where, $1/R_2 = 1/R_a + 1/R_b + 1/R_c$

R_3 = Resistor (1kΩ) used to regulate the external voltage along with a Zener diode in series

V_s = Voltage source (8 V was supplied throughout the testing)

$V_2 = V_{regulated}/[(R_1/R_2) + 1]$

V_m = Voltage output measured from the prototype fatigue sensor

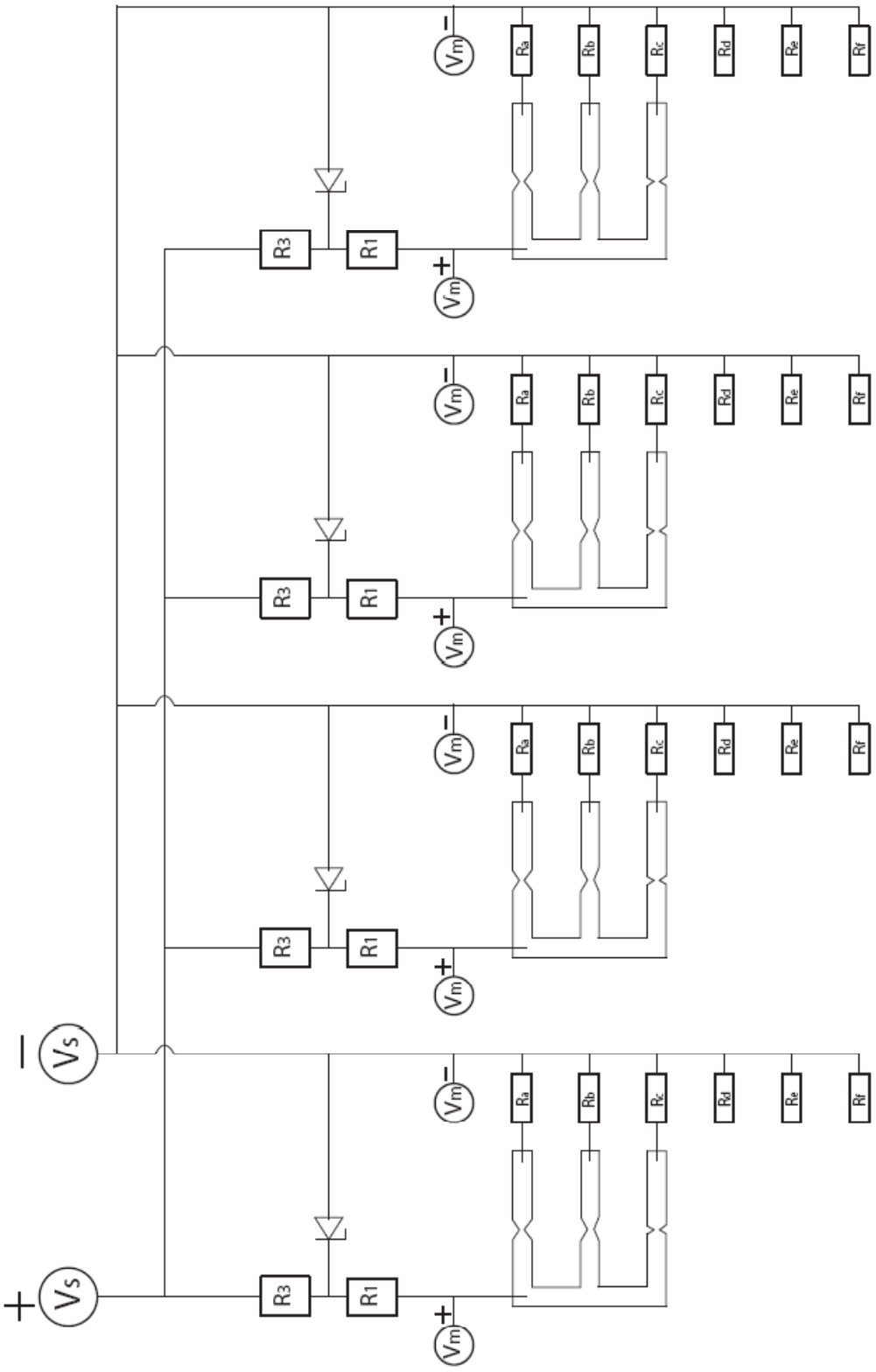

Figure 4.4 Schematic of the circuit to measure the voltage from prototype fatigue sensors

DAQ and Monitoring

Data was saved and displayed in LabVIEW V8.5 in Windows XP Professional 2002 platform. A simple program (vi file) was created for this purpose (see APPENDIX C for the format of the front panel and the block diagram). The channels were configured in the vi as DAQmx global virtual channels with continuous monitoring. Data acquisition frequency was set as a flexible parameter.

4.2. Proof-of-Concept Experiments

Proof-of-concept experiments were carried out (1) to experimentally validate the progressive failure of sensing arms that have varying SCF's and (2) to prove that such failure can be theoretically predicted within a reasonable degree of accuracy. These experiments can be considered as a benchmark in this research because the current prototype sensor design was developed along this line of thinking.

4.2.1. Specimen Design and Testing

Specimens were made from 12 in. x 3 in. x 0.063 in., 7075-T6 sheet Al sheet as shown in Figure 4.5 (right). The four sensor arms were cut using a CNC milling machine with circular notch radii varying from 0.25 in. to 1.0 in., resulting in static SCF's as given in Table 4.1.

Eight prototype sensors were tested under displacement controlled tensile cyclic loading (max = 0.02 in.; min = 0.01 in.) with fixed boundary conditions at a 1 Hz sinusoidal excitation frequency. Specimens were gripped to the MTS machine by 1.5 in. from top and bottom (see Figure 4.5, left). The results were obtained by recording the number of cycles consumed by each notched arm until it failed due to fatigue. A distinctive sound was heard upon breaking of each arm.

Figure 4.5 Test setup and specimen design utilized in the proof-of-concept experiment (Wijesinghe 2010)

Table 4.1 Proof-of-Concept Experimental Results

Notch Radius, in.	Fatigue Life, cycles							
	Test 2	Test 3[a]	Test 4[b]	Test 6[b]	Test 8[b]	Test 9[a]	Test 10	Test 11[b]
0.25	2,630	3,125	1,857	1,888	2,938	2,977	930	2,341
0.50	3,065	2,136	1,857	1,888	2,938	2,571	2,334	2,341
0.75	3,926	4,868	4,975	4,079	6,034	3,197	3,674	4,445
1.00	8,714	8,114	8,610	5,730	9,208	5,948	6,374	9,757

[a]Second smallest notch (0.5 in.) broke first
[b]Smallest (0.25 in.) and the second smallest (0.5 in.) broke at the same time

4.2.2. Finite Element Model

A finite element model of the sensor prototype was created using ANSYS WB to estimate the normal stresses in each arm at the limits of displacement-controlled cycling. Results of the static FE analysis for the two displacement levels (0.02 in. and 0.01 in.) were then used to estimate fatigue lives using the Morrow mean stress correction, the SWT mean stress model, and no mean stress correction using MATLAB.

The ANSYS WB model was created to imitate the actual test setup. Top and bottom tabs (1.75 in. x 1.5 in.) in the model (see Figure 4.6) represent the gripping areas of the prototype sensor in the MTS. The model was meshed with SOLID186 (20 node

quadratic hexahedron) and SOLID187 (10 node quadratic tetrahedron) for the solid bodies and TARGE170 (quadratic quadrilateral target) and CONTA174 (quadratic triangular contact) for contact surfaces using the WB automatic mesh generation. The mesh was refined at the notches, and at the locations where nominal stresses were retrieved, using sphere of influence body sizing (see Figure 4.6, left). Material properties of 7075-T6 Al used in the FEA and fatigue life calculations are given in Table 4.2.

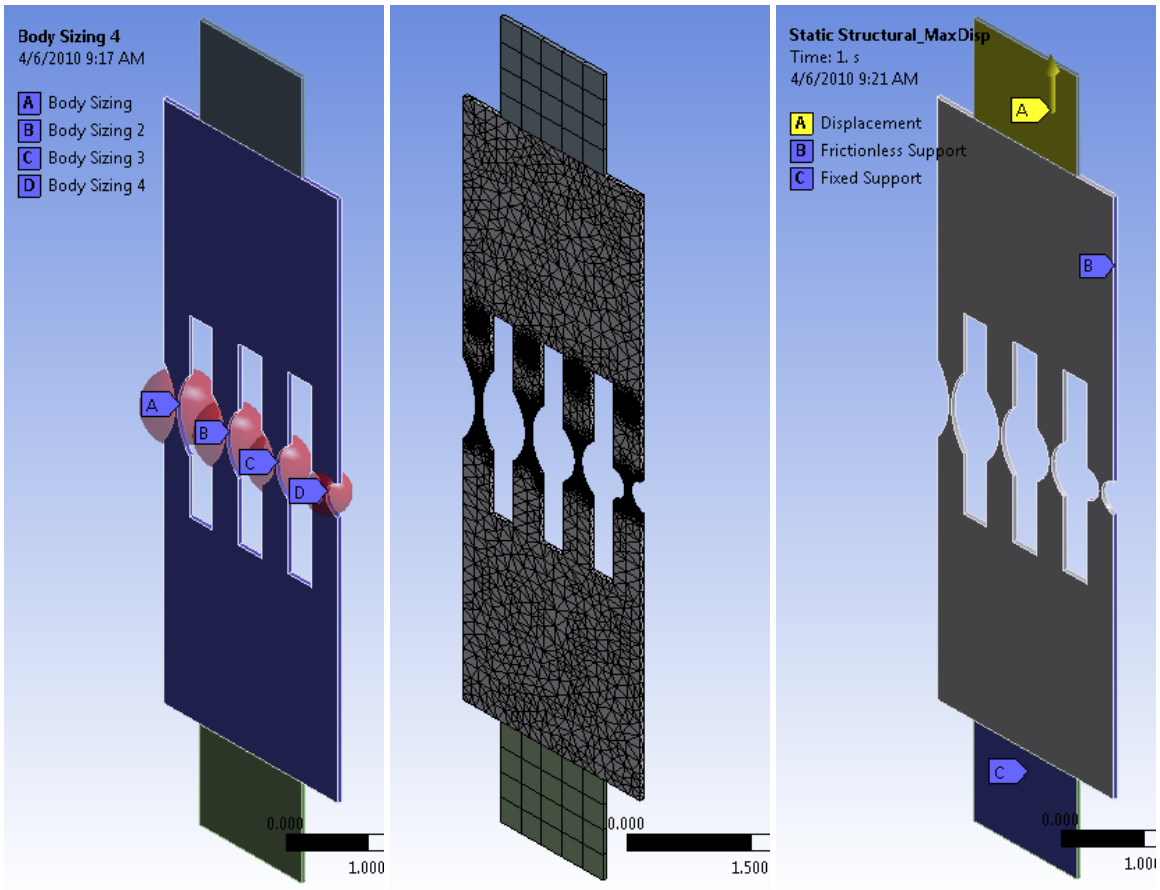

Figure 4.6 The FE model geometry and analysis settings utilized in the simulation: body sizing, left; meshed model, middle; analysis settings, right

Table 4.2 Material Properties used in the FEA (Topper 2009)

Property	7075-T6 Al
Modulus of Elasticity (E), psi	10,298,000
Poisson's Ratio	0.33
Tensile Yield Strength (S_y), psi	68,000
Tensile Ultimate Strength (S_u), psi	83,000
Fatigue Strength Coefficient (σ_f'), psi	127,100
Fatigue Strength Exponent (b)	-0.0751
Fatigue Ductility Coefficient (ε_f')	0.4664
Fatigue Ductility Exponent (c)	-0.7779
Cyclic Strength coefficient (K'), psi	136,800
Cyclic Strain Hardening Exponent (n')	0.0966

Fixed boundary conditions were applied to the front and rear faces of the bottom tab and displacement boundary conditions were applied to the front and rear faces of the top tab. Out of plane displacement was controlled by applying frictionless support boundary condition to the front and rear faces of the specimen (see Figure 4.6, right for analysis settings).

Normal stress (Y axis) results obtained for two displacement levels are listed in Table 4.3. These were obtained at nominal locations of each arm: 1.25 in. above the middle of each notch. See Figure 4.7 and Figure 4.8 for the contour plots of the normal stress (Y axis) obtained at 0.02 in. (max.) and 0.01 in. (min.) displacement levels respectively.

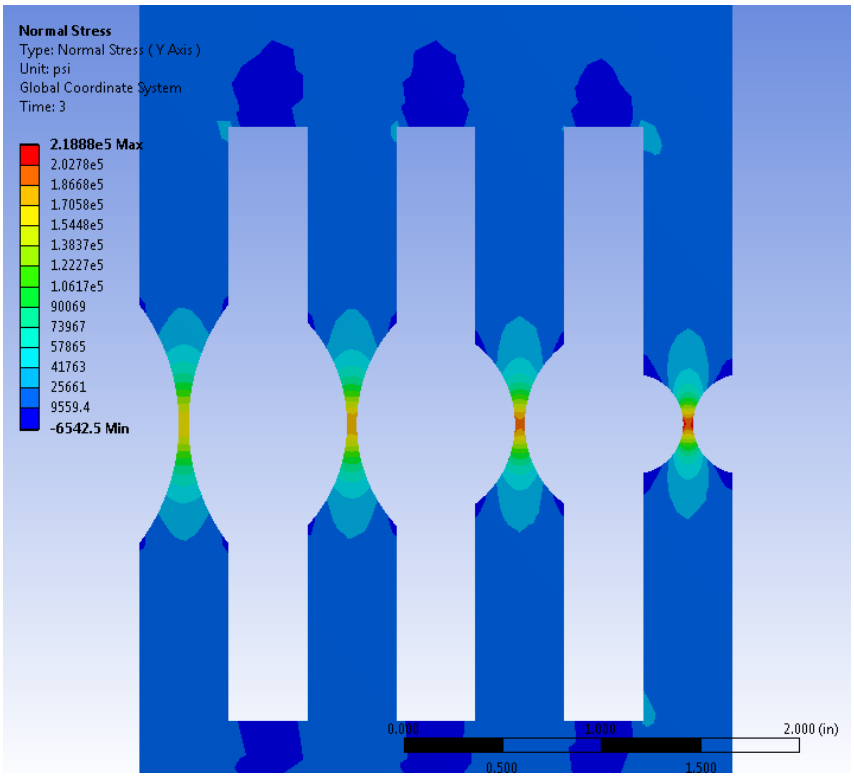

Figure 4.7 Normal stress (Y axis) results for 0.02 in. displacement

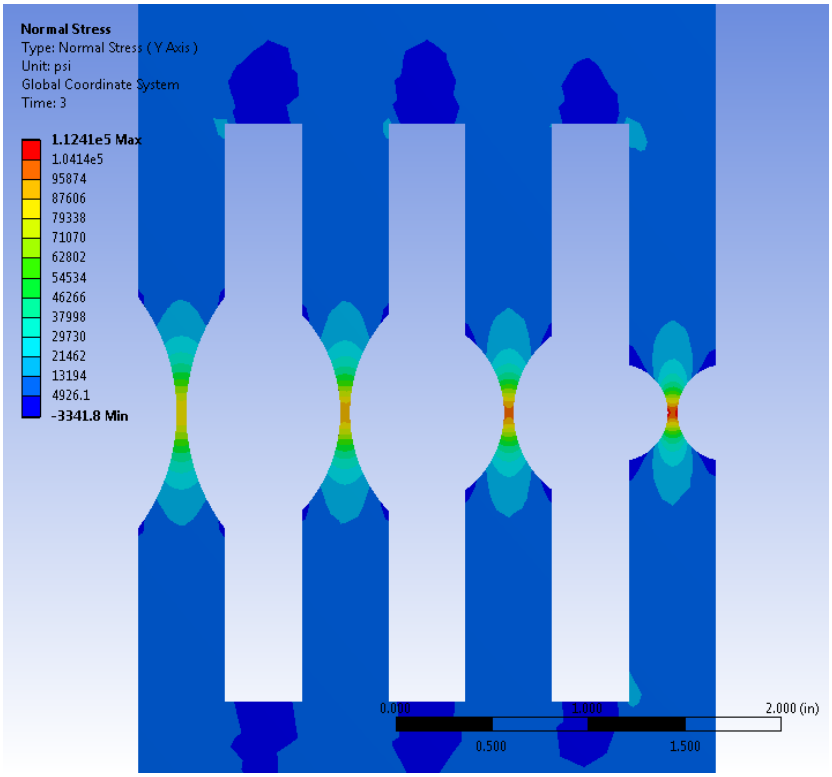

Figure 4.8 Normal stress (Y axis) results for 0.01 in. displacement

4.2.3. Results and Conclusions

Results of proof of concept experiments confirmed that by varying the SCFs at the notches, a progressive failure in notched sensor arms can be obtained. Table 4.3 summarizes the experimental (averaged) and predicted results.

Table 4.3 Results of Proof of Concept Experiments

Notch Radius, in.	**1.0**	**0.75**	**0.50**	**0.25**
Estimated SCF (Peterson 1974)	**9.135**	**9.180**	**9.270**	**9.562**
FEA normal stress for 0.02 in displacement, psi	18,634	20,421	21,723	22,937
FEA normal stress for 0.01 in displacement, psi	9,571	10,476	11,147	11,786
Average life (N = 8), cycles	**7,807**	**4,400**	**2,391**	**2,336**
Calculated life: SWT mean stress correction, cycles	**8,420**	**4,376**	**2,809**	**1,728**
Calculated life: Morrow mean stress correction, cycles	6,420	2,843	2,094	1,506
Calculated life: no mean stress correction, cycles	1,5461,00	424,770	167,040	56,676

Several conclusions were drawn from the data in Table 4.3. Most obvious is that increasing the SCF values tended to reduce the life, as expected. However, the SCF's were not sufficiently different in this prototype to clearly distinguish the lives of each sensing element, with the experimental lives showing enough scatter to overlap the data from the nearest (SCF-wise) element. Regarding the predicted lives, the SWT model was in very good agreement with the experimental values, where neglecting the effect of mean stress on the life resulted in unacceptably non-conservative life estimates.

CHAPTER 5. DEEP "U" NOTCH ALUMINUM IN-SITU PROTOTYPE FATIGUE SENSORS: EXPERIMENTS, SIMULATIONS AND RESULTS

Details of the experiments and simulations carried out for 7075-T6 deep "U" notched Al prototype in-situ fatigue sensors are presented in this chapter. These experiments, results and analyses add a benchmark towards the development of the in-situ fatigue sensors. Deep "U" notched sensors, made from 0.032 in. thick sheet Al, were tested for both constant amplitude and variable amplitude loading. Experimental details such as sensor design, fabrication, test conditions and simulation details, including FE modeling, analysis and fatigue life estimations, are further discussed.

5.1. Prototype Sensor Geometry, Fabrication and Assembly

5.1.1. Prototype Fatigue Sensor Geometry

Prototype fatigue sensor geometries were finalized after several iterations to obtain considerably large stress concentrations, i.e. 29 - 38.6 at their "U" shaped notches. The two successful geometries tested were named 2a and 1b. Geometry 2a had constant ligaments (0.03 in.) with varying notch diameters (0.03125 in. – 0.125 in.) whereas geometry 1b had constant notch diameters (0.03125 in.) with varying ligaments (0.03 in. – 0.04 in.). These prototype sensors were 2.5 in. x 4.5 in. in size: first created in Pro-E and then transferred to a CNC milling machine to cut from 0.032 in. thick 7075-T6 sheet Al. See Figure 5.1.

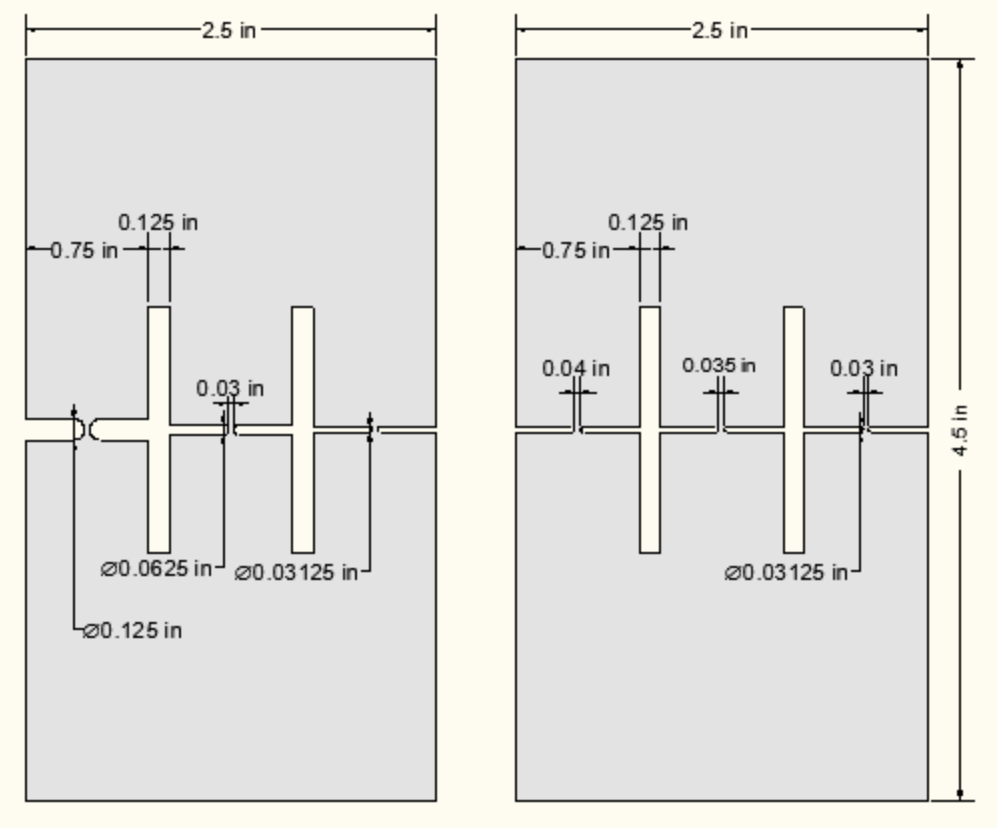

Figure 5.1 Two types of 7075-T6 Al prototype fatigue sensors: geometry 2a, left; geometry 1b, right (Wijesinghe 2010)

5.1.2. Specimen Assembly

The CNC machine cut prototype fatigue sensors were then attached to AISI 1018 steel beams (3 in. x 15 in. x 0.125 in.) as the underlying carrier material via 2.5 in. x 1 in. x 0.063 in. 7075-T6 Al spacers. The spacers were bonded to the prototype sensors at each end and to the steel beams using acrylic-based 3M DP-810 adhesive to transfer loads into the prototype sensor. First, all bonding surfaces were wiped and cleaned with acetone to remove dust and oil. Next, they were abraded with 220 grit sand paper followed by acetone cleaning to remove any loose particles on the bonding surfaces. For easy handling, the exact bonding boundaries were demarcated clearly on the steel beam prior to applying adhesive. After surface preparation, first the spacers were glued onto the

beam and then the prototype sensors were glued on top of them. Only up to five specimens could be assembled within the handling time of the adhesive. The specimens were then allowed to cure for more than 36 hours as per manufacturer's recommendations to gain the maximum strength of the adhesive. The adhesive layer also acts as an electrical insulator allowing measurement of the electrical resistance in each sensing arm when connected to the DAQ as described in Chapter 4.

5.1.3. Strain Measurements

The input-output behavior of the prototype fatigue sensors was observed using strain gages. To measure the strain on the prototype sensor and on the beam during testing, four strain gages (SG1 – SG4) were installed on a dummy sensor (without notches) as shown in Figure 5.2 and Figure 5.3. SG1 and SG2 were installed at the center of front and rear faces of the dummy sensor respectively. SG3 and SG4 were installed on front and rear faces of the steel beam respectively. This was due to some small curvature observed in the sensor raw material.

Strain gages were general purpose, linear, 120Ω, 0.25 in. long Constantan, Polyimide (PI) encapsulated strain gages manufactured by *Vishay Micro-Measurements*. According to the manufacturer's specifications, they have a fatigue life of 10^6 cycles for +/- 1500 με strain level.

The dummy specimen was tested under the same loading condition as the experiments to obtain strain measurements at each loading condition. In addition to the experimental loading conditions, it was run for 40% of the yield strength of steel. Strain measurements from the dummy sensor were used to estimate any attenuation of strain

due to the adhesive. This is an important factor to be considered in fatigue life estimations.

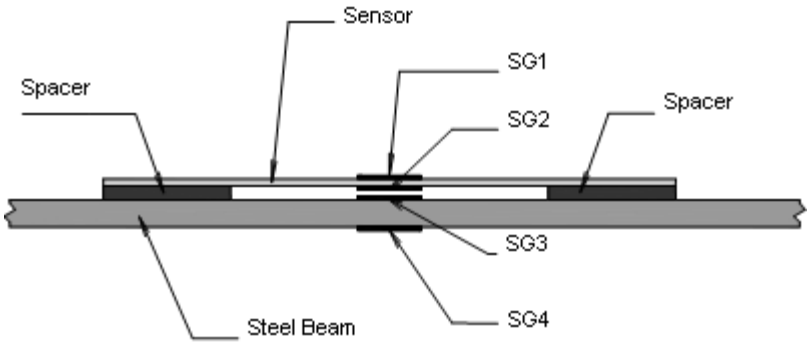

Figure 5.2 Dummy (un-notched) specimen with the sensor and spacers glued to the steel beam (Wijesinghe 2010)

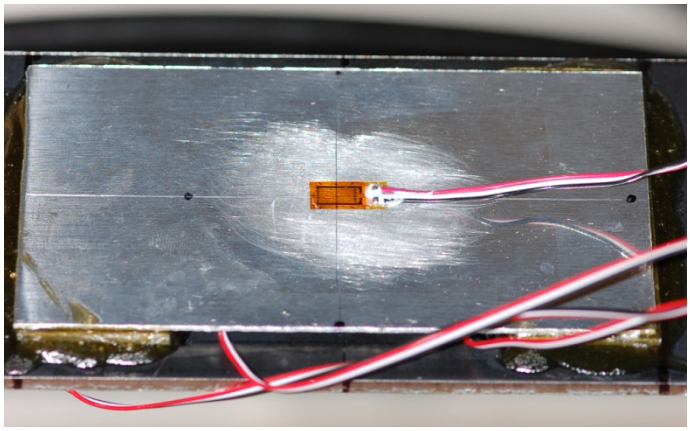

Figure 5.3 Dummy (un-notched) sensor with attached strain gages

5.2. Constant Amplitude Experiments

The majority of the prototype in-situ fatigue sensor experiments during the development stage were carried out under constant amplitude loading. Due to the dispersive nature of fatigue damage, it was crucial to obtain reliable and repeatable fatigue lives for the prototype sensors under constant amplitude loading before testing their behavior under variable amplitude loading.

5.2.1. Experimental procedure

The test was configured for tensile cyclic loading with 1 Hz excitation frequency. The steel beam was clamped 1.5 in. from top and bottom as shown in Figure 5.4. A total of 24 specimens were tested for the two prototype sensor geometries (2a and 1b) at four different loading conditions. These loading conditions were based on the percentage of the yield strength of the carrier specimen (32 ksi). In this way the results can be directly related to any size of a steel carrier. Experiments were run under four loading conditions; from 50% of yield strength of steel to 80%, of the yield strength of steel and each test was repeated three times. These load values were chosen to provide sensor failure data in relatively short periods, so as to provide data for the validation of the fatigue model. The 50% experiments were run at 3 Hz to accommodate the additional cycles needed to reach failure and were connected to the DAQ as shown in Figure 5.4 (right). All loads were applied as constant amplitude sinusoidal waves with a stress ratio, R=0.05. Except for the 50% loading tests, no data acquisition was needed since the breaking of each notch was heard with a distinct sound and could be seen by a lenscope magnifier.

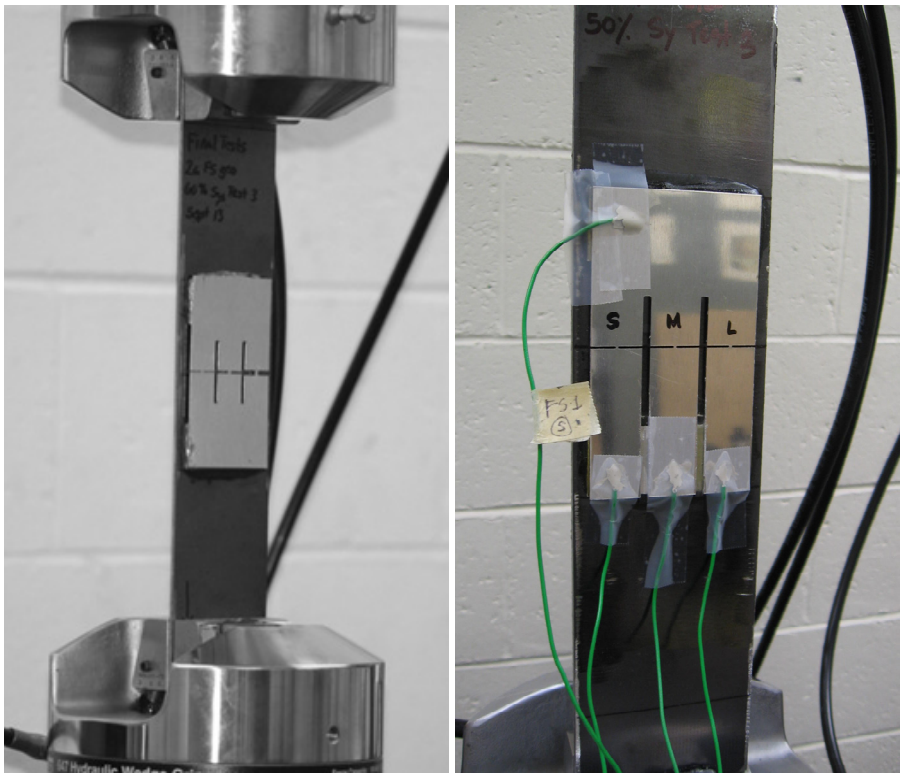

Figure 5.4 Constant amplitude fatigue experiments with deep "U" notch Al prototype: test setup, left (Wijesinghe 2010); sensor arms connected to the DAQ, right

5.2.2. FE modeling and Simulation

The goal was to create FE models of the test specimen with two types of prototype fatigue sensor geometries and apply boundary conditions similar to the experimental conditions (a) to obtain SCF's through static stress analyses for each notch by taking the maximum stress at the notch root and nominal stress at the corresponding arm and (b) to use above SCF's and nominal stresses to estimate fatigue lives of these prototype fatigue sensors (using MATLAB) - for each notch geometry and for all loading scenarios.

In the process of FE modeling of the specimens, it was assumed a perfect bond between the bonded surfaces, i.e. no attenuation of stress would occur due to the adhesive. This assumption was made for several reasons. It was difficult to characterize the adhesive layer in the FE model due to the unavailability of the required material

properties. Another reason was the difficulty in controlling a uniform thickness of the adhesive layer during assembly. DP810 was a viscous adhesive in which the viscosity lies between 18,000 – 22,000 cps at 75°F (3M 2004) thus making it extremely difficult to control the applied pressure and to ensure an even adhesive layer by manual handling.

Geometry creation and meshing

Two FE models were created in ANSYS WB, imitating the prototype fatigue sensor geometries used in the laboratory experiments. Solid models of the specimens were first created in Pro-E and then imported to ANSYS WB in .igs format for meshing. The carrier steel beam volume was divided 1.5 in. from top and bottom to represent the gripping areas in the MTS in order to apply boundary conditions to the FE model. Specimen geometry with 2a prototype fatigue sensor attached is shown in Figure 5.5.

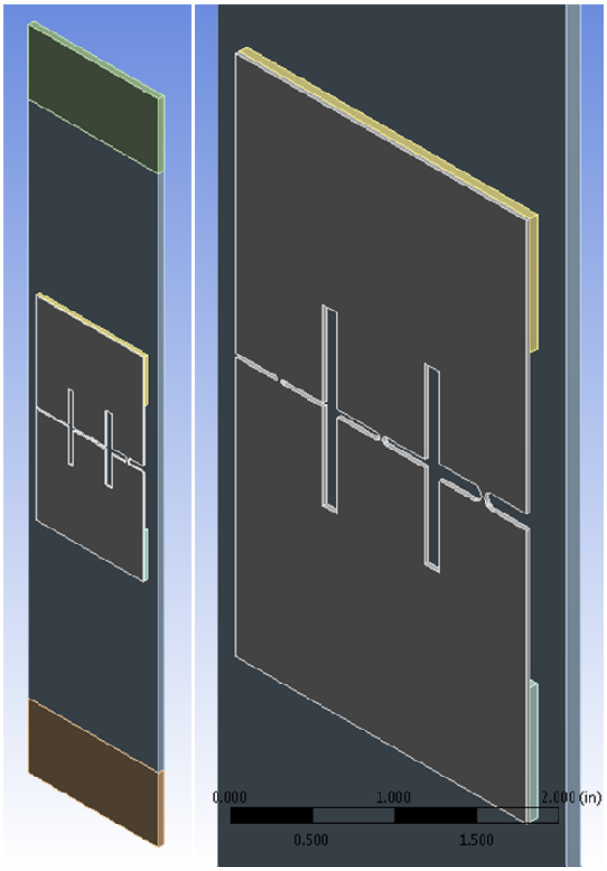

Figure 5.5 ANSYS WB model for 2a specimen geometry

Several mesh control options were added to the WB automatic meshing option to obtain the desired refinement at the notches. Body sizing with a sphere of influence with 0.8 in. radius and 0.005 in. element size were defined for each notch. In addition, the element size was refined to 0.01 in. at the stress probe locations using the same body sizing method. This was done in order to obtain a higher accuracy from the stress analysis at the locations where nominal and local stresses were retrieved for fatigue life calculations. See Figure 5.6 for the meshed specimen model with the 1b prototype sensor attached and to the right is a zoomed view of the refined mesh of its 0.04 in. notch.

The meshed model consisted of approximately 98,000 elements with 160,000 nodes. The solid bodies of the model were meshed with SOLID186 and SOLID187 with hexahedral and tetrahedral elements while the contact surfaces were meshed with TARGE170 and CONTA174 quadrilateral target and quadrilateral contact elements.

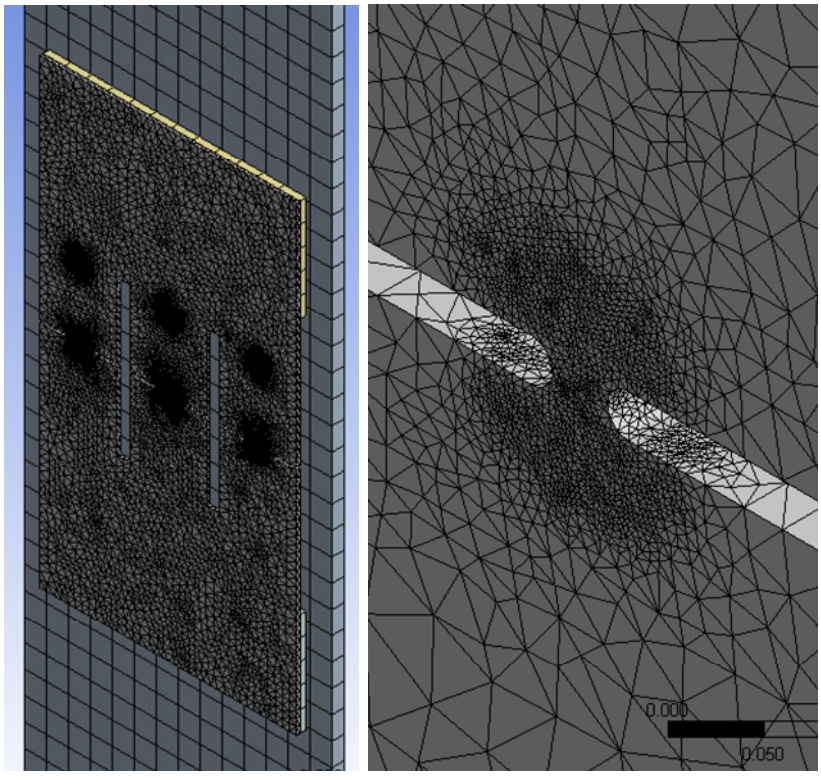

Figure 5.6 Meshed model of the specimen with 1b prototype fatigue sensor

Material properties of 7075-T6 Al used in the FEA and fatigue life calculations are given in Table 4.2 in Chapter 4. Material properties of A1018 steel used in the FE analysis are given in Table 5.1.

Table 5.1 Material Properties of ASTM A1018 Steel Used in the FEA (ASM International Handbook Committee. 1996)

Property	A1018 Steel
Modulus of Elasticity (E), psi	29,700,000
Poisson's Ratio	0.29
Tensile Yield Strength (S_y), psi	32,000 (SAE International. 2010)
Tensile Ultimate Strength (S_u), psi	58,000 (SAE International. 2010)
Fatigue Strength Coefficient (σ_f'), psi	113,400
Fatigue Strength Exponent (b)	-0.11
Fatigue Ductility Coefficient (ε_f')	0.19
Fatigue Ductility Exponent (c)	-0.41
Cyclic Strength coefficient (K'), psi	186,200
Cyclic Strain Hardening Exponent (n')	0.27

Boundary Conditions and the Analysis Procedure

Boundary conditions were applied to the two types of meshed FE models (with 2a and 1b prototype fatigue sensors attached) to imitate the same loading conditions in constant amplitude experiments, which was discussed under Section 5.2.1. Fixed boundary conditions were applied to front and rear faces of the bottom tab and force was applied to front and rear faces of the top tab as shown in Figure 5.7. Maximum and minimum forces corresponding to 80% - 40% of yield strength of the carrier steel beam (32 ksi) with a stress ratio of R=0.05 are given in Table 5.2.

A total of 20 FE static stress analyses was carried out for both geometries in order to obtain local and nominal stresses corresponding to each notch.

Table 5.2 Loads Applied to the FE Model for Static Stress Analysis

	Max. load, lb.	Min. load, lb.
80% Sy	9600	480
70% Sy	8400	420
60% Sy	7200	360
50% Sy	6000	300
40% Sy	4800	240

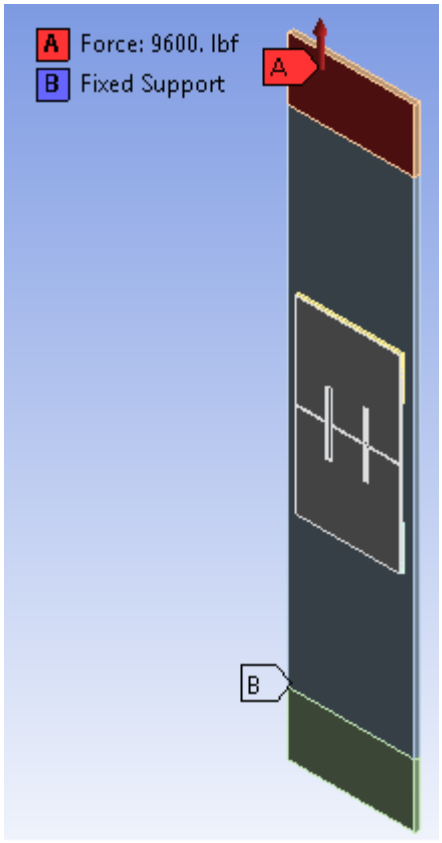

Figure 5.7 Analysis settings for static stress analysis

Results of the FEA

Normal stress results for the 2a prototype at its notches are shown in Figure 5.8 at 80% of the yield stress of the carrier. Shown in Figure 5.9, is the normal elastic strain obtained for 1b geometry at the same loading. Most interestingly, the static stress results showed some bending in the specimen as shown in Figure 5.10 which was not observed during laboratory testing.

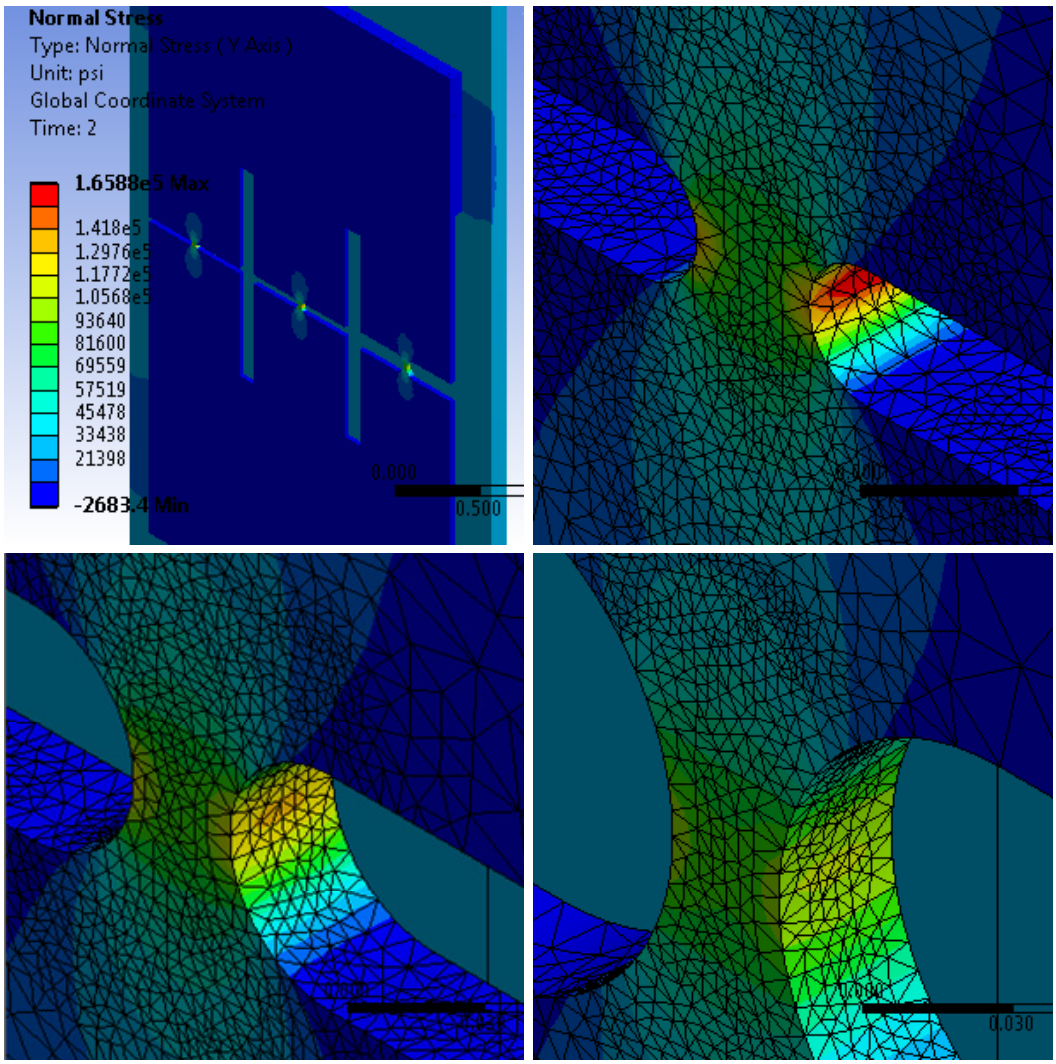

Figure 5.8 Normal stress (Y axis) results: 2a prototype, top left; Ø0.03125 in. notch, top right; Ø0.0625 in. notch, bottom left; Ø0.125 in. notch, bottom right

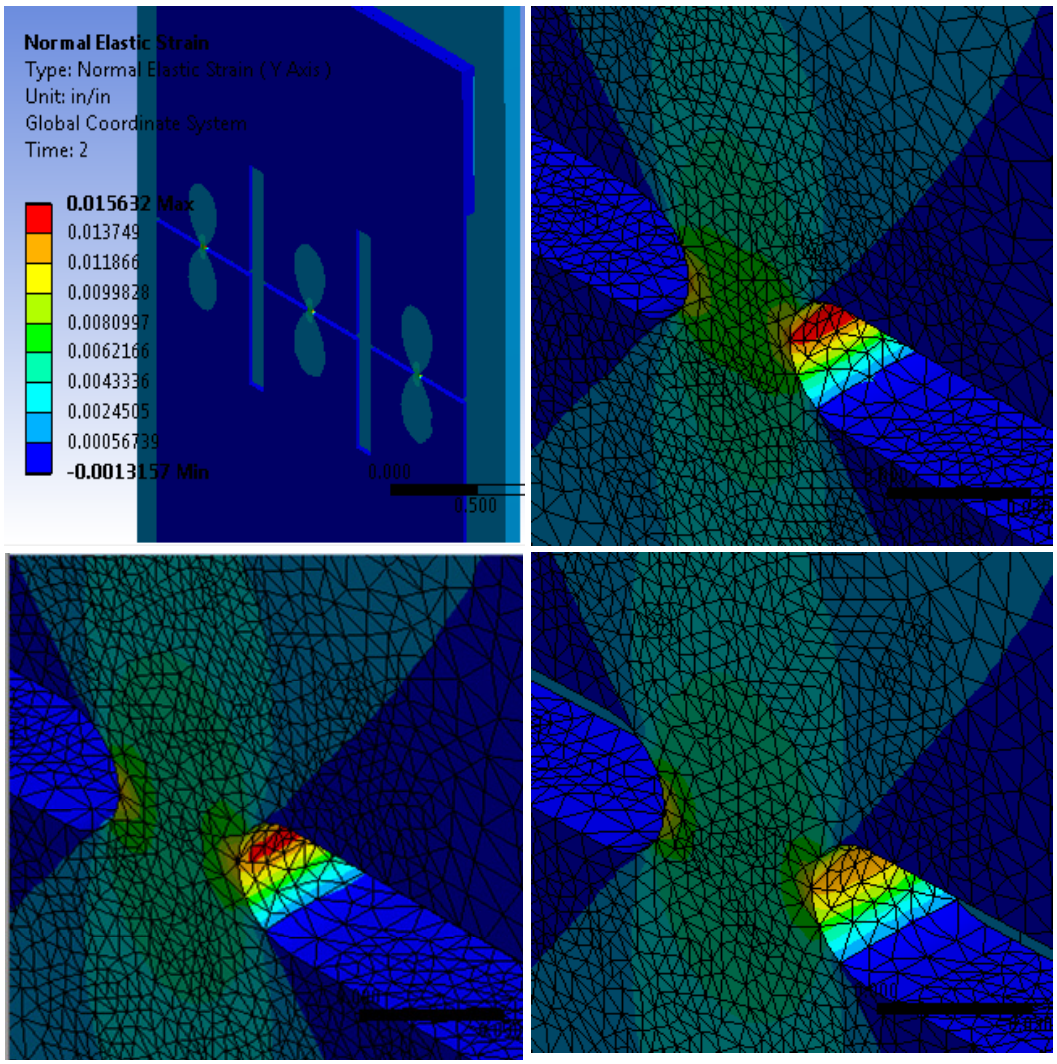

Figure 5.9 Normal elastic strain (Y axis) results: 1b prototype, top left; 0.03 in. notch, top right; 0.035 in. notch, bottom left; 0.04 in. notch, bottom right

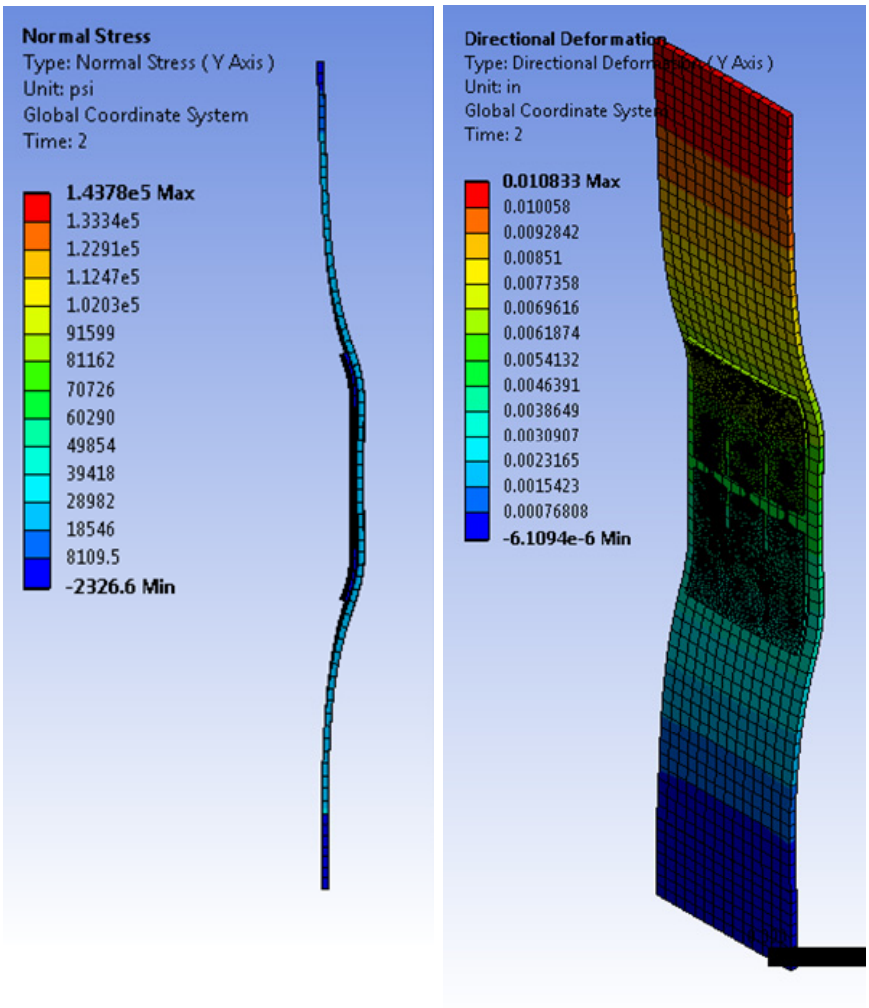

Figure 5.10 Normal stress results (Y axis) for 2a specimen showing the deflected shape (2× auto scale), left; directional deformation (Y axis) (2× auto scale), right

Stress concentrations at the notches showed the highest stress at the middle of each notch root as expected (Figure 5.11, left). The elastic SCF's were calculated based on this maximum stress and the nominal stress which was obtained at 0.69 in. above the horizontal centerline of the notch root. See Figure 5.11 bottom, for stress probe locations.

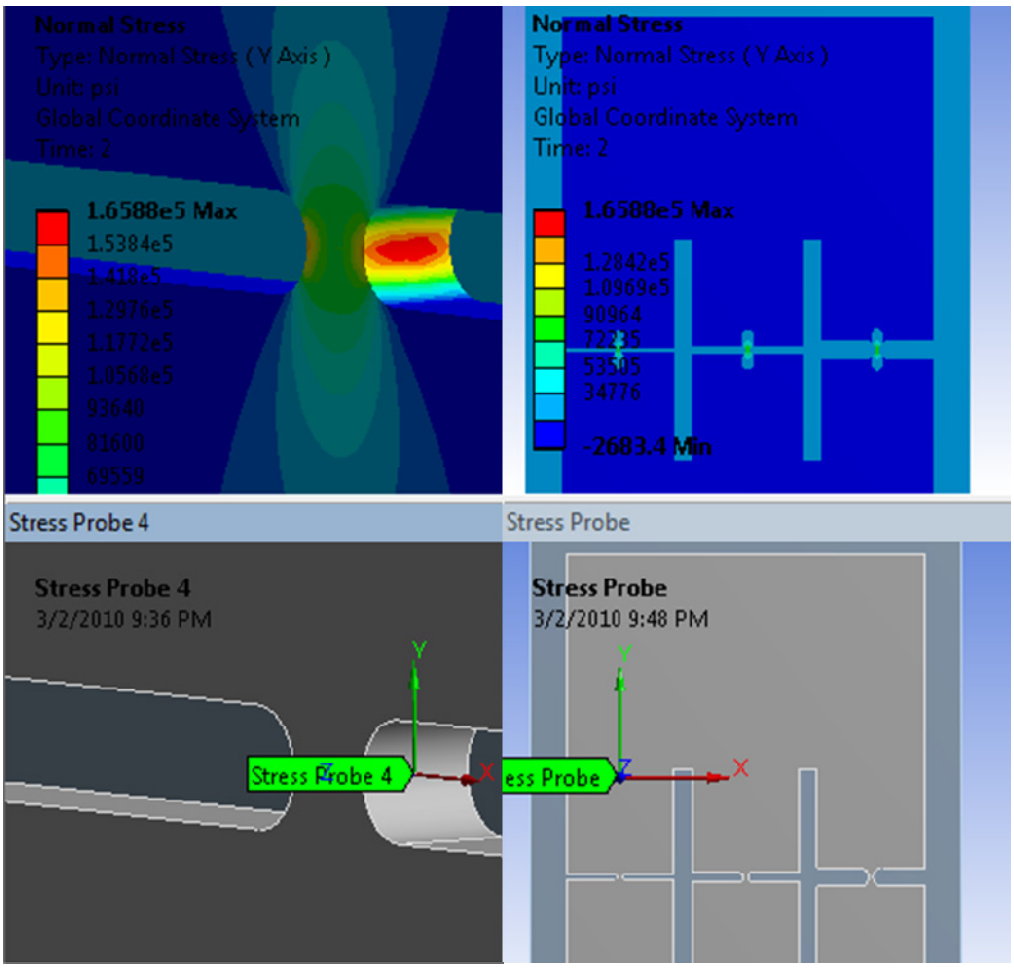

Figure 5.11 Locations of stress probes in the FE model to obtain local stress, left; nominal stress, right

The SCF's along with the nominal stresses were used as inputs to the MATLAB code to calculate fatigue lives. MATLAB code calculates fatigue lives with mean stress correction according to the SWT and Morrow's mean stress correction methods. The same procedure was repeated to calculate the lives with a stress attenuation of approximately 25% due to the adhesive. This percentage of attenuation was obtained from strain data using the dummy specimen (Zacharie 2009) as explained in Section 5.1.3. The same dummy specimen after a longer period of setting time (approximately 3 months) gave less than 2% attenuation. This may be contributed to the stiffening of the

adhesive over time, which was able to transfer more stress from the carrier beam to the prototype sensor. This fact is being mentioned, and due to the uncertainty of the percentage of attenuation that might have occurred during different resting periods for each specimen, 25% attenuation was set as the upper limit for analyzing the results.

A comparison of SCF's obtained from Peterson's (Pilkey 1997) and FE analysis is given in Table 5.3. FE analysis results showed a slight variation (less than 1% increase) in the static SCF's with the decreased maximum loading levels. These values were averaged in Table 5.3.

Table 5.3 SCF's Obtained from FE Method and Peterson's (Pilkey 1997)

	Geometry 2a			Geometry 1b		
Notch Geometry	0.125 in. diameter	0.0625 in. diameter	0.03125 in. diameter	0.04 in. ligament	0.035 in. ligament	0.03 in. ligament
FEA	27.57	32.16	38.55	31.68	35.86	38.61
Peterson's	29.04	32.62	38.60	31.36	34.48	38.60

5.2.3. Results and Analysis

Experimental results for both geometries are plotted with simulated results; Figure 5.12a, Figure 5.12b and Figure 5.12c for prototype sensor geometry 2a and Figure 5.13a, Figure 5.13b and Figure 5.13c for prototype sensor geometry 1b. See Table 3 and Table 4 in APPENDIX D for corresponding values. Both SWT and Morrow mean stress correction curves are plotted for each notch to compare with the experimental results. Fatigue lives with a 25% stress reduction due to adhesive are also plotted for each notch (only the SWT mean stress correction curve is plotted for clarity).

Overall, the results for geometry 1b showed a good agreement with the estimated results compared to geometry 2a. Out of the three notches in 2a, the 0.125 in. diameter notch (largest) showed lower experimental fatigue lives compared to the estimated values

especially at low stress ratios tested. A similar behavior pattern was noticed in 0.0625 in. diameter notch geometry but with higher experimental lives at higher stresses (see Figure 5.12b). Out of the three notches in 2a, the experimental results of the smallest notch geometry (0.03125 in. diameter) agreed well with the estimated results (Figure 5.12c). However, unlike the other two notches, experimental values for this smallest notch were higher than estimated, but fall between 0% and 25% attenuation curves.

In prototype sensor geometry 1b, experimental results agreed well with the simulated results (see Figure 5.13a, Figure 5.13b and Figure 5.13c). It was observed that at higher stresses, the experimental values were closer to the 25% attenuation curve than at lower stresses. This was also observed by the strain response of the dummy sensor, in which approximately 25% attenuation of stress was noticed at 80% yield of the carrier (Zacharie 2009). The same phenomenon was noticed in 2a geometry as well. In addition, the smallest notch behavior (see Figure 5.13c) is almost the same as the smallest notch behavior of geometry 2a (Figure 5.12c). Since the geometry of both notches is the same, this demonstrates a good repeatability of the fatigue results obtained.

From this analysis it was also observed that the life estimations obtained from SWT and Morrow were in good agreement with each other. This was clearly seen at stress ranges between 70% - 50% of yield strength and most obviously for smaller notches than the larger ones (see Figure 5.12a).

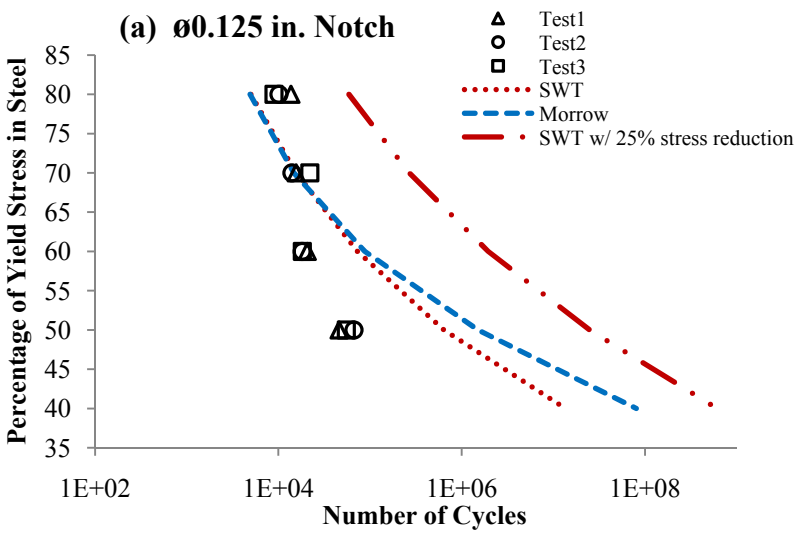

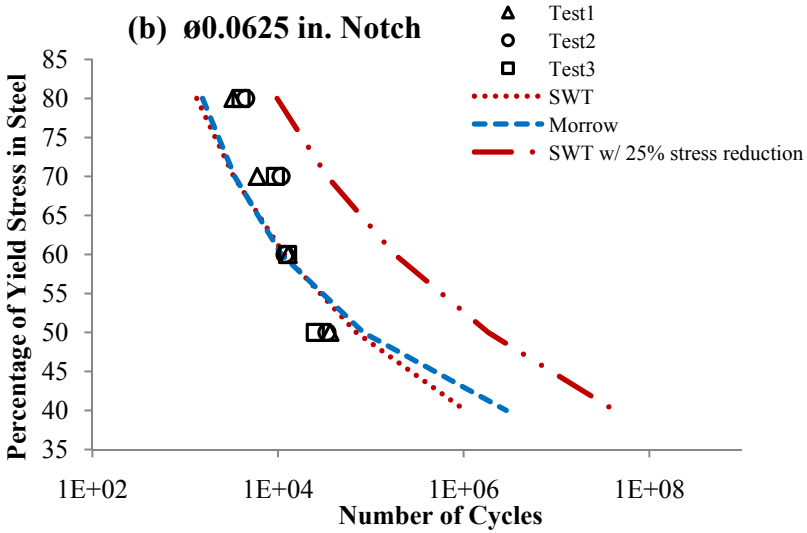

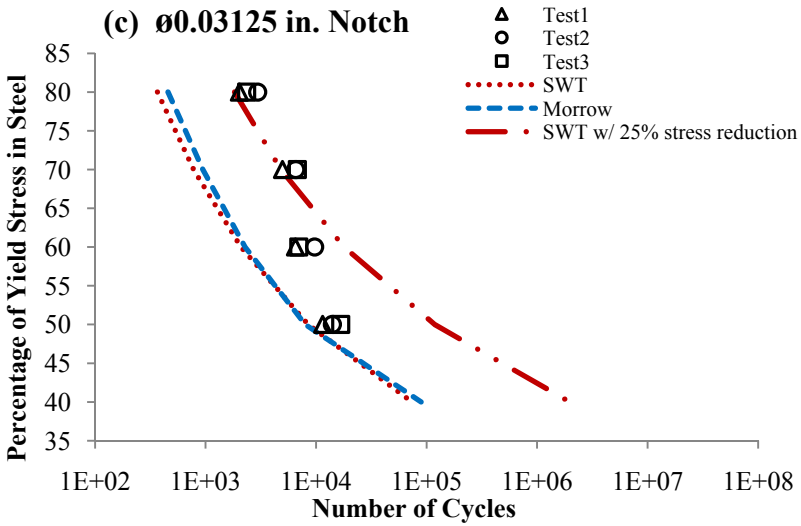

Figure 5.12 Experimental and estimated results for 2a prototype fatigue sensor

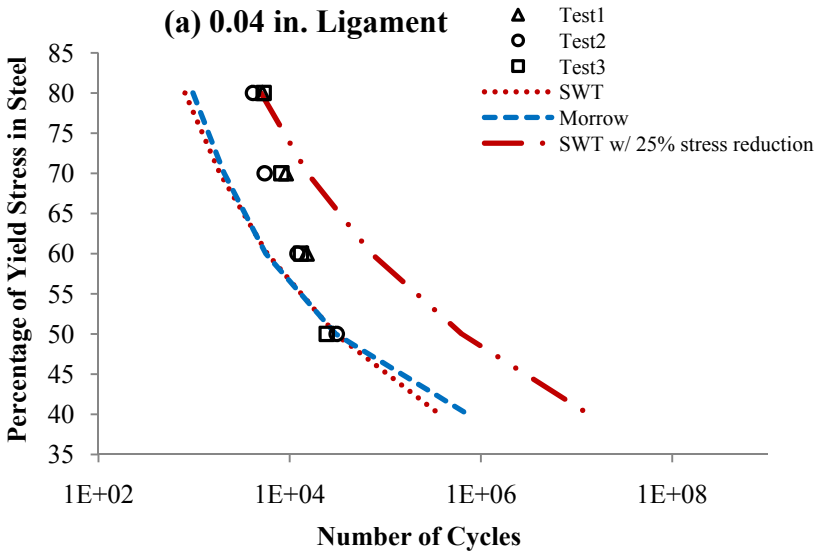

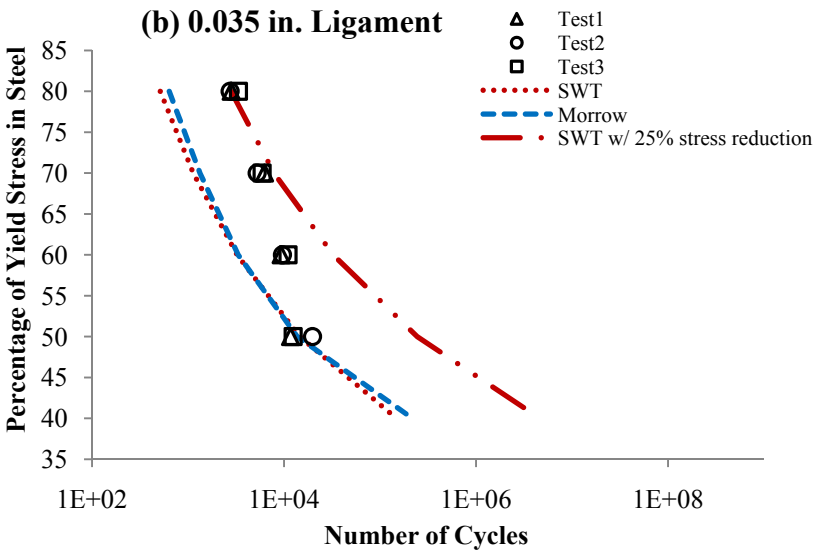

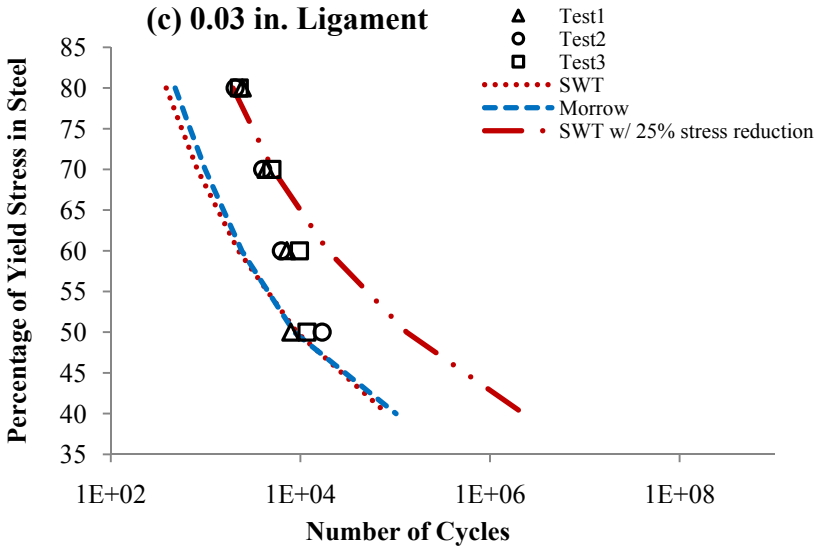

Figure 5.13 Experimental and estimated results for 1b prototype fatigue sensor

5.3. Variable Amplitude Experiments I – Two Load Ranges

Experiments and simulations carried out and analyzed so far were focused on constant amplitude loading conditions only. However, in practical standpoint, typical loading in a bridge is more related to variable amplitude loading rather than constant amplitude loading. Therefore, as an initial attempt to check the validity and behavior of the prototype fatigue sensors under variable amplitude loading a simple two level loading scenario was selected.

5.3.1. Experimental procedure

The combination of loading levels were selected from 40% - 80% of yield strength of steel following the constant amplitude experimental conditions. For simplicity, only two load ranges (high and low) with ten cycles from each were used at a time. Therefore, one block corresponds to 20 cycles. The maximum load range was then changed while keeping the minimum load range the same. Each two-level loading was programmed in the MTS by multipurpose test ware (MPT) which allows creating inputs with multiple load ranges. Specimen fabrication, assembly and the experimental setup was the same as the constant amplitude experiments. However, only 1b prototype sensor geometry was used for variable amplitude experiments. This is because geometry 1b showed a good agreement between experimental and estimated fatigue lives under constant amplitude loading when compared to the geometry 2a. The excitation frequency was 1 Hz throughout the loading and the total number of blocks to failure was manually recorded from the MTS reading.

Load Combinations

The following load combinations were selected for variable amplitude experiments. The percentage denotes the percentage of yield strength (Sy) of steel.

Load History 1: 80% Sy + 40% Sy

Load History 2: 70% Sy + 40% Sy

Load History 3: 60% Sy + 40% Sy

Load History 4: 50% Sy + 40% Sy

Even though initially it was planned to carry out experiments under all four load combinations, the total time and the number of blocks to failure during first two load combinations turned out unexpectedly higher than estimated (see Results and Analysis Section). Based on these results, it was not feasible to carry out experiments for the last two load combinations. This was because the excitation frequency had to be limited to 1Hz in the MTS to achieve the conformity between the input and measured response and under such frequency load history 3 would consume more than 260 hours and load history 4 would take more than 2800 hours. Therefore, ten experiments in total were carried out for the first two load histories and only six experiments provided good results which are discussed under Result and Analysis Section.

5.3.2. FE Modeling and Simulation

Finite element analyses and life estimations were carried out using ANSYS and MATLAB respectively to estimate life of the 1b prototype sensor under the above combined load histories. SCF's and nominal stresses used for constant amplitude estimations (See Table A-1 and Table A-2 in APPENDX D) were also valid for variable amplitude estimations because the same ratios of yield stress of steel were used with the

same geometry and experimental conditions. Only the fatigue life estimation (using MATLAB) was different since it included Miner's damage summation rule to calculate the total blocks to failure for each combined load history. Similar to constant amplitude estimations, 25% stress reduction was carried out with Miner's damage summation method for each combined load history to account for attenuation of stress due to the behavior of the adhesive.

5.3.3. Results and Analysis

Fatigue life results plotted based on maximum nominal stress range versus fatigue life in blocks for 1b prototype sensor geometry are shown in Figure 5.14a, Figure 5.14b and Figure 5.14c for 0.04 in., 0.035 in., and 0.03 in. notches respectively. Only the SWT mean stress correction curve is plotted for clarity. In addition, fatigue lives with no mean correction are also plotted with and without stress attenuation. Due to the limitations discussed earlier, experiment results were obtained for the first two load combinations only (80% + 40% and 70% + 40%).

Unlike constant amplitude results, experimental results of the two load combinations showed a considerable deviation from the estimated values calculated with SWT mean stress correction. This was evident in all three notches. However, the experimental results for all three notches seemed to follow the no-mean stress curve for the two load combinations tested. In addition, they were closer to the SWT with 25% stress reduction curve, than SWT with no reduction curve.

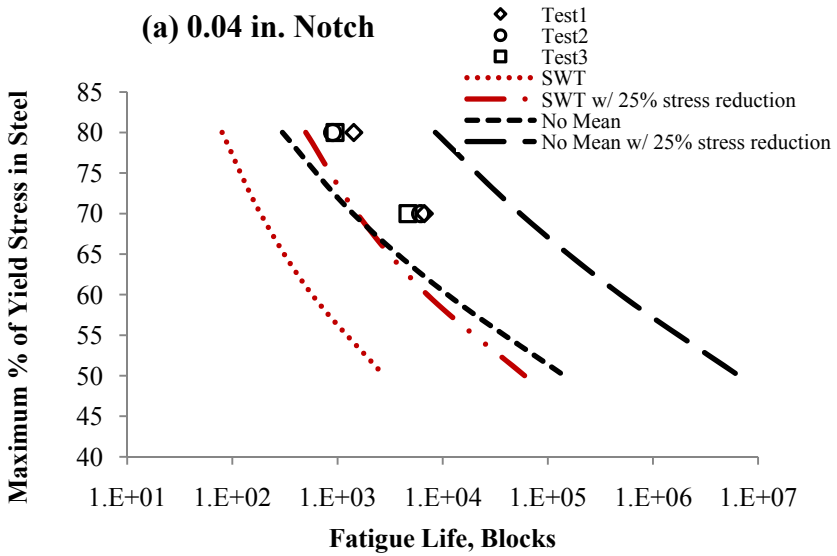

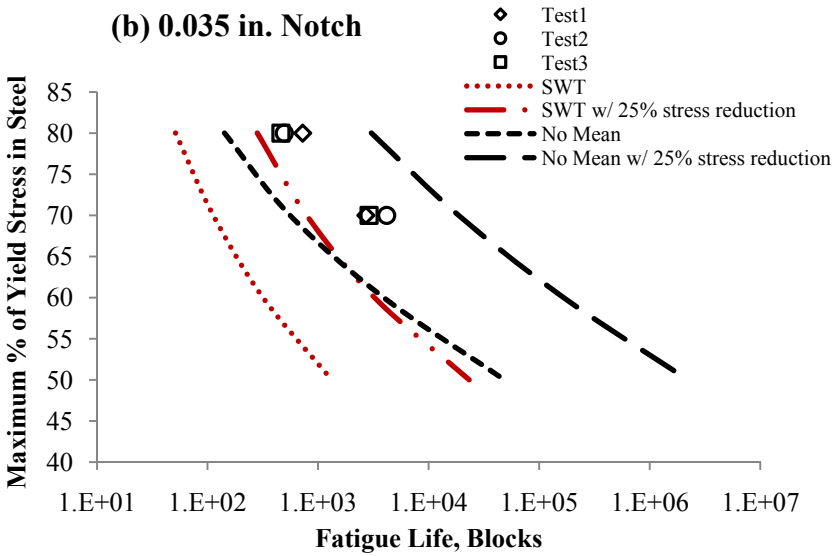

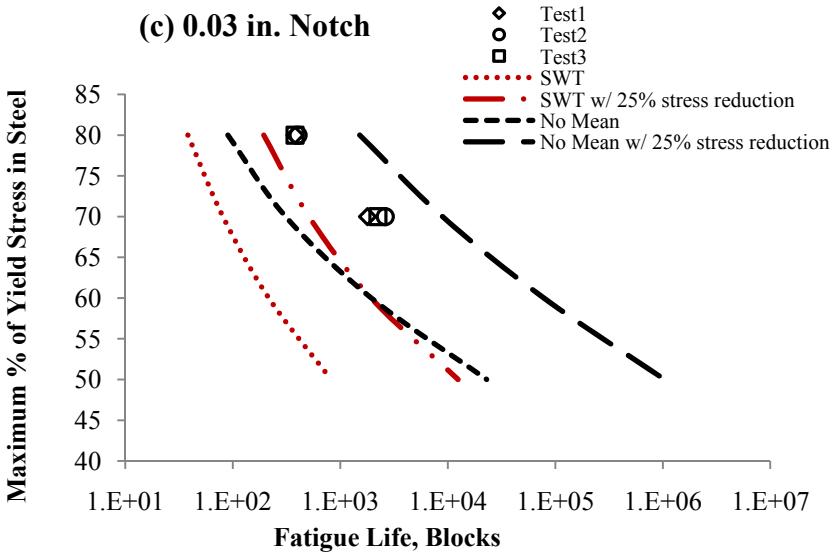

Figure 5.14 Experimental and estimated results for two-range variable amplitude loading - 1b prototype fatigue sensor

5.4. Variable Amplitude Experiments II– Multiple Load Ranges

Moving one step further to actual loading in a bridge, the response of deep "U" notched Al prototype fatigue sensors to multiple load ranges was examined. The experimental load histories were created using multiple load ranges to imitate a typical truck response in a typical highway bridge (see Figure 5.15).

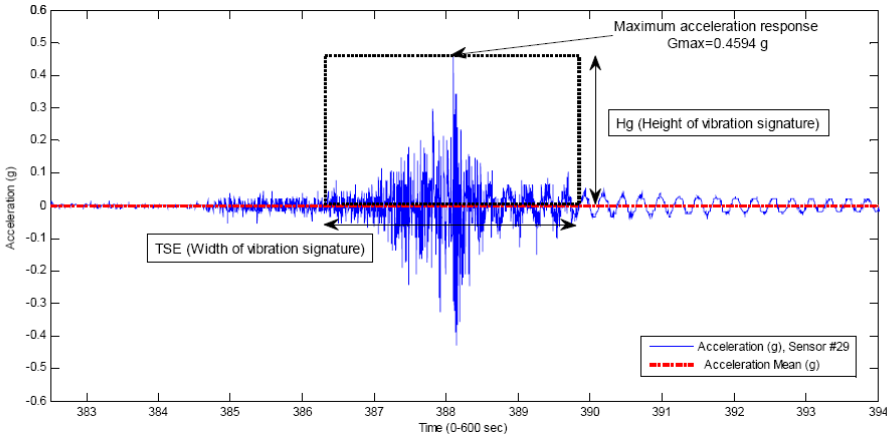

Figure 5.15 Acceleration time history of a truck response in a typical highway bridge (Bhachu 2010)

In doing so, it was assumed the above acceleration time history would produce a similar displacement time history induced by a similar load history. If the peak of the above acceleration was considered as the upper limit, i.e. to 80% of the yield stress of the carrier, then the lowest load range should be around 10%-20% of the yield stress of the carrier to represent the scaling of the above acceleration time history. However, due to the limitation in laboratory testing, 50% of the yield stress of steel was chosen as the lower limit in order to have better results within a reasonable time frame. Two load histories were created for laboratory experiments within these two limits (see Figure 5.16 for a representation of the two histories).

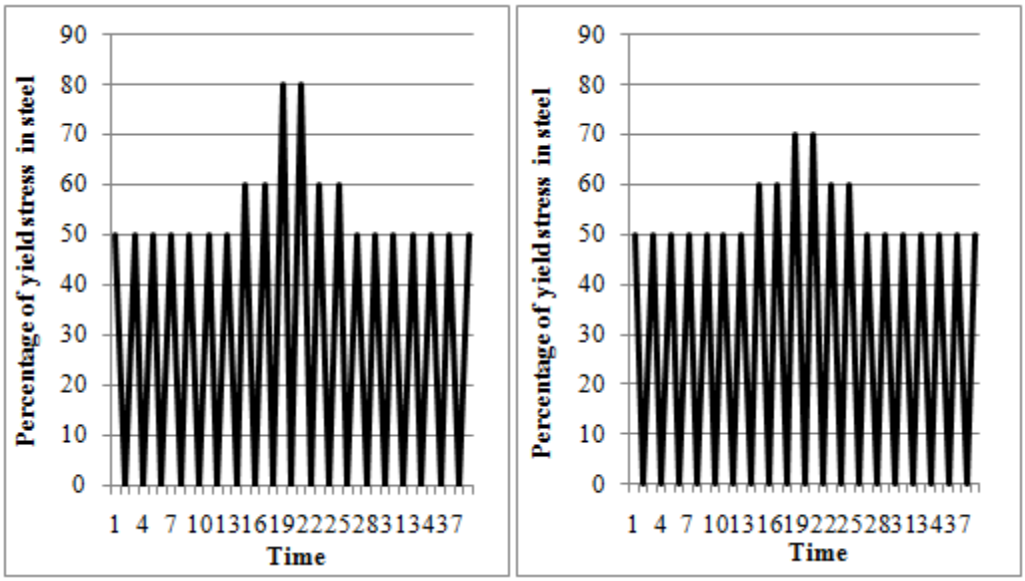

Figure 5.16 Two represesntative load histroies utilized in multiple-range variable amplitude experiments

5.4.1. Experimental procedure

Similar to two-range variable amplitude experiments, the load combinations were programmed in the MTS using the MPT. Each combination consisted of 20 cycles, which is one block of loading (see Figure 5.16), and the excitation frequency was set to 1Hz. Specimens were prepared following the same procedure as in constant amplitude and two-range variable amplitude experiments. Similar to two-range variable amplitude experiments, only 1b prototype geometry was used and the sensors were cut with a rolling direction perpendicular to the loading direction. Prototype sensor arms were separated along their arm lengths by carefully drilling them through sensor thickness in order to attach them to the DAQ. Four experiments were carried out for each load combination and the data was collected at 50 Hz initially and then was increased up to 200Hz.

5.4.2. FE modeling and Simulation

Fatigue life estimations were carried out following the same procedure adopted in two-range variable amplitude analysis. The same FEA results were used to calculate fatigue life for the two load histories using Miner's damage summation rule. Similar to previous analyses, 25% stress reduction curve was created to account for any stress attenuation due to the adhesive. Life calculations for two load histories are given in APPENDIX F.

5.4.3. Results and Analysis

Fatigue life results obtained for two multiple-range variable amplitude load histories are plotted in Figure 5.17a, Figure 5.17b and Figure 5.17c for .04 in., 0.035 in., and 0.03 in. notches respectively. These are plotted as the maximum percentage of the yield stress in the carrier versus fatigue life (experimental and estimated) in blocks. Only the SWT mean stress correction curve is plotted.

Similar to two-range variable amplitude results, experimental results for multiple-range load histories showed higher lives than estimated with SMT mean stress method. Some experimental values were even beyond the 25% stress attenuation curve, thus indicating possible attenuation of stress. The most important observation is the larger scatter in the experimental data compared to constant amplitude and two-range variable amplitude experiments. The poor repeatability of the experimental results demands a larger number of experiments to be carried out for each load history.

Overall, larger lives obtained through variable amplitude loading experiments show similar trends to those found in the literature. In general, for block loadings (similar to the above load histories), it is common to obtain a larger scatter than constant amplitude loading. Moreover, for some cases, Miner's Rule does not provide accurate

predictions for variable amplitude life, depending on the type of loading sequence (Zhang 2006b). It therefore emphasized the need for deploying other damage summation methods, i.e. non-linear methods (discussed in Section 2.1.2.2) for comparison.

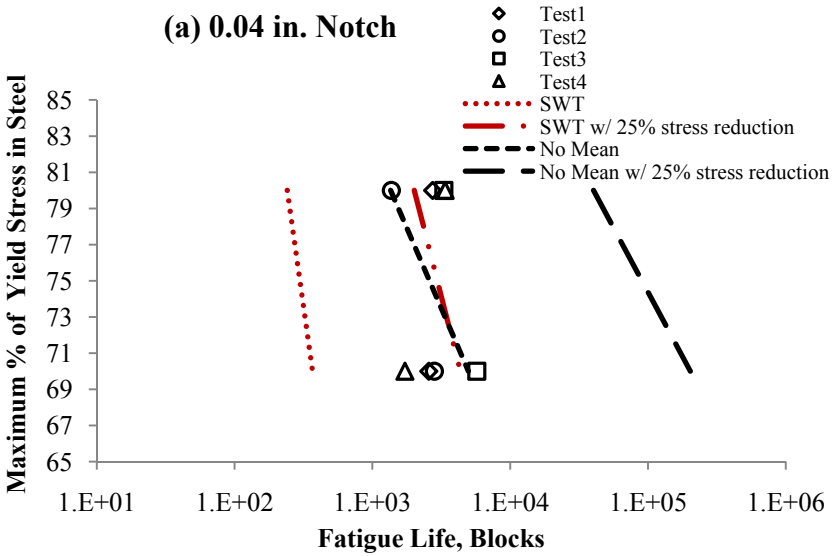

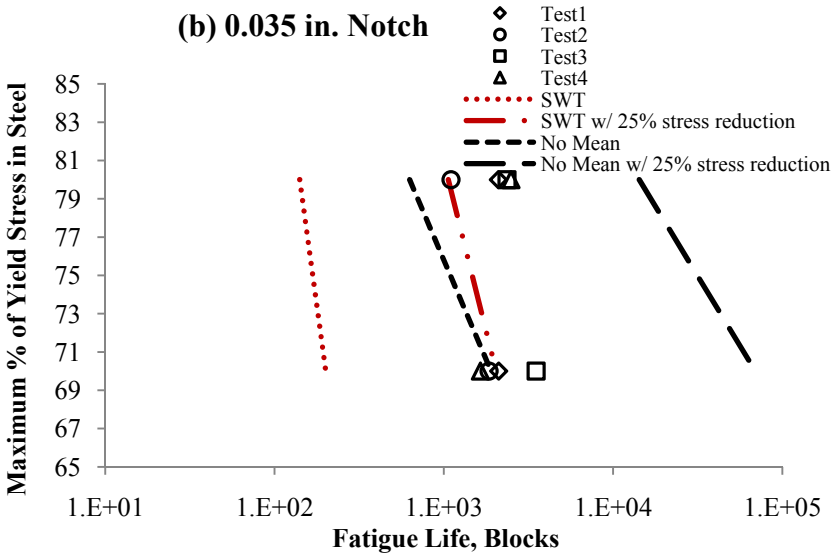

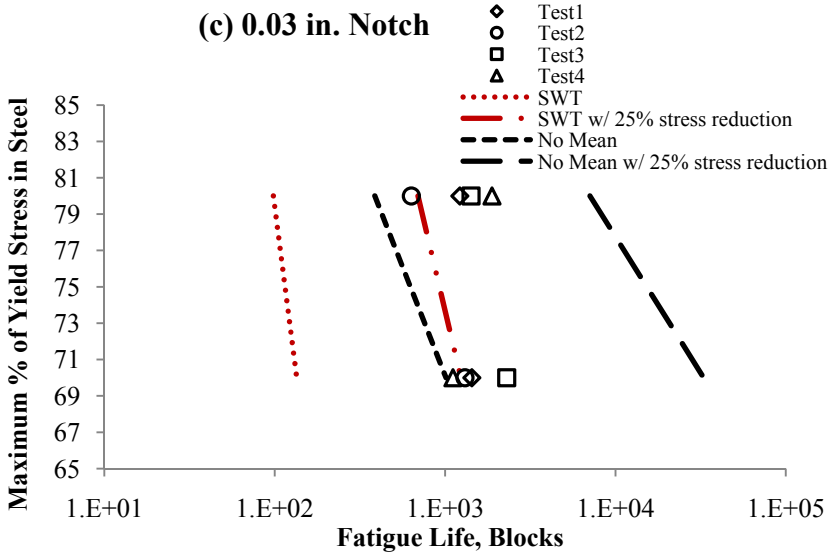

Figure 5.17 Experimental and estimated results for multiple-range variable amplitude loading – 1b prototype sensor

Discussion: Variable Amplitude Results

Regardless of the reliability issues associated with Miner's Rule for variable amplitude loading, it is worthwhile to investigate other possibilities which may have contributed to this deviation. Higher lives obtained from the two types of variable amplitude experiments may be attributed to multiple reasons. One possible explanation might be that prototype fatigue sensors have experienced some compressive stresses which lead them to longer fatigue lives than estimated. Any plastic deformation that may have occurred at notch roots due to yielding of the material can increase lengths of the corresponding arms to some extent, even by a small amount. When unloading and crack closure occur, these elongated arms can create compressive stresses at the prototype sensors while affecting the fatigue lives of other notches. Since the compressive mean stresses increase the fatigue life while tensile mean stresses decrease, longer lives obtained from variable amplitude loading may be attributed to this phenomenon. However, if it was the main reason for obtaining longer experimental lives than estimated, then it would have affected the constant amplitude experiments in the same way. Such a deviation was not observed in constant amplitude experiments. Therefore, it is possible that several other factors may have contributed to this, in addition to compressive mean stresses.

Material anisotropy causes significant variations in fatigue properties in metals, especially in their fracture toughness values (Broek 1986). The rolling direction of the material creates such variations in grain orientation (Meyers 1986) and in grain size (Pedersen 1986). Experimental results obtained from 7075-T6 series plate Al show that the specimens oriented in a longitudinal (rolling) direction, and crack growth in

transverse direction (L-T specimens), give higher fracture toughness values, i.e. longer fatigue lives, than the specimens oriented in transverse direction, and crack propagation in longitudinal direction (T-L specimens) (U.S Department of Defense. 2003). It was noticed that the prototype Al sensors tested under constant amplitude loading were L-T specimens whereas the sensors tested under variable amplitude loading were T-L. Therefore, considering the material microstructure, particularly the grain direction, L-T specimens utilized in constant amplitude experiments should give longer fatigue lives than T-L specimens utilized in variable amplitude tests. Since this was contrary to what was actually obtained from experimental results, the grain orientation seemed to have no considerable contribution towards this deviation.

For further investigation, the cracked notch surfaces from both T-L and L-T specimens were micrographed using a *Nikon ECLIPSE ME600* microscope. See Figure 5.18. A distinct variation in crack pattern and cracked surfaces was observed. Crack paths in T-L specimens showed considerable turning and twisting compared to L-T specimens. The fractured edges were also different from one another: L-T showed some brittle-like features with sharp crack edges, while T-L showed ductile-like smooth crack edges with considerably higher chipping on the surface.

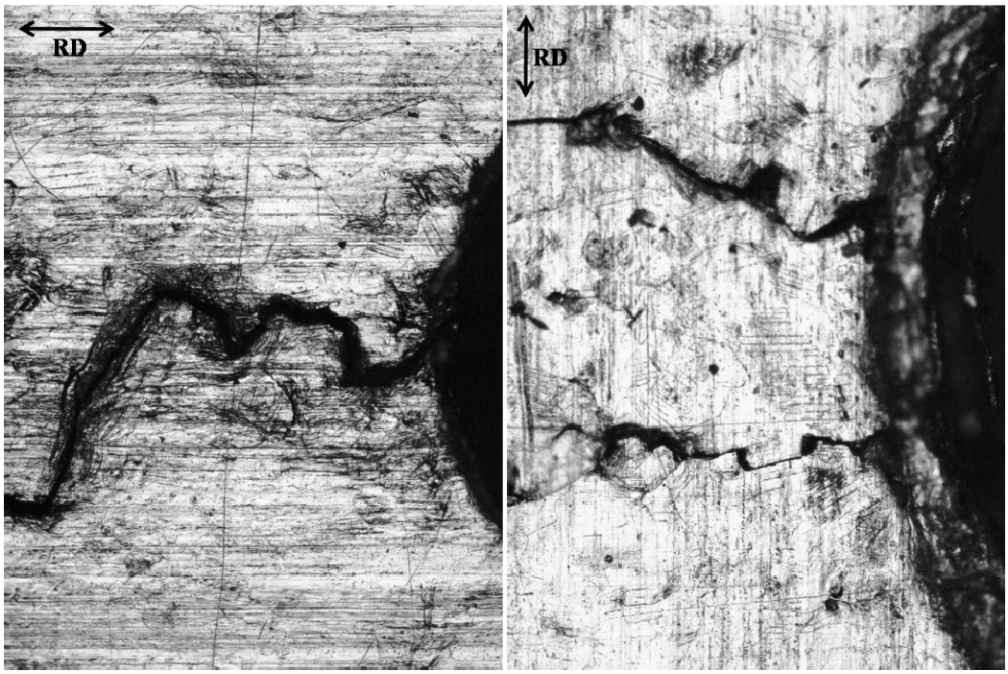

Figure 5.18 Micrographs of cracked notch surfaces (10×): T-L orientation, left; L-T orientation, right

5.5. Sensitivity Analysis of Deep "U" Notch Prototype In-Situ Fatigue Sensors

Sensitivity of material and geometric parameters on the numerical results are investigated in this section. Based on the comparison of experimental and numerical results discussed under the previous section, it was found important to examine the most sensitive parameters that influence the fatigue life of the prototype sensors so that the behavior of the sensor at different stress levels can be reliably predicted.

5.5.1. Sensitivity Analysis of Geometric Parameters

Geometric parameters that influence the fatigue life of the above prototype sensors are correlated to the SCF's of the sensor. Peterson (1974) presents SCF's for deep "U" notches, based on empirical results. The derived empirical relationship for deep "U" notches is,

$$K_{tn} = C_1 + C_2\left(\frac{2t}{H}\right) + C_3\left(\frac{2t}{H}\right)^2 + C_4\left(\frac{2t}{H}\right)^3 \qquad (5.1)\ \text{(Peterson 1974)}$$

where $K_{tn} = {}^{\sigma_{max}}/_{\sigma_{net}}$ and $\sigma_{net} = {}^{P}/_{hd}$. P is the applied tensile load, h is the thickness and d is the notch ligament. H is the width of the sensing arm and t is the depth of the notch. C_1,C_2, C_3 and C_4 are constants derived empirically which depend on ${}^{t}/_{r}$ ratio, where r is the radius of the notch. In addition, $K_{tg} = {}^{\sigma_{max}}/_{\sigma_{gross}}$

where $\sigma_{gross} = {}^{P}/_{Hd}$ and $K_{tg} = K_{tn}\left({}^{H}/_{d}\right)$. In this study we refer K_{tg} to K_t which is based on the nominal or gross area of the sensing arm.

According to the geometric parameters embedded in equation (5.1), r, H and t are the governing parameters of K_{tg} and K_{tn} and their influence can be graphed as shown in Figure 5.19. The sensor arm width, H changes linearly with K_{tg} while the notch diameter ($2r$) and the notch ligament (d) show a power distribution. According to the analysis results, the notch ligament plays a vital role in determining K_{tg} and so does the fatigue life of the notch. At notch ligaments less than 0.05 in., very high SCF's can be obtained. The relationship of these geometric parameters was effectively utilized in the design and development of the prototype in-situ fatigue sensor. In addition, by varying SCF's of several sensor arms in a single sensor it can effectively respond to varying stress ranges in an attached structure.

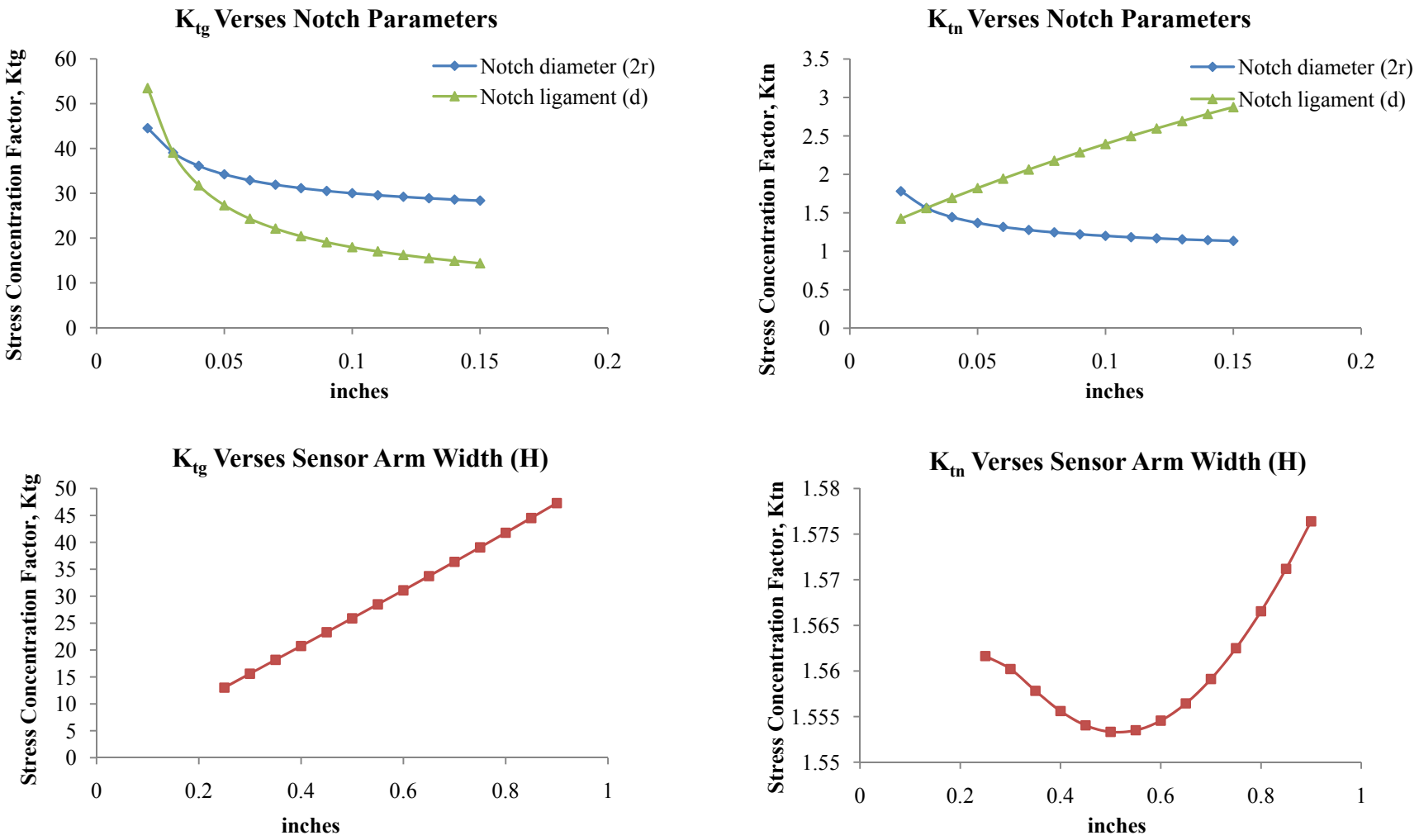

Figure 5.19 Sensitivity of the geometric parameters in stress concentration factor calculations

5.5.2. Sensitivity Analysis of Material Parameters: Strain-Life Parameters

Material parameters play a vital role in determining the fatigue life of sensing arms. The sensitivity of strain-life parameters in the cyclic stress-strain equation (2.13) and the strain-life equation (2.18) was investigated for a selected notch; the smallest notch (0.03 in. ligament with 0.03125 in. diameter) of 1b prototype sensor geometry. The SCF for this notch obtained previously through FEA, 38.61 (Table 5.3) was used for fatigue life estimations. Nominal stresses corresponding to the upper limit of each load level (80%-40% of yield strength of steel) obtained through FEA were considered for this analysis with SWT mean stress correction. Material properties of 7075-T6 Al given in Table 4.2 were used as fixed values while changing each parameter through the range indicated in Table 5.4.

Table 5.4 Strain-Life Parameters and Ranges used in the Sensitivity Study

Parameter	Minimum	Maximum	Interval
Fatigue Strength Coefficient (σ_f'), psi	50,000	150,000	20,000
Fatigue Strength Exponent (b)	-0.05	-0.1	-0.01
Fatigue Ductility Coefficient (ε_f')	0.2	0.7	0.1
Fatigue Ductility Exponent (c)	-0.3	-0.8	-0.1
Cyclic Strength Coefficient (K'), psi	100,000	150,000	10,000
Cyclic Strain Hardening Exponent (n')	0.1	0.2	0.02

According to the analysis results shown in Figure 5.20, a reasonable judgment can be made for the sensitivity of the strain-life parameters. When parameters b and c are compared (see Figure 5.20b and Figure 5.20d) it can be observed that b is more sensitive than c and its sensitivity becomes less prominent at higher c values than at lower c values and the sensitivity increases with lower stress levels, i.e. 40% yield. Comparing ε_f' with c (see Figure 5.20c and Figure 5.20d), c is more sensitive than ε_f' and its sensitivity increases with higher stress levels. When σ_f' and K' are compared (see Figure 5.20a and

Figure 5.20e) $\sigma_f^{'}$ shows a much higher sensitivity than $K^{'}$ especially at its lower parameter values and becomes less sensitive at higher values. This trend seems common at all stress levels. In both $n^{'}$ and b (see Figure 5.20f and Figure 5.20b), the sensitivity increases with lower stress levels, but b is much more sensitive than n'.

According to the sensitivity analysis, strain-life parameters $\sigma_f^{'}$, b, and c play vital roles in the fatigue life of the prototype sensor within the stress levels analyzed. With only 1% change in parameter value, a 5.3% change of the fatigue life was noticed in $\sigma_f^{'}$, a 2.5% change in b and a 3.9% change in c at the nominal stress corresponding to 80% of the yield of the carrier. For the nominal stress corresponding to 40% of the yield stress of the carrier, 13.6%, 10.8% and 0.448% changes in fatigue lives were observed for parameters $\sigma_f^{'}$, b and c respectively.

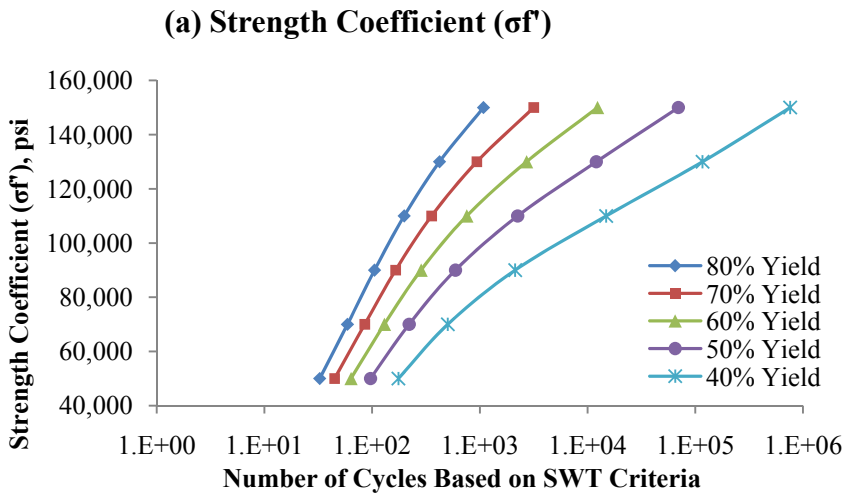
(a) Strength Coefficient (σf')
Strength Coefficient (σf'), psi
160,000
140,000
120,000
100,000
80,000
60,000
40,000
1.E+00
1.E+01
1.E+02
1.E+03
1.E+04
1.E+05
1.E+06
Number of Cycles Based on SWT Criteria
80% Yield
70% Yield
60% Yield
50% Yield
40% Yield

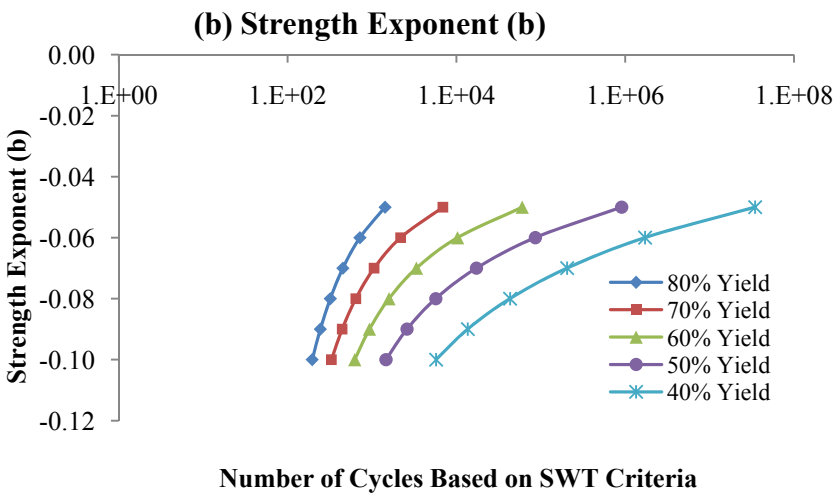
(b) Strength Exponent (b)
Strength Exponent (b)
0.00
-0.02
-0.04
-0.06
-0.08
-0.10
-0.12
1.E+00
1.E+02
1.E+04
1.E+06
1.E+08
Number of Cycles Based on SWT Criteria
80% Yield
70% Yield
60% Yield
50% Yield
40% Yield

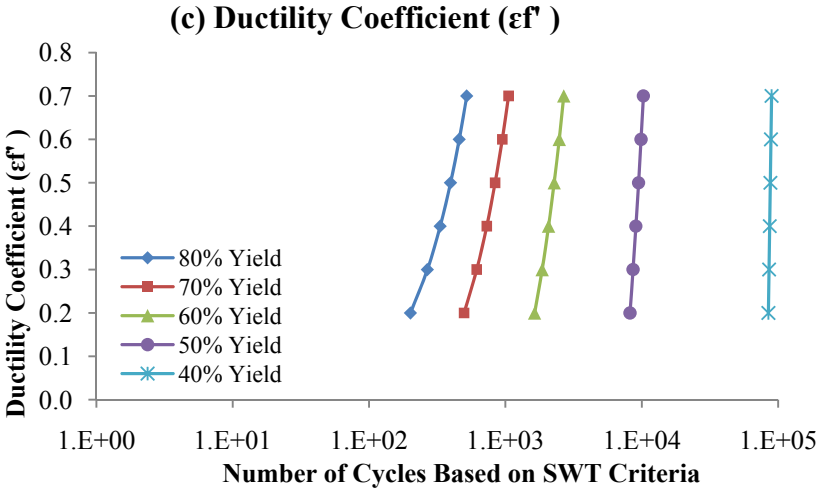
(c) Ductility Coefficient (εf')
Ductility Coefficient (εf')
0.8
0.7
0.6
0.5
0.4
0.3
0.2
0.1
0.0
1.E+00
1.E+01
1.E+02
1.E+03
1.E+04
1.E+05
Number of Cycles Based on SWT Criteria
80% Yield
70% Yield
60% Yield
50% Yield
40% Yield

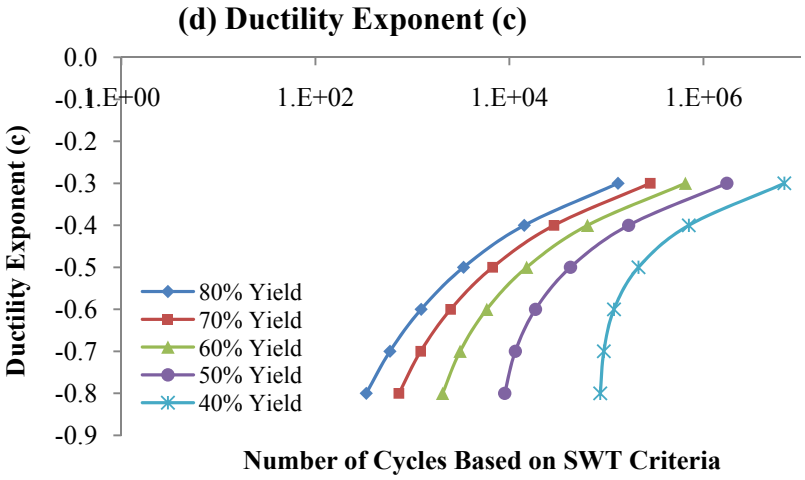
(d) Ductility Exponent (c)
Ductility Exponent (c)
0.0
-0.1
-0.2
-0.3
-0.4
-0.5
-0.6
-0.7
-0.8
-0.9
1.E+00
1.E+02
1.E+04
1.E+06
Number of Cycles Based on SWT Criteria
80% Yield
70% Yield
60% Yield
50% Yield
40% Yield

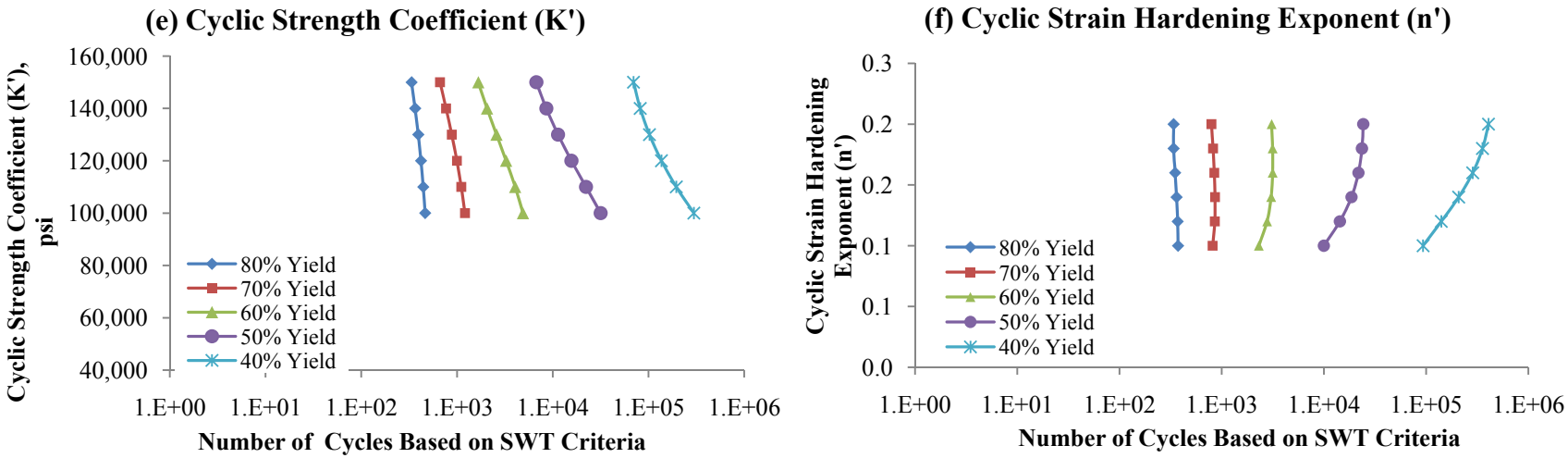

Figure 5.20 Sensitivity analyses of strain-life parameters

5.5.3. Discussion

According to the results of the sensitivity analysis, it is crucial to obtain the most accurate strain-life parameter values for the material of interest. Unfortunately there are not many data sources available for this purpose. The reference publication for strain-life parameters for 7075-T6 Al used in this study dates back to 1969 (Endo 1969; Topper 2009) by Endo and Morrow. Endo and Morrows' (1969) used hourglass circular rods with 0.25 in. notch diameter as their fatigue test specimens to derive these parameters. Since 0.032 in. plate materials was for the deep "U" notch prototype sensors discussed in this chapter and this thickness is below the lower limit (0.1 in.) of the ASTM standards, the need of self-derived material parameters are justified. Future experimental work based on this research should focus on obtaining these material parameters, which will tremendously help in building more accurate and reliable life predictions for the future sensor designs. Most importantly, obtaining measurement data would enable researchers to carry out an error propagation analysis to determine the error propagation/uncertainly in each measured parameter toward the final fatigue life, which will ultimately produce more complete sensitivity analysis results. Following is the criterion for an error propagation analysis provided that the raw measurement data for strain-life parameters are available.

Error Propagation Analysis - Criterion

The governing equation for error propagation analysis is the strain-life equation (5.2).

The strain amplitude, $\varepsilon_a = \Delta\varepsilon/2$ as discussed in Chapter 2 under Section 2.2.1.

$$\varepsilon_a = \frac{\sigma_f'}{E}\left(2N_f\right)^b + \varepsilon_f'\left(2N_f\right)^c \tag{5.2}$$

Assume that the measured errors in variables σ_f',E, b, ε_f' and c in the strain-life equation (5.2) as $\delta_{\sigma_f'}$, δ_E, δ_b, $\delta_{\varepsilon_f'}$, and δ_c respectively.

The variation of functions with respect to variables σ_f',E, b, ε_f' and c, therefore, can be taken as $\delta_{f\_\sigma_f'}$,δ_{f_E}, δ_{f_b}, $\delta_{f\_\varepsilon_f'}$ and δ_{f_c} respectively. Using the derivation method,

$$\delta_{fx} = \left(\frac{\delta f}{\delta x}\right)\delta_x \tag{5.3}$$

the variation of functions can be determined as follows.

$$\delta_{f\_\sigma_f'} = \left(\frac{\partial \varepsilon_a}{\partial \sigma_f'}\right)\delta_{\sigma_f'} \text{ where } \frac{\partial \varepsilon_a}{\partial \sigma_f'} = \frac{(2N_f)^b}{E} \tag{5.4}$$

$$\delta_{f\_E} = \left(\frac{\partial \varepsilon_a}{\partial E}\right)\delta_E \text{ where } \frac{\partial \varepsilon_a}{\partial E} = -\frac{\sigma_f'(2N_f)^b}{E^2} \tag{5.5}$$

$$\delta_{f_b} = \left(\frac{\partial \varepsilon_a}{\partial b}\right)\delta_b \text{ where } \frac{\partial \varepsilon_a}{\partial b} = \frac{\sigma_f'}{E}(2N_f)^b(\ln 2N_f) \tag{5.6}$$

$$\delta_{f\_\varepsilon_f'} = \left(\frac{\partial \varepsilon_a}{\partial \varepsilon_f'}\right)\delta_{\varepsilon_f'} \text{ where } \frac{\partial \varepsilon_a}{\partial \varepsilon_f'} = (2N_f)^c \tag{5.7}$$

$$\delta_{f\_c} = \left(\frac{\partial \varepsilon_a}{\partial c}\right)\delta_c \text{ where } \frac{\partial \varepsilon_a}{\partial c} = \varepsilon_f'(2N_f)^c(\ln 2N_f) \tag{5.8}$$

The total error (δ_{f_total}) is obtained by adding the individual contributions in quadrarure.

$$\delta_{f\_total} = \sqrt{{\delta_{f\_\sigma_f'}}^2 + {\delta_{f\_E}}^2 + {\delta_{f_b}}^2 + {\delta_{f\_\varepsilon_f'}}^2 + {\delta_{f\_c}}^2} \tag{5.9}$$

In order to solve the equation (5.9) it is necessary to obtain measured errors $\delta_{\sigma_f'}$, δ_E, δ_b, $\delta_{\varepsilon_f'}$, and δ_c from a set of experimental data. The standard error δ is calculated by $\delta = \frac{\sigma}{\sqrt{N}}$ where σ refers to the standard deviation of the measured values and N is the number of measurements.

Values for strain-life parameters can be obtained through standard fatigue testing following the ASTM E-606 (standard recommended practice for constant amplitude low-cycle fatigue testing). However, the recommended specimen and loading profile needs to be changed to suit the sheet thickness of the prototype fatigue sensor (0.032 in) since ASTM E-606 recommendations are limited to rectangular cross section only up to 0.1 in. thickness. Obtaining measured values for strain-life parameters and calculating error propagation according to the above criterion is a future area of focus of this research.

CHAPTER 6. OTHER APPROACHES

Different materials, methods and approaches were explored during the development process of the prototype in-situ fatigue sensor (1) to identify appropriate materials for the sensor, (2) to identify successful attachment options (3) and to explore effective and successful test configurations under the limitations of available resources, laboratory conditions, and the timeline (to accumulate a large number of cycles). These other approaches, their limitations and problems encountered at different stages of the development of the prototype fatigue sensor are discussed in this chapter.

6.1. Sensor Materials and Attachment Options

6.1.1. Thin Cu Film as Sensor Material

The possibility of using other sensor materials than 7075-T6 Al was explored. Thin Cu film was utilized in several experiments to see its behavior as a possible candidate. Prototype sensors cut from 5 mil thick Cu foil were tested under a fully reversed cantilever test configuration, 3-point bending test setup and axial tension test configuration which will be explained in Section 6.2.1.

The main issue associated with Cu foil sensors was the flexibility of the material, which makes it difficult to obtain high precision in cutting and handling. Based on preliminary experimental and simulation results, it was confirmed that the high precision laser cutting was essential to achieve good experimental results that can be predicted well through simulation. This was difficult to achieve by manual cutting or cutting using a template.

The other issue was the Cu foil sensors' higher susceptibility to surface scratches while handing. Since a small surface flaw can change the fatigue life of the associated notch significantly, any type of handling errors, especially during attaching them to carrier beams, were not desirable. Experimental results obtained from Cu film prototype sensors confirmed the need for a thicker sensor material than thin films. Either Cu, steel or Al, that is electrically conductive may serve this purpose. The main reason for choosing 7075-T6 Al for further testing (Chapter 5) was due to its availability of strain-life fatigue parameters and well-characterized material behavior.

6.1.2. Attachment Options

Different attachment options were explored to attach sensors to the carrier beam, i.e., fully-attached to edges-only- attached, with adhesives, and by mechanical attachment. The fully bonded option using adhesives failed to provide good results; this was also confirmed by FEA results as shown in Figure 6.1. This FE simulation was carried out to imitate the fully reversed, cantilevered test setup with thin Cu prototype sensors with "V" shaped notches. The left sensor was fully bonded, while the sensor on the right was attached from its edges only, and only the latter was able to show stress concentrations at its notches. The edge bonded option using adhesives, reduced the fatigue life of notches and increased the sensitivity of prototype sensors. Therefore, for the Al prototype fatigue sensor experiments described in Chapter 5, the edge bonded option was chosen.

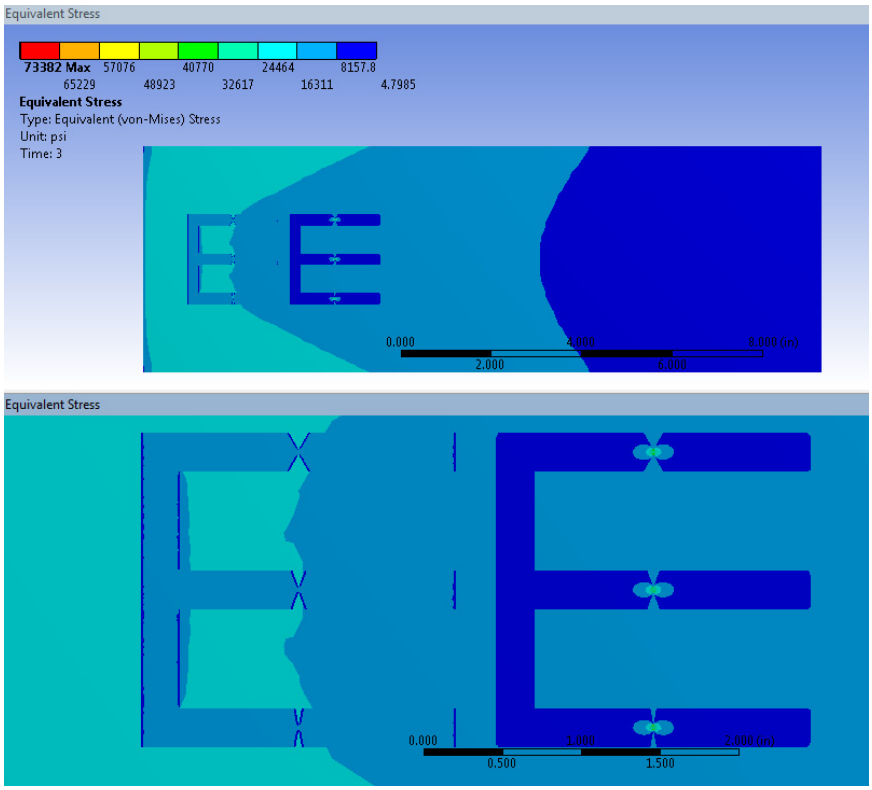

Figure 6.1 Equivalent stress results from ANSYS WB for thin Cu prototype sensors: left sensor - fully bonded, right sensor - edge bonded

Mechanical attachment methods may possibly prevent issues related to adhesives such as longer curing time, attenuation of stress (Chapter 5) and non-uniform bond layers. In addition, it may prevent such issues related to numerical life estimations. NDE being a major concern in this research, the possibility of applying mechanical attachment methods for actual bridges is limited – or may not feasible at all. However, for laboratory testing, the behavior of the bolted connection was checked out. The connection was found unsuccessful due to premature fatigue failure at bolt holes.

6.1.3. Adhesives, Electrical Insulation and Wiring

Adhesives and Insulation

The behavior of adhesive was important not only for attaching sensors to the beam, but also for providing an electrical insulation to sensors to measure voltage in sensor arms.

Several types of adhesives were tested. A typical acrylic based strain gauge adhesive (*M-Bond200,* which is recommended by *VISHAY* (2008) for crack detecting sensors, was used. Using *M-Bond200* alone as an insulator for Cu film prototype sensors was not successful because in long duration tests, this adhesive became dry and showed chipping while losing its bond and the insulation capability. This problem was somewhat controlled by using a polyurethane coating (*VISHAY M-CoatA* - general purpose laboratory coating), typically used in strain gauge installation to avoid drying. Having emphasized the need of a separate insulation layer, PI film was introduced as an insulator and as a backing material for thin Cu prototype sensors, which will be discussed further in the following section.

Another acrylic based adhesive that was successfully used was the *3M DP-810* (Chapter 5). However, the uncertainty of the duration it takes to achieve its full strength is yet to be resolved through a separate parametric study. For some trial tests, which utilized Plexiglas (used as an insulator) and Al, (see Figure 6.2) *DP-810* did not perform well. The Al-Plexiglas bond failed after approximately 500,000 cycles when ran at 0.05 in. amplitude sine excitation with a frequency of 13Hz. This indicated a bonding issue of this adhesive with plastics under HCF regime. A similar issue was encountered with Cu-PI bond using *DP-810.* Moreover, higher viscosity as mentioned in Section 5.2.2 makes this adhesive difficult to apply on thin Cu and PI films to maintain an even bond.

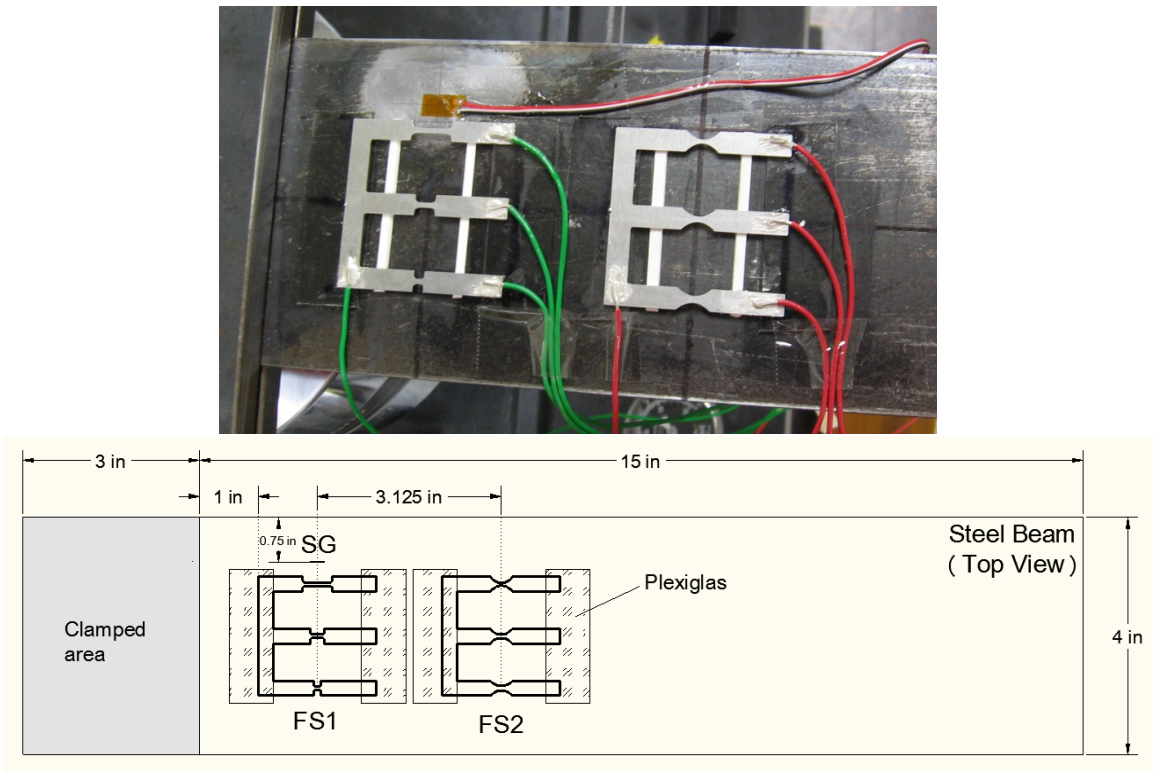

Figure 6.2 Al prototype sensors edge-bonded using Plexiglas: test specimen, top; schematic of the specimen layout for cantilevered testing, bottom

Electrical Wiring

Wiring prototype sensors to the DAQ was a concern throughout testing. Al prototype sensors, shown in Figure 6.2, encountered problems such as loosening of attached wires and fatigue failure at wired connection at a higher number of cycles. Since the typical solder does not work for Al soldering due to the presence of heavy Al Oxide (Al_2O_3), Silver Conductive Epoxy (*MG Chemicals Silver Conductive Epoxy 14G)* was used to attach wires to Al sensors. A problem with this epoxy is that it failed at a higher number of cycles, typically $>10^6$ cycles. This issue can be solved by using Sn/Zn based Al solder. However, special care must be taken not to overheat the sensor material during the soldering process, which may affect the fatigue properties of the sensor.

6.1.4. Backing Material for Thin Cu Films

As mentioned earlier, for thin Cu sensors, the role of adhesive as an electrical insulator was not successful and the need for a backing material was confirmed. After several trials 3 mil PI was identified as a good candidate. In fact, it is one of the common backing materials used in typical foil strain gauge packaging (Vishay 2008). *DuPont Kapton 300 HN (DuPont 2009a)* PI sheets were used as a backing material for the prototype sensors made of thin Cu film. Several experiments were carried out with 5 mil Cu film as the prototype sensor material and 3 mil PI as the backing material (see Figure 6.3). These were bonded together using the two types of adhesives discussed before.

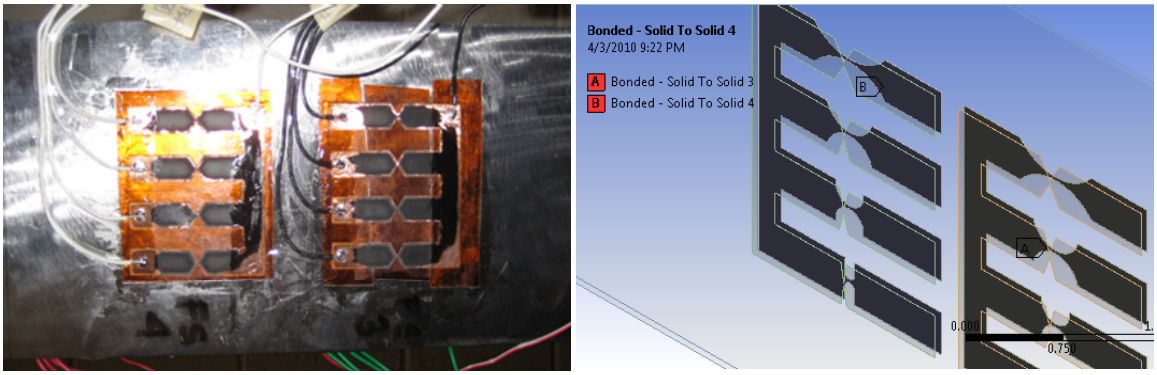

Figure 6.3 Testing and simulation of thin Cu film sensors on PI backing: a test specimen (top face), left; corresponding FE model with layered sensors on either sides of the beam, right

As mentioned before, none of the above adhesives were able to create a firm bond with PI. According to the PI manufacturer, *Pyralux® LF* and *Pyralux® FR* adhesives are good candidates for this purpose. However, the process of bonding using these modified acrylics, which are made of thermoplastics and thermosets, needs to be performed in a lamination press under heat and pressure, which was not feasible.

The use of flexible circuit materials as an alternative was explored. This option may prevent the press lamination or even the entire lamination layer. Two types Cu-PI

flexible circuit materials were found manufactured by *DuPont* (2009b) that can be used as possible sensor materials (see Figure 6.4).

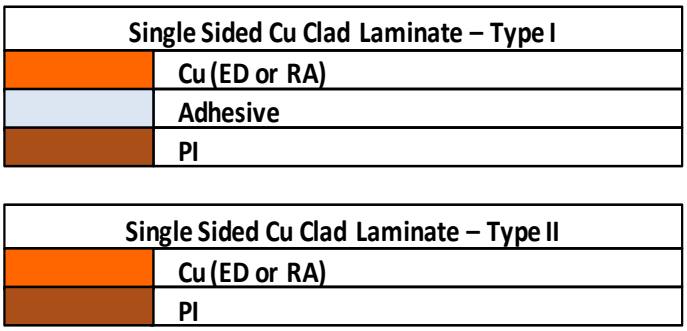

Figure 6.4 Two types of flexible circuit materials

Pyralux® LF is a Cu clad laminate which has an adhesive layer in between Cu and PI. Cu can be either electro-deposited (ED) or rolled, annealed (RA). *Pyralux® AC* may be a better option than the previous, because it does not include an adhesive layer which simplifies the sensor material properties and avoids the burden of characterizing the adhesive. For testing purposes, the second type of flexible circuit material was obtained which has 0.5 mil Cu on 1 mil PI (both EA and RA options).

However, cutting these materials was an issue. Due to the PI lamination, typical laser cutting did not work. Either chemical etching or high precision commercial laser cutting was needed. This aspect needs to be addressed in the future, depending on the future scope of the project.

6.2. Test Setup and Monitoring

6.2.1. Test Setups

Test setups utilized in this research were, (1) axial tensile loading with fixed-fixed boundary conditions, (2) 3-point bending with simply supported boundary conditions and (3) cantilevered bending setup with “fixed”-free boundary conditions. Out of these, the first option was found to be the most successful configuration, which is discussed at

length under Section 4.1.1. The other types of test setups, their advantages and disadvantages are discussed next.

6.2.1.1. Three-Point Bending with Simply Supported Boundary Conditions

In a 3-point bending test setup, as shown in Figure 6.5, the supports were set up to simulate pin-pin boundary conditions with a 12 in. span. The test parameters in the MTS were setup so that the beam would always experience a compressive stress. This was mainly due to the difficulty in reaching a zero load value in the MTS. All experiments conducted under 3-point test setup were performed between 0.1 - 1 Hz frequency. Higher frequencies were difficult to achieve for this loading setup in the MTS. When the frequency was raised from 0.1 Hz to 1 Hz, a noticeable difference between the estimated and measured values of displacements was noticed. This could be attributed to the discrepancies at the pin connections due to the increased frequency, which causes the joints to move away from the "ideal" pin-pin condition.

FE analyses were carried out for each experiment to obtain a stress-strain response from the beam and to predict the fatigue lives of the attached prototype sensors. Experimental strain values were used to validate the FE model. Shown in Figure 6.7 are typical analysis settings for 3-point bending test setup and normal stresses obtained from ANSYS WB.

An advantage of this setup is that, similar to the axial tensile setup, characterization of the behavior of the attached prototype sensors was straightforward because the stress field in the beam can be easily calculated and verified by strain measurements.

Figure 6.5 Test setup for 3-point bending in the MTS

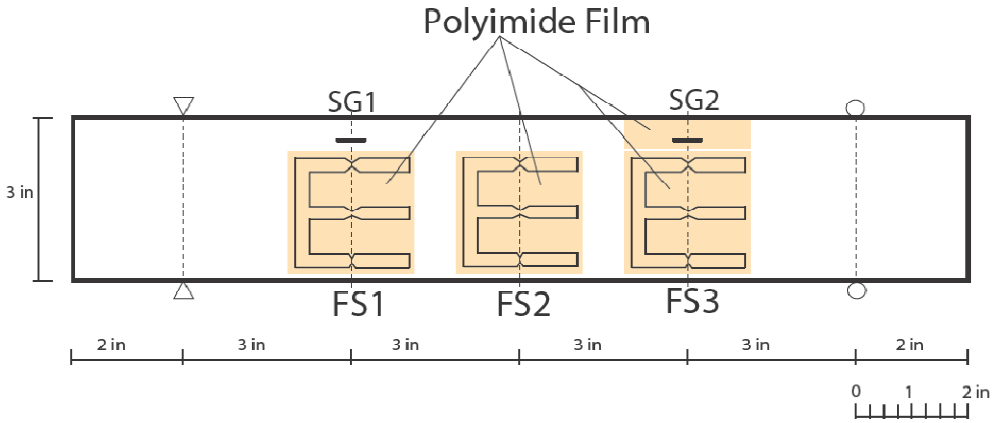

Figure 6.6 A test specimen layout for 3-point bending test with three Cu-PI sensors and two strain gages

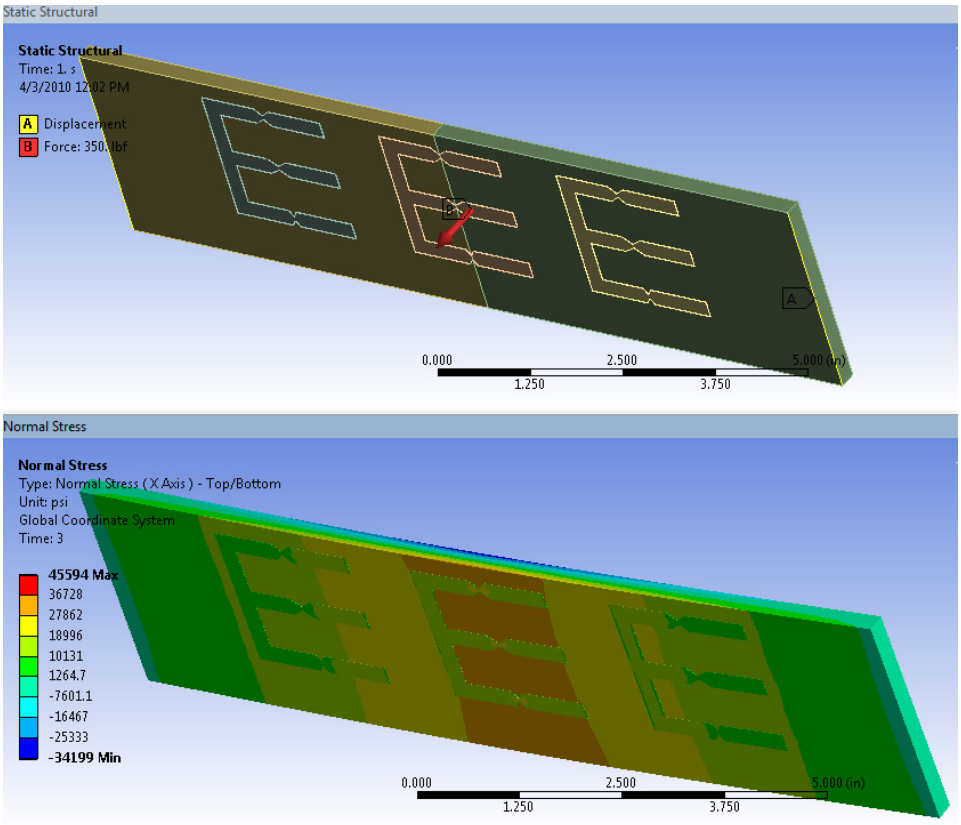

Figure 6.7 FEA of a 3-point bending experiment: analysis settings, top; normal stress (X axis) results, bottom

6.2.1.2. Cantilevered test setup with "fixed"-free boundary conditions

The cantilevered test setup is commonly used in fatigue testing due to its robustness to accumulate large number of cycles. The feasibility of the cantilevered setup with fully reversed loading was explored in this research. A separate fixture was fabricated with bolts, to fix the specimen to the MTS grips and to obtain fixed boundary conditions as shown in Figure 6.8. Excitation frequencies for each test were setup according to the estimated and observed natural frequencies of the beam used for each test. The behavior of the prototype sensors were examined at the resonance frequency and at lower frequencies of the attached beam. The main advantage of cantilever test setup was its ability to excite test specimens at relatively higher frequencies. This drastically reduced testing time.

However, there are major drawbacks in this setup. First, the stress field was not uniform. The bending stress associated with the sensor was difficult to obtain through baseline calculations since the test setup did not necessarily simulate the ideal fixed-free boundary conditions. The calculated natural frequencies for fixed-free boundary conditions were a little higher than those observed during testing. Second, it was difficult to attach sensors at the highest stress field of the beam, i.e. closer to the clamped edge. This is because the stress filed was not uniform at the connection due to the Saint-Venant's principle, and it was difficult to estimate the stress associated with the sensor. Finally, due to vigorous vibration of the beam, issues such as rubbing of attached wiring, loosening of the bolts and premature failure of the beam at the connection were encountered.

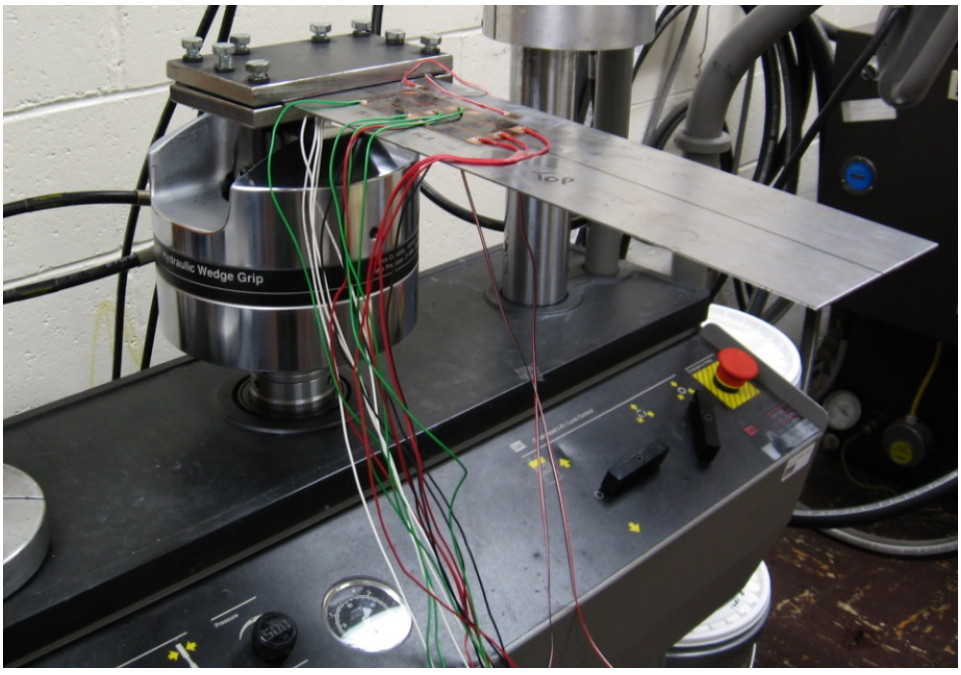

Figure 6.8 Cantilever test setup in the MTS

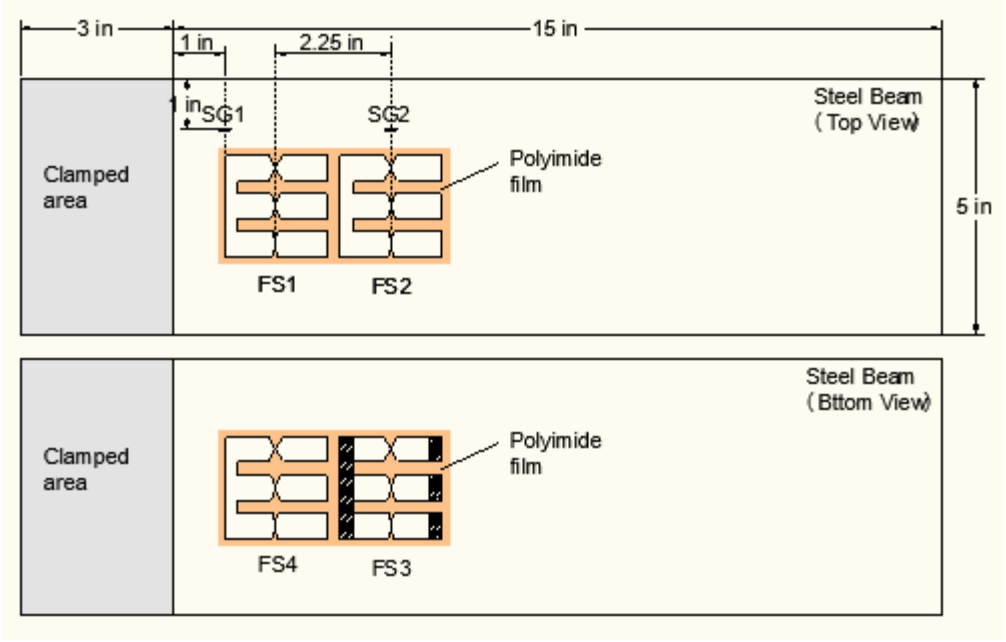

Figure 6.9 A schematic of a test specimen layout for fully reversed cantilever setup with four prototype Cu-PI sensors and strain gages attached

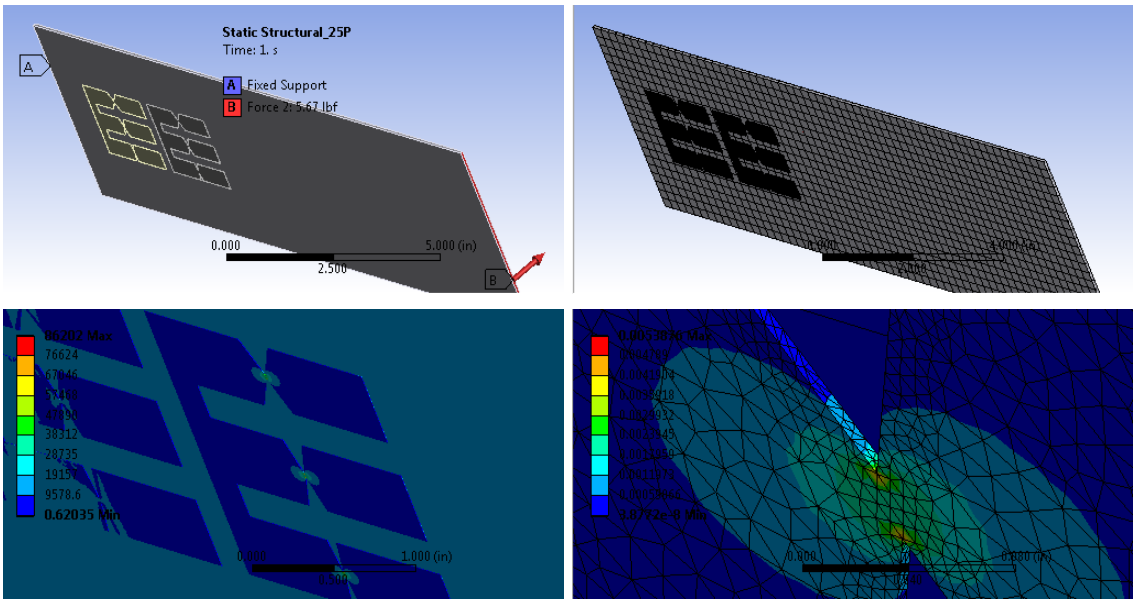

Figure 6.10 FEA of a cantilevered test: analysis settings, top left; meshed model, top right; Von-Mises stress (edge-bonded sensor), bottom left; Von-Mises elastic strain (edge-bonded top notch), bottom right

6.2.2. Monitoring of Fatigue Results

Monitoring and saving of fatigue results were important in long duration experiments, to avoid the burden of watching the test from start to end. The DAQ was of great help in this regard. However, due to some variations in failure characteristics of the notches that were associated with certain test configurations, the following issues were encountered during the monitoring process.

Even though a clear stepped voltage output was expected upon failure of each arm in an actual test, this was not observed, especially under the fully reversed cantilevered test setup. It showed a stepped wave instead of a straight line. This was because of re-touching and re-connecting of broken notches due to fully reversed vibration. See Figure 6.11, Figure 6.12 and Figure 6.13 for plots obtained at three different stages during breaking of a notch under fully reversed cyclic loading.

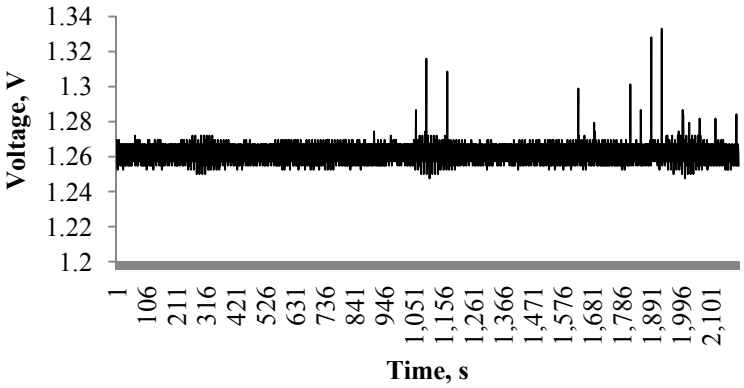

Figure 6.11 Voltage output: Initial stage of breaking

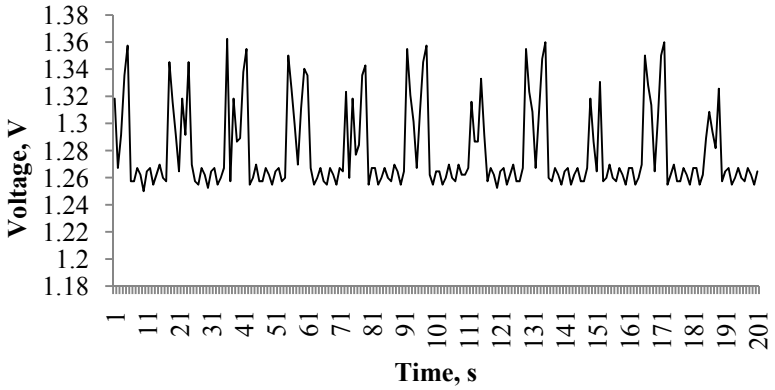

Figure 6.12 Voltage output: Intermediate stage of breaking

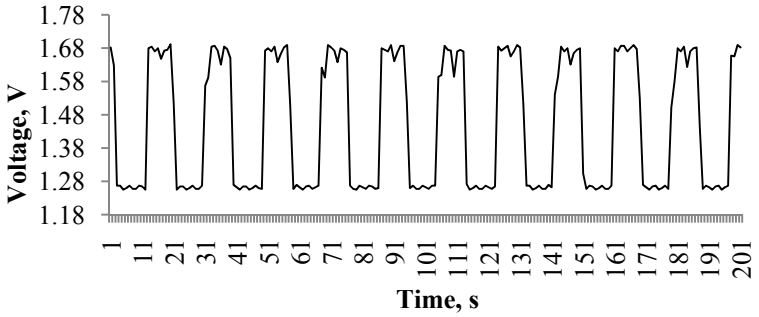

Figure 6.13 Voltage output: A broken notch retouching during fully reversed loading

However, this problem was not a significant issue for other types of test configurations, i.e. axial tensile loading. In fact, after a considerable number of cycles, the signal eventually became straight. See Figure 6.14 for an example of voltage output obtained from a deep "U" notch Al prototype sensor, tested under constant amplitude loading (50% yield) with R=0.05.

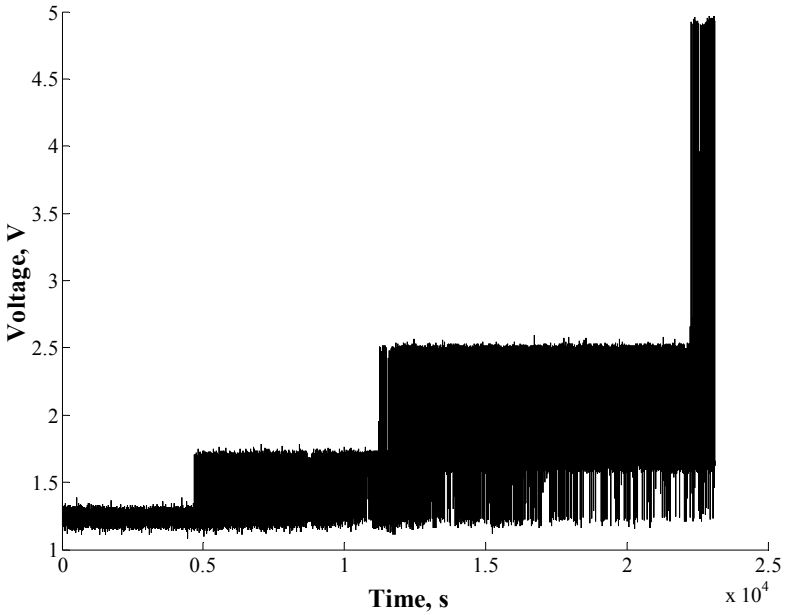

Figure 6.14 Experimental results from an Al prototype sensor, tested under constant amplitude loading (50% yield) under axial tension

CHAPTER 7. CONCLUDING REMARKS AND SUGGESTIONS FOR FUTURE WORK

7.1. Summary

This research is focused on developing a prototype in-situ fatigue sensor to detect accumulation of fatigue damage in steel highway bridges. The importance of early detection of fatigue, specifically the fatigue crack nucleation in steel structures, is emphasized. This is due to the inherent nature of fatigue damage. It allows only a limited time to apply preventive measures after the fatigue cracks are initiated.

A broad literature review is presented, which addresses the fatigue damage mechanism in metals, theories to predict fatigue damage and fatigue analysis methods. Special emphasis is given to the strain-life analysis method, mean stress correction theories and Minor's damage summation rule as key methods/theories utilized in this research.

FEA method has been successfully utilized in this research to predict fatigue lives of the prototype in-situ fatigue sensors. An introduction to the FEA for fatigue life prediction is presented together with a brief market search on FE based fatigue analysis tools. An in-house fatigue code was created using the MATLAB tool. Static stress analysis results from ANSYS WB were used as inputs to the fatigue code to successfully estimate fatigue lives of the prototype in-situ fatigue sensors.

An introduction to the experimental procedure is presented with details of the test setup, DAQ, and monitoring. Details of the proof-of-concept experiments, which were

able to validate the proposed method, are presented. This also serves as a benchmark to the development of deep "U" notch Al prototype fatigue sensors.

Experimental and simulation details of deep "U" notch Al prototype sensors, that were developed along the above line of thinking, are discussed at length. Both constant amplitude and variable amplitude experimental results are discussed and compared with estimated life predictions. A sensitivity analysis is carried out for this prototype to identify the most sensitive geometric and material parameters to establish a higher accuracy for future life predictions.

Finally, other approaches taken while developing the deep "U" notch Al prototype are discussed in terms of the sensor material, backing, attachment options and test setup. Lessons learned from these approaches and methods will help further testing and development of the current design.

7.2. Concluding Remarks

The Sensor Design

The deep "U" notch Al in-situ prototype fatigue sensors developed in this research show promising results towards achieving a final design for an in-situ fatigue sensor. However, there are certain limitations pertaining to the current design that need to be addressed in the future.

The notch design needs to be further improved to obtain a reasonable gap between failures of each notch. This will be helpful in achieving a better coverage towards the fatigue life of the attached structural element. The number of sensor arms in the current design can be increased to accommodate additional notches, which will address lower stress ranges with larger number of loading cycles. See Figure 7.1 and Figure 7.2 for the

current ranges of fatigue lives of sensor notches in relation to the fatigue life of the attached steel carrier.

Scaling down of the current prototype sensor design will also be necessary to attach them closer to structural details in bridges where high stress concentrations are possible.

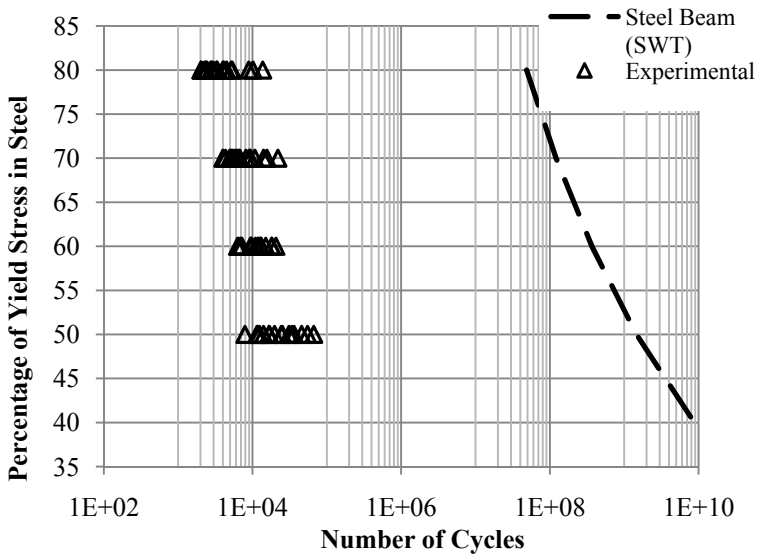

Figure 7.1 Comparison of experimental notch life and estimated carrier life for constant amplitude loading

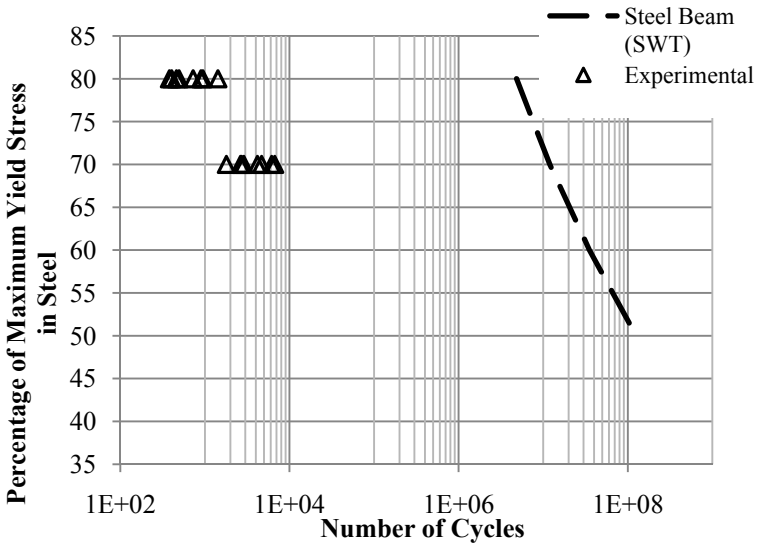

Figure 7.2 Comparison of experimental notch life and estimated carrier life for two-range variable amplitude loading

The specimen Design

The test specimen utilized in deep "U" notch prototype Al sensor experiments showed some bending effects as discussed in Chapter 5. The combined axial tension and bending stresses made it difficult to characterize the life of the notches, since the influence of bending varies with the applied stress level. It is therefore suggested to minimize the bending effect, either by introducing a thicker carrier beam than the current thickness (0.125 in.) or counter balance this effect by attaching another specimen on the opposite face.

External Circuitry/Cladding

Another limitation of the current prototype design is that it is necessary to separate sensor arms to connect them to the DAQ. Separating arms before attaching them to the carrier beam is not possible. This is because the slightest bend of the notches may destroy the sensor capability. Currently, the sensor arms are separated after the sensor is attached to the beam by carefully drilling along its arms. However, in a real structure, this may not be possible. To overcome this, a separate cladding can be attached to the sensor (see Figure 7.1). Flexible circuit material mentioned in Chapter 6 can be effectively used to create this cladding, which can be attached on top of the Al prototype. Special techniques need to be explored and developed to cut and glue, to avoid any impact towards crack propagation process across the notch ligament.

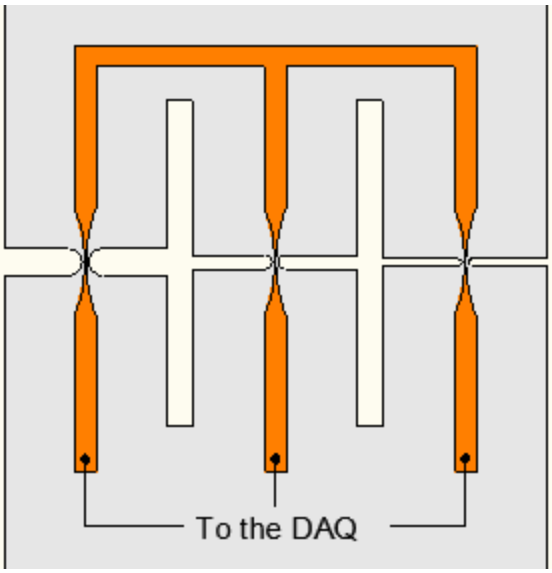

Figure 7.3 Suggested external cladding to be attached on top of the Al prototype

Attachment Options

The other important aspect that needs to be addressed is the sensor attachment. As discussed in Chapter 5, the attenuation of stress due to the adhesive can be up to 25%, which may significantly affect the fatigue life of sensor notches. Glued specimens can keep a longer setting time to control this. However, it is important to estimate the stress attenuation more precisely for accurate life predictions. A parametric study is needed in this regard.

It is also important to look into other attachment options such as capacitor discharge stud welding, a method which is being used to attach similar types of sensors to structures (Zhang 2006b). However, deploying such techniques in real bridges might be a concern under NDE regime.

Laboratory Testing

It is important to be able to predict fatigue lives of the sensor notches as accurately as possible under laboratory conditions, before attaching them to real world bridges. A good

understanding of the factors which affect the fatigue life of the notches is necessary. In addition to the geometric parameters, stress amplitude, and the mean stress effects, there are numerous other parameters, including batch-to-batch variations, and environmental parameters, which can affect the fatigue life of metals. It has been shown that environmental parameters, such as humidity and temperature, may affect the fatigue crack propagation in metals (Broek 1986). Knowing these parameters during the time of testing will help to identify such influences on the final results. It is therefore suggested that recording such data will be helpful even if their influence is found negligible, for this particular problem.

It is also important to improve the uniformity in the specimen fabrication and assembly. A high precision laser cutting is desirable. In addition, the rolling direction of the sensor material needs to be kept uniform. This is to avoid any variation of fatigue life due to the anisotropy of the rolled Al alloy as discussed in Section 5.4.3.

Simulation and Fatigue Life estimation

Simulation results of the prototype fatigue sensor can be greatly improved by establishing a higher accuracy in the strain-life parameters used in fatigue life estimations. As mentioned in Chapter 5, obtaining these parameters for the same sensor material will be an area for future focus. It will be helpful to perform an error propagation analysis to determine the error propagation or uncertainty associated with each measured parameter toward the final fatigue life. Such information can be used to update the fatigue life estimation to predict the experimental results more accurately. Better life estimation is crucial for a reliable sensor design, since it can be used to predict fatigue lives at lower stress ranges, which cannot be practically achieved through laboratory testing.

Future Testing Focus

There are several aspects that need to be the focus of future testing. Sensor response to multi-axial loading needs to be addressed since the actual loading in a bridge at fatigue prone locations, as discussed in Chapter 2, are mostly associated with combined loading. Specimens to accommodate combined loading effects to the sensor will have to be designed and tested with proper loading configurations.

Sensor response to variable amplitude loading, i.e. for an actual load history of a bridge, may be worth investigating. A typical load history in a bridge will need to be identified in this regard.

Sensor Packaging

Packaging of the final sensor design will address compact electronics and encapsulating to protect them from harsh environments. Since continuous monitoring of the sensor is not desired, deploying RFID tags will be helpful to transfer life data from the sensor to a remote location which will greatly help to monitor sensors that are installed at inaccessible locations in a bridge.

REFERENCES

3M. (2004) "3M Scotch-Weld™ Low-Odor Acrylic Adhesives, DP-810: Technical Data", <www.3M.com/industrial> (July 6, 2009).

AASHTO. (2007). AASHTO LRFD Bridge Design Specifications - 2008 Interim Revisions, American Association of State Highway and Transportation Officials, Washington, DC.

ANSYS. (2009). "Theory Reference for ANSYS and ANSYS Workbench: Release 11."

ASM International Handbook Committee. (1996). Carbon and Alloy Steels, *ASM specialty handbook*, J. R. Davis, ed., ASM International, Materials Park, OH, 260.

Bannantine, J. A., Comer, J. J., Handrock, J. L. (1990). Fundamentals of Metal Fatigue Analysis, Prentice-Hall, Inc., New Jersey.

Barron, G. E. (1975). "A Finite Element and Cumulative Damage Analysis of a Keyhole Test Specimen." Society of Automotive Engineers Inc., Warrendale, PA.

Bhachu, K. S., Baldwin, J. D., Mish K. D. (2010). "Method for Vehicle Identification and Classification for Bridge Response Monitoring." *Proceedings of the IMAC-XXVIII*, Society for Experimental Mechanics Inc., Jacksonville, FL.

Bhargava, A., Roddis, W. M. K. . (2008). "Finite Element Analysis of Fatigue Cracking of Flange-to-Gusset Plate Connection on a Two Girder Steel Bridge." *Transportation Research Board 87th Annual Meeting*, Washington DC.

Broek, D. (1986). Elementary Engineering Fracture Mechanics, Kluwer Academic Publishers, Dordrecht, Netherlands.

Browell, R., Hancq, A. (2006) "Calculating and Displaying Fatigue Results", <www.ansys.com> (June 6, 2008).

Calvert, S., Mooney, J. (2004). "Bridge Structural Health Monitoring System Using Fiber Grating Sensors: Development and Preparation for a Permanent Installation." *Proceedings of SPIE*, 61.

Casas, J. R., Cruz, P. J. S. (2003). "Fiber Optic Sensors for Bridge Monitoring." *ASCE Journal of Bridge Engineering*, 8(6), 362-373.

Chan, T. H. T., Li, Z. X., Ko, J. M. (2001). "Fatigue Analysis and Life Prediction of Bridges with Structural Health Monitoring Data - Part II: Application." *International Journal of Fatigue*, 23, 55-64.

Chase, S. B. (2005). The Role of Sensing and Measurement in Achieving FHWA's Strategic Vision for Highway Infrastructure, *Sensing Issues in Civil Structural Health Monitoring* F. Ansari, ed., Springer, Netherlands, 23-32.

Chase, S. B., Washer, G. (1998). "Nondestructive Evaluation for Bridge Management in the Next Century." *Public Roads*, 61(1), 16-25

Doebling, S. W., Farrar, C. R., Prime, M. B. (1998). "A Summary Review of Vibration Based Damage Identification Methods." *Shock and Vibration Digest*, 30(2), 91-105.

Dowling, N. E., Brose, W. R., Wilson, W. K. (1975). "Notched Member Fatigue Life Predictions by the Local Strain Approach." The Society of Automotive Engineers, Inc., PA.

DuPont. (2009a) "Kapton® HN", <http://www2.dupont.com/Kapton/en_US/products/HN/index.html> (Jan 10, 2009).

DuPont. (2009b) "Pyralux® Flexible Laminates", <http://www2.dupont.com/Pyralux/en_US/products/laminate/index.html> (Jan 10, 2009).

Endo, T., Morrow, J. (1969). "Cyclic Stress-Strain and Fatigue Behavior of Representative Aircraft Metals." *ASTM Journal of Materials*, 4(1), 159-175.

Fatemi, A., Yang, L. (1998). "Cumulative Fatigue Damage and Llife Prediction Theories: A survey of the state of the art for homogeneous materials." *International Journal of Fatigue*, 20(1), 9-34.

Fisher, J. W. (1984). Fatigue and Fracture in Steel Bridges - Case Studies, John Wiley and Sons.

Fisher, J. W., Kulak, G. L., Smith, I. F. C. (1998). Fatigue Primer for Structural Engineers, National Steel Bridge Alliance, USA.

Gongkang, F. (2004). Non Destructive Testing For Steel Highway Bridges, *NDT Methods Applied to Fatigue Reliability Assessment of Structures*, J. Mohammadi, ed., American Society of Civil Engineers, Reston, VA, 23-31.

Hancq, D. A., Walters, A. J., Beuth, J. L. (2000). "Development of an Object-Oriented Fatigue Tool." *Engineering with Computers*, 16(2), 131-144.

Landgraf, R. W., Richards, F. D., LaPointe, N. R. (1975). Fatigue Life Predictions for a Notched Member Under Complex Load Histories, *Fatigue Under Complex Loading: Analysis and Experiments*, R. M. Wetzel, ed., The Society of Automotive Engineers, Inc., Warrendale, PA, 95-106.

Lee, D. C., Lee, J. J., Kwon, I. B., Seo, D. C. (2001). "Monitoring of Fatigue Damage of Composite Structures by Using Embedded Intensity-based Optical Fiber Sensors." *Smart Materials and Structures*, 10(2), 285-292.

Lee, Y. L., Pan, J., Hathaway, R. B., Barkey, M. E. (2005). Fatigue Testing and Analysis: Theory and Practice, Elsevier Inc.

Li, Z. X., Chan, T.H.T., Ko, J.M. (2001). "Fatigue Analysis and Life Prediction of Bridges with Structural Health Monitoring Data - part I: Methodology and Strategy." *International Journal of Fatigue*, 23, 45-53.

Meyers, C. W., Srivatsan, T. S. (1986). Characterization of Mechanical Properties and Anisotropy of Cast and Wrought Aluminum Alloys, *Aluminum Alloys, Their Physical and Mechanical Properties - International Conference*, E. A. Starke Jr, Sanders Jr, T. H., ed., Engineering Materials Advisory Services Ltd., UK, 901-919.

Mohammadi, J., Guralnick, S. A., Polepeddi, R. (2004). Use of Stress Range Data in Fatigue Reliability Assessment of Highway Bridges, *NDT Methods Applied to Fatigue Reliability Assessment of Structures*, J. Mohammadi, ed., American Society of Civil Engineers, Reston, VA, 56-71.

Moore, P. O. (1998). Nondestructive Testing Handbook, C. N. Jackson Jr, Sherlock, C. N., ed., American Society for Nondestructive Testing.

Nelson, D. V., Fuchs, H. O. (1975). Predictions of Cumulative Fatigue Damage Using Condensed Load Histories, *Fatigue Under Complex Loading: Analysis and Experiments*, R. M. Wetzel, ed., The Society of Automotive Engineers, Inc., Warrendale, PA, 163-187.

Newport, A., Glinka, G. (1990). "Effect of Notch-strain Calculation Method on Fatigue-Crack-Initiation Life Predictions." *Experimental Mechanics*, 30(2), 208-216.

ODOT. (2006). Pontis Bridge Inspection Manual for Oklahoma Bridges, Oklahoma Department of Transportation - Bridge Division.

Pedersen, K. (1986). The Effect of Microstructure on Fatigue Crack Initiation in Al-Mg-Si Alloys, *Aluminum Alloys, Their Physical and Mechanical Properties - International Conference*, E. A. Starke Jr, Sanders Jr, T. H., ed., Engineering Materials Advisory Services Ltd., UK, 921-935.

Peterson, R. E. (1974). Stress Concentration Factors, John Wiley & Sons, Inc.

Pilkey, W. D. (1997). Peterson's Stress Concentration Factors, John Wiley & Sons.

Rakow, A., Chang, F. K. (2007). "An In-Situ Sensor Design for Monitoring Fatigue Damage in Bolted Joints." *6th International Workshop on Structural Health Monitoring (IWSHM)*, DEStech Publications, Inc, Stanford, CA.

SAE International. (2010). 2010 SAE Handbook, *SAEJ1397*, The Society of Automotive Engineers International, Warrendale, PA.

Schulz, W. L., Udd, E., Seim, J. M., Laylor, H. M., McGill, G. E. (1998). "Single and Multiaxis Fiber Grating Based Strain Sensors for Civil Structure Applications " *SPIE Proceedings*, 71.

Son, J., Mohammadi, J. (2004). NDT Methods Applied to Fatigue Reliability Assessment of Structures, *A Review of Non-destructive Test Methods for Bridges*, J. Mohammadi, ed., American Society of Civil Engineers, Reston, VA, 122-138.

Topper, T. H. (2009) "F.D.+E. Experimental HTML Fatigue Database", <http://fde.uwaterloo.ca/Fde/Material/Alum/AA7075/aa7075.html > (June 16, 2008).

Tucker, L., Bussa, S. (1975). The SAE Cumulative Fatigue Damage Test Program, *Fatigue Under Complex Loading: Analysis and Experiments*, R. M. Wetzel, ed., The Society of Automotive Engineers, Inc., Warrendale, PA, 3-53.

U.S Department of Defense. (2003). Department of Defense Handbook: MIL-HDBK-5J, *Metallic Materials and Elements for Aerospace Vehicle Structures*, Department of Defense.

Vishay. (2008) "Special Use Sensors - Crack Propagation Sensors", <www.vishaymg.com> (June 16, 2008).

Wijesinghe, B. H. M. P., Zacharie, S., Baldwin, J. D., Runolfsson, T. (2010). "In-Situ Fatigue Sensors for Structural Health Monitoring of Highway Bridges." *Proceedings of the IMAC-XXVIII*, Society of Experimental Mechanics Inc., Jacksonville, FL.

Wood, W. A. (1958). "Recent Observations on Fatigue Failure in Metals." *Symposium on Basic Mechanisms of Fatigue*, ASTM STP 237, Philadelphia, PA, 110-121.

Zacharie, S. A. (2009). "In Situ Fatigue Sensor Characterization," MS thesis, University of Oklahoma, Norman, OK.

Zhang, Y. (2006a). "In Situ Fatigue Crack Detection using Piezoelectric Paint Sensor." *Journal of Intelligent Material Systems and Structures*, 17(10), 843-852.

Zhang, Y. H., Tubby, P. J. (2006b). "Development of a Fatigue Sensor for Welded Steel Structures." *International Conference on Residual Fatigue Lifetime Extension of In-Service Structures*, JIP, Paris, France.

APPENDIX A - Verification of MATLAB Code for Constant Amplitude Loading

MATLAB code

```
%=========================================================================
% This m file calculates fatigue life for constant amplitude
%proportional loading when nominal stresses are known
% Neuber's Rule is used to relate nominal stresses to local stresses
% Copyright - Priyantha Wijesinghe- 7th July 2009
%=========================================================================
%% Input parameters
% Reference: Bannantine, J.A., Comer, J. J., Handrock, J. L.,
%Fundamentals of Metal Fatigue Analysis, Prentice-Hall, 1990
%Example 4.2 (page 143)
E = 30000000; %Young's Modulus (psi)
SigmaF_prime = 169000; %Strength Coefficient (psi)
EpsilonF_prime = 1.14; %Ductility Coefficient
c = -0.67; % Ductility Exponent
b = -0.081; %Strength Exponent
K_prime = 154000; %Cyclic Strength Coefficient (psi)
n_prime = 0.123; %Cyclic Strain Hardening Exponent
K = 2.42; %stress concentration factor
%% Nominal Stress history
s_max=50000; %maximum nominal stress (psi)
s_min=-50000; %minimum nominal stress (psi)
delta_s=s_max-s_min;
%
%% Local Stress Calculations using Neuber's Rule
% Initial loading curve
xinit=1;
x=sym('x');
f=(((K*s_max)^2)/E)-(x*((x/E)+(x/K_prime)^(1/n_prime))); % Neuber and
cyclic stress-strain curve equations-combined
fprime=diff(f);
newton %call newton m file for Newton-Raphson iteration
sigma_max=x1;
epsilon_max=(((K*s_max)^2)/(E*sigma_max));
% Nominal Stress Reversal
xinit=1;
x=sym('x');
f=(x^2/(2*E))+(x*((x/(2*K_prime))^(1/n_prime)))-
(((K*delta_s)^2)/(2*E)); % Neuber and hysteresis curve equations-
%combined
fprime=diff(f);
newton
delta_sigma=x1;
delta_epsilon=((K*delta_s)^2)/(E*delta_sigma);
sigma_min=sigma_max-delta_sigma;
epsilon_min=epsilon_max-delta_epsilon;
sigma_mean=(sigma_max+sigma_min)/2;
epsilon_a=(delta_epsilon)/2; %calculated local strain amplitude
%
```

```
%% Newton-Raphson Iteration to calculate life
% Life with SWT mean stress correction
xinit=1; %initial value
x=sym('x');
f=(((SigmaF_prime^2)/E)*(2*x)^(2*b))+(SigmaF_prime*EpsilonF_prime*((2*x
)^(b+c)))-(sigma_max*epsilon_a); %corrected strain-life equation
fprime=diff(f);
newton
life_SWT_cycles=x1
life_SWT_reversals=x3
%
%% Morrow's mean stress correction
xinit=1;
x=sym('x');
f=(((SigmaF_prime-sigma_mean)/E)*(2*x)^b)+(EpsilonF_prime*(2*x)^c)-
epsilon_a; %corrected strain-life equation
fprime=diff(f);
newton
life_Morrows_cycles=x1
life_Morrows_reversals=x1
%
%% Without mean stress correction
xinit=1;
x=sym('x');
f=((SigmaF_prime/E)*(2*x)^b)+(EpsilonF_prime*(2*x)^c)-epsilon_a; %
strain-life equation
fprime=diff(f);
newton
life_NoMeanCorrection_cycles=x1
life_NoMeanCorrection_reversals=2*x1

%=========================================================================
% This m file performs the Newton-Raphson iteration
%=========================================================================
n=0;
x0=xinit;
x2=xinit+1;
while abs(x2-x0)>.0000001 && n<500,
   x1=x0-subs(f,x,x0)/subs(fprime,x,x0);
   x2=x0;
   x0=x1;
   n=n+1;
end
x1;
n;
subs(f,x,x1);

Output

life_SWT_cycles = 3.3256e+003

life_Morrows_cycles = 2.8082e+003

life_NoMeanCorrection_cycles = 2.8082e+003
```

APPENDIX B - Verification of MATLAB Code for Variable Amplitude Loading

MATLAB code

```
%=========================================================================
% This m file calculates fatigue life for variable amplitude loading
%when the nominal strain history is given as the input
% Neuber's Rule is used to relate nominal stresses to local stresses
% Rain-flow counting method is used for cycle counting
% Copyright - Priyantha Wijesinghe - 9th August 2009
%=========================================================================
%% Input Parameters
% Reference: Society of Automotive Engineers., Technical Report on
Fatigue Properties - SAE J1099, Society of Automotive Engineers
Warrendale, PA, 1975
%Illustrative Example (page 3.83)
E = 29500000; %Young's Modulus (psi)
SigmaF_prime = 130000; %Strength Coefficient (psi)
b = -0.12; %Strength Exponent
EpsilonF_prime = 0.41; %Ductility Coefficient
c = -0.51; % Ductility Exponent
K_prime = 112000; %Cyclic Strength Coefficient (MPa)
n_prime = 0.18; %Cyclic Strain Hardening Exponent
K = 3; %Fatigue Stress Concentration Factor
SH=[4500 -2000 4000 -4500 3000 -4500 4500]'; %nominal strain history
(micro-strains)
%% Calculate sigma_1 corresponding to e1
SH_1=SH*10^-6';
e1=SH_1(1);
xinit=1;
x=sym('x');
f=((x/E)+(x/K_prime)^(1/n_prime))-((K^2*e1^2*E)/x); % Cyclic stress-
strain equation
fprime=diff(f);
newton
sigma_1=x1;
epsilon1=(sigma_1/E)+(sigma_1/K_prime)^(1/n_prime); % Calculate local
strain from local stress
%% Calculate other epsilon values (i.e.epsilon_2, epsilon1_3...)
(epsilon1_other)corresponding to rest of the strain ranges
% First, sort the strain ranges (delta_e)
for z=1:length(SH)-1;
delta_e1(z)=(SH_1(z)-SH_1(z+1));
end
delta_e2=delta_e1';
delta_e = [0; delta_e2]; %add the initial strain range to the array
% Then, calculate the corresponding stress ranges (delta_sigma)and
strain
% ranges (delta_epsilon)
for j=1:length(delta_e);
xinit=0.02;
x=sym('x');
```

```
f=((x/E)+2*(x/(2*K_prime))^(1/n_prime))-(((K^2)*((delta_e(j))^2)*E)/x);
% Hysteresis curve equation
fprime=diff(f);
newton
delta_sigma(j)=x1;
delta_epsilon(j)=(delta_sigma(j)/E)+2*((delta_sigma(j)/(2*K_prime)))^(1
/n_prime);
end
delta_sigma=delta_sigma';
delta_epsilon=[epsilon1 ;delta_epsilon(2:length(SH_1))'];
% sign correction for delta_epsilon
for i=1:length(SH)-1;
    if SH(i)<SH(i+1);
        delta_epsilon(i+1)=-delta_epsilon(i+1);
    else
        delta_epsilon(i+1)=delta_epsilon(i+1);
    end
end
%% Then, calculate other epsilon values
epsilon_other1(1)=epsilon1; %put back epsilon1 calculated from the
stress-strain equation
 for s=2:length(delta_epsilon);
       epsilon_other1(s)=epsilon_other1(s-1)-delta_epsilon(s);
 end
 epsilon_other=epsilon_other1';
% Then, calculate other sigma values
sigma_other1(1)=sigma_1; %put back the sigma_1 calculated from the
stress-strain equation
 for w=2:length(delta_sigma);
  if delta_e(w)>0;
    sigma_other1(w)=sigma_other1(w-1)-delta_sigma(w);
  else
    sigma_other1(w)=sigma_other1(w-1)+delta_sigma(w);
  end
 end
sigma_other=sigma_other1';
disp('Notch Strain | Strain range | Stress range | Calculated stress');
A=[epsilon_other delta_epsilon delta_sigma sigma_other];
disp ([A(:,1),A(:,2),A(:,3),A(:,4)]);
%% Cycle counting - Rainflow counting method (3 point) is used as per
SAE
%and ASTM recommendations
epsilon_other=epsilon_other*10^6;
n = 1;
cc = 0;
while length(epsilon_other) > 1
    while (abs(epsilon_other(n+1) - epsilon_other(n+2)) -
abs(epsilon_other(n) - epsilon_other(n+1)) < 0)
        n = n + 1;
    end
    cc = cc + 1;
    Total(cc,1) = epsilon_other(n);
    Total(cc,2) = epsilon_other(n+1);
    Total(cc,3) = abs(epsilon_other(n) - epsilon_other(n+1));
    Total(cc,4) = (epsilon_other(n) + epsilon_other(n+1))/2;
    epsilon_other(n) = [];
    epsilon_other(n) = [];
```

```
    n = 1;
end
disp('Identified cycles, their ranges and mean values');
disp('      From       To      Range      Mean');
disp([Total(:,1),Total(:,2),Total(:,3),Total(:,4)]);
cc; %total number of cycles
%% Fatigue life calculations
% Identify the max. and min. strain values corresponding to each cycle
obtained from Rain-flow counting
[m,g] = size(Total);
for p=1:m;
    if Total(p,1)>Total(p,2);
        epsilon_max(p)=Total(p,1);
        epsilon_min(p)=Total(p,2);
        epsilon_a(p)=(Total(p,1)-Total(p,2))/2;
    else epsilon_min(p)=Total(p,1);
        epsilon_max(p)=Total(p,2);
        epsilon_a(p)=(Total(p,2)-Total(p,1))/2;
    end
end
epsilon_max=epsilon_max'*10^-6; %convert into strain for fatigue calcs.
epsilon_min=epsilon_min'*10^-6;
epsilon_a=epsilon_a'*10^-6;
% Identify the corresponding stresses (max and min) from A
AA(:,1)=roundn(A(:,1),-4);
epsilon_max11=roundn(epsilon_max,-4);
epsilon_min11=roundn(epsilon_min,-4);
[v,u] = size(A);
for a=1:cc;
    for bbb=1:v;
if epsilon_max11(a)==AA(bbb,1);
    sigma_max1(a,:)=A(bbb,4); break, end
    end
 end
sigma_max=sigma_max1';
%
for a=1:cc;
    for bbc=1:m
if epsilon_min11(a)==AA(bbc,1);
sigma_min1(a)=A(bbc,4); break,end
    end
end
sigma_min=sigma_min1';
sigma_mean=(sigma_max+sigma_min)/2;
%% Life with SWT mean stress correction
for g=1:cc;
xinit=1;
x=sym('x');
f=(((SigmaF_prime^2)/E)*(2*x)^(2*b))+(SigmaF_prime*EpsilonF_prime*((2*x
)^(b+c)))-(sigma_max(g)*epsilon_a(g)); %corrected strain-life equation
fprime=diff(f);
newton
life_SWT(g,:)=x1;
damage_SWT(g,:)=1/x1;
end
life_Nf_SWT=life_SWT;
Total_damage_SWT=sum(damage_SWT);
```

```
Total_Life_Blocks_SWT=1/(Total_damage_SWT)
%% Life with Morrow's mean stress correction
for q=1:cc;
xinit=1;
x=sym('x');
f=(((SigmaF_prime-sigma_mean(q))/E)*(2*x)^b)+(EpsilonF_prime*(2*x)^c)-
epsilon_a(q); %corrected strain-life equation
fprime=diff(f);
newton
life_Morrows(q,:)=x1;
damage_Morrows(q,:)=1/x1;
end
life_Nf_Morrows=life_Morrows;
Total_damage_Morrows=sum(damage_Morrows);
Total_Life_Blocks_Morrows=1/(Total_damage_Morrows)
%% Life without mean stress correction
for q=1:cc;
xinit=1;
x=sym('x');
f=((SigmaF_prime/E)*(2*x)^b)+(EpsilonF_prime*(2*x)^c)-epsilon_a(q); %
strain-life equation
fprime=diff(f);
newton
life_NoMeanCorrection(q,:)=x1;
damage_NoMeanCorrection(q,:)=1/x1;
end
life_Nf_NoMeanCorrection=life_NoMeanCorrection;
Total_damage_NoMeanCorrection=sum(damage_NoMeanCorrection);
Total_Life_Blocks_NoMeanCorrection=1/(Total_damage_NoMeanCorrection)
```

Output

```
Notch Strain | Strain range | Stress range | Calculated stress
  7.6652e-002  7.6652e-002            0  7.0140e+004
 -1.1904e-002  8.8555e-002  1.2667e+005 -5.6530e+004
  6.5487e-002 -7.7391e-002  1.2350e+005  6.6973e+004
 -7.3717e-002  1.3920e-001  1.3780e+005 -7.0828e+004
  3.8990e-002 -1.1271e-001  1.3251e+005  6.1678e+004
 -7.3717e-002  1.1271e-001  1.3251e+005 -7.0828e+004
  7.9586e-002 -1.5330e-001  1.4028e+005  6.9453e+004

Identified cycles, their ranges and mean values
      From       To      Range      Mean
  1.0e+005 *
   -0.1190    0.6549    0.7739    0.2679
   -0.7372    0.3899    1.1271   -0.1736
    0.7665   -0.7372    1.5037    0.0147

Total_Life_Blocks_SWT = 11.6318

Total_Life_Blocks_Morrows = 8.2552

Total_Life_Blocks_NoMeanCorrection = 8.2852
```

APPENDIX C - *LabVIEW* Front Panel and the Block Diagram

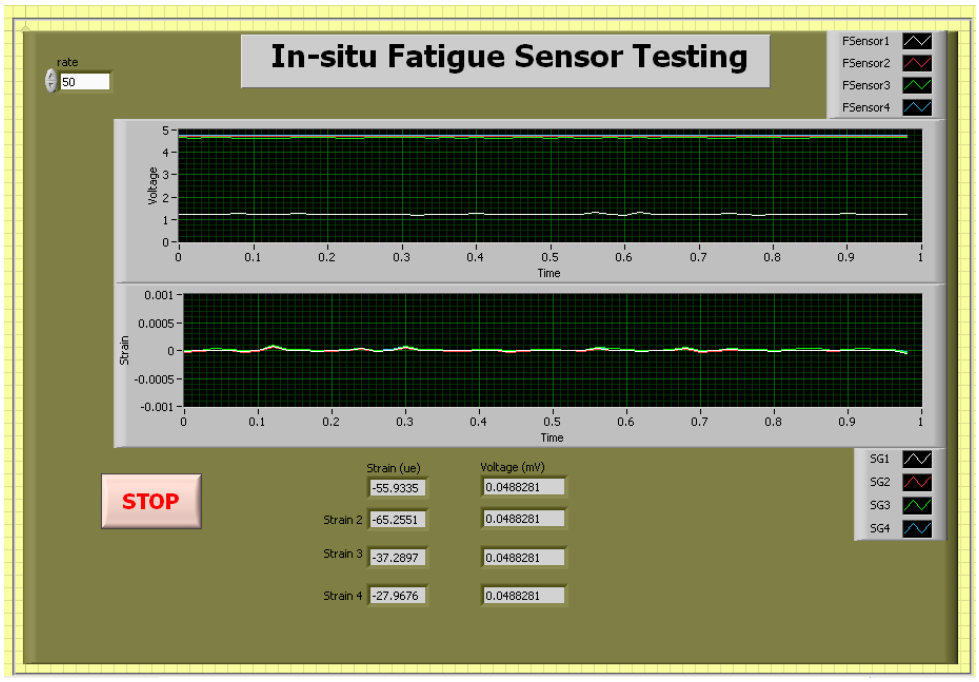

Figure 1. *LabVIEW* front panel

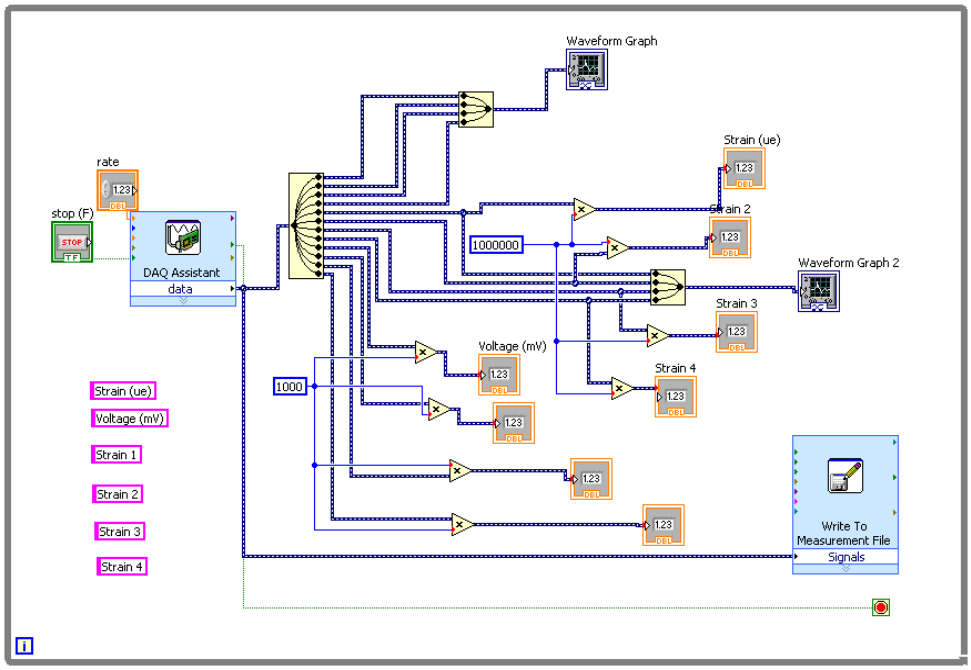

Figure 2. *LabVIEW* block diagram

APPENDIX D - FE and MATLAB Results for Constant Amplitude Loading

Table 1. Nominal Stresses Obtained from FEA Results for 2a and 1b Al Prototype Sensors

Geometry 2a	0.125 in. Diameter Notch		0.0625 in. Diameter Notch		0.03125 in. Diameter Notch	
	Max.	Min.	Max.	Min.	Max.	Min.
80%Sy: 9600lbf(max), 480lbf(min)	3905.50	147.30	4093.20	154.28	4322.10	162.51
70%Sy: 8400lbf(max), 420lbf(min)	3379.10	127.43	3541.30	133.46	3739.40	140.55
60%Sy: 7200lbf(max), 360lbf(min)	2857.00	107.81	2994.00	112.91	3161.50	118.89
50%Sy: 6000lbf(max), 300lbf(min)	2340.70	88.51	2452.80	92.69	2590.00	97.57
40%Sy: 4800lbf(max), 240lbf(min)	1832.40	69.56	1920.20	72.84	2027.50	76.65
Geometry 1b	**0.04 in. Ligament**		**0.035 in. Ligament**		**0.03 in. Ligament**	
	Max.	**Min.**	**Max.**	**Min.**	**Max.**	**Min.**
80%Sy: 9600lbf(max), 480lbf(min)	4534.2	166.56	4348.00	159.89	4274.60	157.03
70%Sy: 8400lbf(max), 420lbf(min)	3927.5	145.91	3765.70	140.07	3702.10	137.56
60%Sy: 7200lbf(max), 360lbf(min)	3318.10	123.37	3181.20	118.44	3127.50	116.31
50%Sy: 6000lbf(max), 300lbf(min)	2716.00	101.19	2603.90	97.158	2559.90	95.41
40%Sy: 4800lbf(max), 240lbf(min)	2124.00	79.451	2036.30	76.295	2001.80	74.916

Table 2. Calculated SCF's Based on Nominal and Local (Notch Root) Stresses for 2a and 1b Al Prototype Sensors

GEOMETRY 2a	0.125 in. Diameter Notch		0.0625 in. Diameter Notch		0.03125 in. Diameter Notch	
	Notch Root Stress	SCF	Notch Root Stress	SCF	Notch Root Stress	SCF
80%Sy: 9600lbf(max)	107,220	27.454	131,040	32.014	165,885	38.381
70%Sy: 8400lbf(max)	92,913	27.496	113,560	32.067	143,780	38.450
60%Sy: 7200lbf(max)	78,711	27.550	96,214	32.136	121,830	38.536
50%Sy: 6000lbf(max)	64,651	27.620	79,038	32.224	100,080	38.641
40%Sy: 4800lbf(max)	50,778	27.711	62,089	32.335	78,600	38.767
Average SCF		**27.570**		**32.160**		**38.550**
GEOMETRY 1b	**0.04 in. Ligament**		**0.035 in. Ligament**		**0.03 in. Ligament**	
	Notch Root Stress	SCF	Notch Root Stress	SCF	Notch Root Stress	SCF
80%Sy: 9600lbf(max)	142,950	31.527	155,110	35.674	164,210	38.415
70%Sy: 8400lbf(max)	124,060	31.588	134,610	35.746	142,490	38.489
60%Sy: 7200lbf(max)	105,070	31.666	114,010	35.839	120,670	38.584
50%Sy: 6000lbf(max)	86,265	31.762	93,612	35.951	99,075	38.703
40%Sy: 4800lbf(max)	67,717	31.882	73,492	36.091	77,773	38.852
Average SCF		**31.680**		**35.860**		**38.610**

Table 3. Experimental and Estimated Fatigue Results for 2a Al Prototype Sensor

GEOMEREY 2a	0.125 in. Diameter Notch					
	Morrow	**SWT**	**SWT with 25% Stress Reduction**	**Test1**	**Test2**	**Test3**
80% Sy	4,908	5,019	58,750	13,714	10,158	8,943
70% Sy	14,726	15,585	266,720	15,617	14,066	22,023
60% Sy	87,610	72,755	1,943,100	20,689	18,150	18,242
50% Sy	1,502,100	637,310	24,792,000	45,900	66,840	55,140
40% Sy	80,125,000	13,537,000	610,010,000	No Experimental Data		
	0.0625 in. Diameter Notch					
	Morrow	**SWT**	**SWT with 25% Stress Reduction**	**Test1**	**Test2**	**Test3**
80% Sy	1,540	1,333	9,786	3,281	4,489	3,995
70% Sy	3,422	3,340	33,867	5,965	10,768	9,370
60% Sy	10,905	11,631	181,030	12,879	11,893	12,702
50% Sy	83,178	69,796	1,844,800	36,360	33,720	25,239
40% Sy	2,878,200	1,039,800	42,289,000	No Experimental Data		
	0.03125 in. Diameter Notch					
	Morrow	**SWT**	**SWT with 25% Stress Reduction**	**Test1**	**Test2**	**Test3**
80% Sy	457	367	1,833	2,024	2,961	2,353
70% Sy	946	779	4,811	4,969	6,557	6,771
60% Sy	2,283	2,094	17,980	6,514	9,704	6,983
50% Sy	7,984	8,469	118,610	11,484	14,055	16,695
40% Sy	89,220	73,824	1,978,600	No Experimental Data		

Table 4. Experimental and Estimated Fatigue Results for 1b Al Prototype Sensor

GEOMEREY 1b	0.04 in. Ligament					
	Morrow	**SWT**	**SWT with 25% Stress Reduction**	**Test1**	**Test2**	**Test3**
80% Sy	971	801	4,994	5,174	4,124	5,344
70% Sy	2,063	1,861	15,340	9,101	5,458	8,169
60% Sy	5,610	5,812	71,631	15,064	12,037	13,117
50% Sy	30,225	30,000	629,150		31,020	24,396
40% Sy	725,520	368,860	13,449,000	No Experimental Data		
	0.035 in. Ligament					
	Morrow	**SWT**	**SWT with 25% Stress Reduction**	**Test1**	**Test2**	**Test3**
80% Sy	638	515	2,821	2,824	2,746	3,350
70% Sy	1,334	1,134	7,886	6,263	5,261	5,926
60% Sy	3,335	3,242	32,542	9,345	9,633	11,018
50% Sy	13,745	14,584	244,470	11,696	19,830	12,456
40% Sy	217,940	148,270	4,644,500	No Experimental Data		
	0.03 in. Ligament					
	Morrow	**SWT**	**SWT with 25% Stress Reduction**	**Test1**	**Test2**	**Test3**
80% Sy	479	384	1,945	2,439	2,053	2,269
70% Sy	990	818	5,125	4,342	4,001	5,015
60% Sy	2,404	2,222	19,493	7,204	6,305	9,766
50% Sy	8,607	9,151	131,610	7,922	16,932	11,724
40% Sy	101,780	81,960	2,254,500	No Experimental Data		

APPENDIX E - Experimental and Estimated Results for Two-Range Variable Amplitude Loading

Table 1. Experimental and Estimated Results for Two-Range Variable Amplitude Loading – 1b Al Prototype Sensor

0.04 in. Ligament													
Loading	**Max. % Sy in Steel**	**SWT**	**SWT with 25% Stress Reduction**	**No Mean**	**No Mean with 25% Stress Reduction**	**Test1**	**Test2**	**Test3**	**Test4**	**Test5**	**Test6**	**Test7**	**Test8**
80%+40% Sy	80	80	499	299	8,522	1,425	898	947	621	2,081*		358‡	898‡
70%+40% Sy	70	185	1,532	1,401	54,434	6,690	6,166	4,679	1,126	1,299*	3,154*		
60%+40% Sy	60	572	7,125	11,086	490,756								
50%+40% Sy	50	2,774	60,103	142,589	6,530,527					No Experimental Data			
0.035 in. Ligament													
Loading	**Max. % Sy in Steel**	**SWT**	**SWT with 25% Stress Reduction**	**No Mean**	**No Mean with 25% Stress Reduction**	**Test1**	**Test2**	**Test3**	**Test4**	**Test5**	**Test6**	**Test7**	**Test8**
80%+40% Sy	80	51	282	142	3,039	724	495	461	327	1,199*		246‡	493‡
70%+40% Sy	70	113	787	557	18,674	2,708	4,173	2,887	863	1,005*	2,598*		
60%+40% Sy	60	317	3,232	3,918	166,129								
50%+40% Sy	50	1,328	23,225	48,426	2,202,017					No Experimental Data			
0.03 in. Ligament													
Loading	**Max. % Sy in Steel**	**SWT**	**SWT with 25% Stress Reduction**	**No Mean**	**No Mean with 25% Stress Reduction**	**Test1**	**Test2**	**Test3**	**Test4**	**Test5**	**Test6**	**Test7**	**Test8**
80%+40% Sy	80	38	194	90	1,520	380	405	379	369	582*		105‡	405‡
70%+40% Sy	70	81	511	310	8,930	1,790	2,626	2,240	565	654*	2,024*		
60%+40% Sy	60	216	1,933	1,945	78,309								
50%+40% Sy	50	823	12,435	22,972	1,034,915					No Experimental Data			

* Sensor arms cut separated

‡ Sensor arms cut separated through spacers

Table 2. A Sample Set of Calculations Using Miner's Rule for 1b Al Prototype Sensor for Two-Range Variable Amplitude Loading

Load History 1 (80% + 40%)					Load History 1 with 25% Stress Reduction				
0.04 in. Ligament					**0.04 in. Ligament**				
Nominal Stress Range	**4,368**	SWT	No Mean	Morrow	Nominal Stress Range	**3,276**	SWT	No Mean	Morrow
80%	n1	10	10	10	80%	n1	10	10	10
80%	N1	801	2,992	971	80%	N1	4,994	85,228	4,889
Nominal Stress Range	**2,045**				Nominal Stress Range	**1,533**			
40%	n2	10	10	10	40%	n2	10	10	10
40%	N2	368,860	37,088,000	725,520	40%	N2	13,449,000	1,708,300,000	79,392,000
Damage Increment per Block		0.0125043	0.0033424	0.0103074	Damage Increment per Block		0.0020032	0.0001173	0.0020455
Blocks to failure		**80**	**299**	**97**	**Blocks to Failure**		**499**	**8,522**	**489**
0.035 in. Ligament					**0.035 in. Ligament**				
Nominal Stress Range	**4,188**	SWT	No Mean	Morrow	Nominal Stress Range	**3,141**	SWT	No Mean	Morrow
80%	n1	10	10	10	80%	n1	10	10	10
80%	N1	515	1,423	638	80%	N1	2,821	30,391	2,956
Nominal Stress Range	**1,960**				Nominal Stress Range	**1,470**			
40%	n2	10	10	10	40%	n2	10	10	10
40%	N2	148,270	12,494,000	217,940	40%	N2	4,644,500	575,020,000	20,418,000
Damage increment per block		0.0194948	0.0070277	0.0157257	Damage Increment per Block		0.0035471	0.0003291	0.0033838
Blocks to Failure		**51**	**142**	**64**	**Blocks to Failure**		**282**	**3,039**	**296**
0.03 in. Ligament					**0.03 in. Ligament**				
Nominal Stress Range	**4,118**	SWT	No Mean	Morrow	Nominal Stress Range	**3,088**	SWT	No Mean	Morrow
80%	n1	10	10	10	80%	n1	10	10	10
80%	N1	384	902	479	80%	N1	1,945	15,202	2,143
Nominal Stress Range	**1,927**				Nominal Stress Range	**1,445**			
40%	n2	10	10	10	40%	n2	10	10	10
40%	N2	81,960	5,881,100	101,780	40%	N2	2,254,500	270,410,000	7,977,000
Damage Increment per Block		0.0261512	0.0110858	0.0209946	Damage Increment per Block		0.0051450	0.0006578	0.0046674
Blocks to Failure		**38**	**90**	**48**	**Blocks to Failure**		**194**	**1,520**	**214**

APPENDIX F - Experimental and Estimated Results for Multiple-Range Variable Amplitude Loading

Table 1. Experimental and Estimated Results for Multiple-Range Variable Amplitude Loading, 1b Al Prototype Sensor

Loading	0.04 in. Ligament								
	Max. % Sy in Steel	**SWT**	**SWT with 25% Stress Reduction**	**No Mean**	**No Mean with 25% Stress Reduction**	**Test1**	**Test2**	**Test3**	**Test4**
80%+60%+50% Sy	80	242	2,018	1,359	40,260	2,735	1,373	3,302	3,375
70%+60%+50% Sy	70	368	4,354	4,980	202,675	2,568	2,822	5,726	1,723
Loading	**0.035 in. Ligament**								
	Max. % Sy in Steel	**SWT**	**SWT with 25% Stress Reduction**	**No Mean**	**No Mean with 25% Stress Reduction**	**Test1**	**Test2**	**Test3**	**Test4**
80%+60%+50% Sy	80	141	1,063	628	14,270	2,100	1,102	2,360	2,492
70%+60%+50% Sy	70	201	2,040	1,900	69,186	2,108	1,851	3,506	1,644
Loading	**0.03 in. Ligament**								
	Max. % Sy in Steel	**SWT**	**SWT with 25% Stress Reduction**	**No Mean**	**No Mean with 25% Stress Reduction**	**Test1**	**Test2**	**Test3**	**Test4**
80%+60%+50% Sy	80	98	694	387	7,096	1,220	634	1,419	1,887
70%+60%+50% Sy	70	135	1,237	1,012	32,910	1,436	1,307	2,299	1,112

Table 2. A Sample Set of Calculations using Miner's Rule for 1b Al Prototype Sensor for Multiple-Range Variable Amplitude Loading

Load History 1 (80% +60%+50%)					Load History 1 with 25% Stress Reduction				
0.04 in. Ligament					**0.04 in. Ligament**				
Nominal Stress Range	**4,368**	SWT	No Mean	Morrow	Nominal Stress Range	**3,276**	SWT	No Mean	Morrow
80%	n1	2	2	2	80%	n1	2	2	2
80%	N1	805	2,943	967	80%	N1	5,080	84,804	4,979
Nominal Stress Range	**3,195**				Nominal Stress Range	**2,396**			
60%	n2	4	4	4	60%	n2	4	4	4
60%	N2	5,916	110,710	5,722	60%	N2	73,024	4,919,700	88,378
Nominal Stress Range	**2,615**				Nominal Stress Range	**1,961**			
50%	n3	30	30	30	50%	n3	30	30	30
50%	N3	30,624	1,481,500	31,106	50%	N3	636,130	67,897,000	1,498,000
Damage Increment per Block		0.004140	0.000736	0.003731	Damage Increment per Block		0.000496	0.000025	0.000467
Blocks to Failure		**242**	**1,359**	**268**	**Blocks to Failure**		**2,018**	**40,260**	**2,142**
0.035 in. Ligament					**0.035 in. Ligament**				
Nominal Stress Range	**4,188**				Nominal Stress Range	**3,141**			
80%	n1	2	2	2	80%	n1	2	2	2
80%	N1	516	1,399	633	80%	N1	2,861	30,136	2,991
Nominal Stress Range	**3,063**				Nominal Stress Range	**2,297**			
60%	n2	4	4	4	60%	n2	4	4	4
60%	N2	3,290	39,008	3,381	60%	N2	33,217	1,664,700	34,162
Nominal Stress Range	2507				Nominal Stress Range	**1,880**			
50%	n3	30	30	30	50%	n3	30	30	30
50%	N3	14,883	502,890	14,113	50%	N3	248,190	22,894,000	429,360
Damage Increment per Block		0.007110	0.001591	0.006470	Damage Increment per Block		0.000940	0.000070	0.000856
Blocks to Failure		**141**	**628**	**155**	**Blocks to Failure**		**1,063**	**14,270**	**1,169**